

**Neotectonics of the East African Rift System:
new interpretations from conjunctive analysis of
field and remotely sensed datasets in the Lake
Magadi area, Kenya**

Ghebretinsae Woldu Sequar
February 2009

Neotectonics of the East African Rift System: new interpretations from conjunctive analysis of field and remotely sensed datasets in the Lake Magadi area, Kenya

by

Ghebretinsae Woldu Sequar

Thesis submitted to the International Institute for Geo-information Science and Earth Observation in partial fulfilment of the requirements for the degree of Master of Science in Geo-information Science and Earth Observation, Specialisation: Earth Resource Exploration

Thesis Assessment Board

Prof. Dr. F.D. van der Meer (Chairman)
Dr. J. van der Kruk (External Examiner)
Dr. T. Woldai (1st supervisor)
Dr. E.J.M. Carranza (2nd supervisor)

Observer:

Drs. T.M. Loran (Program director)



**INTERNATIONAL INSTITUTE FOR GEO-INFORMATION SCIENCE AND EARTH OBSERVATION
ENSCHEDÉ, THE NETHERLANDS**

Disclaimer

This document describes work undertaken as part of a programme of study at the International Institute for Geo-information Science and Earth Observation. All views and opinions expressed therein remain the sole responsibility of the author, and do not necessarily represent those of the institute.

Abstract

Proper characterization of tectonic extension of a rift helps to understand its seismicity, geothermal activity, volcanicity and general geodynamics. For the Kenya Rift, two different models of extension directions (E-W to ESE-WNW and NW-SE) have been proposed. However, there is a knowledge gap in the understanding of neotectonics of the southern Kenya Rift (Lake Magadi area) since previous works in the area were based on limited field sites and they lacked subsurface investigations. Hence, conjunctive analysis of field and remotely sensed datasets of the Lake Magadi area is essential. Field data from several locations in a larger area are required in order to obtain representative information about the conditions of extensional stress in the Lake Magadi area. Remotely sensed datasets, which include space-borne multispectral imagery and geophysical (resistivity plus magnetic) data sets are likely to provide useful surface and subsurface geological information, respectively and would enable characterization of the neotectonic extension in the Lake Magadi area.

In this research, ASTER datasets, SRTM DEM, airborne magnetic data, ground magnetic data, resistivity data, structural field data, existing geological maps and location of earthquake epicenters were used. In order to extract optimum structural and lithologic information, the remotely sensed datasets were enhanced using different enhancement methods. Lithologic information extracted from the ASTER images, from field and from the airborne magnetic data was integrated in order to update geological map of the study area. Structural information was extracted from the enhanced ASTER datasets, SRTM DEM and airborne magnetic data. Combined results of these datasets revealed four fault sets in the area; normal N-S fault, dextral NW-SE fault, strike slip ENE-WSW fault and sinistral NE-SW fault. All fault sets have been observed in the field where their relative age relationship showed that the N-S faults are the oldest and the reactivated NE-SW faults are youngest. The existence of four set of faults having different styles and different relative ages suggests that there has been a geodynamic change in tectonics of the rift. These faults were created under an E-W extension direction which is explained by Anderson's fault model. Preliminary paleostress reconstruction of the field data also showed that the neotectonic extension direction of the study area is E-W. The new finding of sinistral NE-SW trending fault in the study area was created under E-W extension direction, which counterbalanced the dextral NW-SE. This finding solves the puzzle that some researchers were associating the dextral NW-SE movement with a NW-SE extension direction. Besides, the clustering of the earthquake swarms in the northern part of the Lake Magadi area is associated with the intersection of the N-S, NW-SE and NE-SW to ENE-WSW trending structures.

In the earthquake clustering area, a surface rupture has been observed by Seht et al.(2001). Ground magnetic and resistivity data characterized the subsurface nature of the rupture and revealed other hidden rupture in the site. The 2D resistivity imaging of the ruptures showed that both ruptures persist to a depth of greater than 66m signifying that the ruptures were intense. Besides, field observation showed that the surface rupture aligns along N-S to NNE-SSW signifying that the neotectonic extension direction is E-W.

The conjunctive analysis of field and remotely sensed datasets were useful in updating geological map of the study area, characterizing surface and subsurface structures and in deducing neotectonic extension of the Lake Magadi area and in explaining the clustering of earthquake in the area.

Acknowledgements

I would like to thank the Netherlands government for granting me the prestigious scholarship through the Netherlands Fellowship Program (NFP) that enabled me to achieve my dream of learning.

I am grateful to Dr T. Woldai, 1st supervisor, for his guidance, critical and constructive comments. I am equally thankful to Dr. E.J.M. Carranza, 2nd supervisor, for his commitment, critical and constructive comments.

I would like to thank Dr Sally Barritt for providing the aeromagnetic data of the study area and for establishing contact with the geophysical company, GETECH, for further metadata; I also thank Dr Sally for her comments after checking my processing progress. Mr. Tom Kerrane, from the GETECH Company, is thanked for providing detail Meta data and his prompt replies during our e-mail communications.

I am indebted to all my instructors for their diligent teaching and for sharing their enormous knowledge during my MSc study.

Much gratitude to Mr. Zack Kuria for his hospitality and guidance during the field stay in the Lake Magadi area, Kenya. Mr. Gayantha Roshana is also thanked for his cooperation and willingness to share what had during the field time.

Heartfelt thanks to my family and my friends for their encouragement and moral support. Above all I am thankful to the almighty God for his blessing and grace.

Table of contents

1. Introduction	1
1.1. Research background	1
1.2. Research problem	3
1.3. Objectives	4
1.3.1. General objective.....	4
1.3.2. Specific objectives.....	4
1.4. Research questions.....	4
1.5. Hypothesis	5
1.6. Datasets and Methodology.....	5
1.6.1. Data sets & Softwares	5
1.6.2. Methodology.....	5
1.7. Outline of the thesis	7
2. Literature Review	9
2.1. Location of study area	9
2.2. Volcanic and tectonic evolution of the EARS.....	11
2.3. Tectonic setting and geology of the Kenya Rift	13
2.3.1. Tectonic setting of the Kenya Rift	13
2.3.2. Geology of the Kenya rift.....	14
2.3.3. Remote sensing and geophysical works on the Kenya rift.....	19
3. Processing and analysis of the remote sensing datasets.....	21
3.1. Pre-processing of the remote sensing datasets.....	21
3.2. Enhancement methods	22
3.2.1. Enhancement of ASTER images	22
3.2.2. Enhancement of SRTM DEM and ASTER DEM.....	28
3.3. Analysis on faults extracted from the remote sensing datasets	30
3.3.1. Map and orientation of the faults	30
3.3.2. Fractal analysis	34
3.4. Discussion.....	38
4. Field data collection and analysis	41
4.1. Rocks	43
4.2. Faults and other structures	44
4.2.1. The different sets of structures	44
4.2.2. Tectonic significance the different fault sets	54
4.2.3. Paleostress analysis	55
4.3. Discussion.....	57
5. Processing and analysis of geophysical datasets.....	59
5.1. Magnetic data.....	59
5.1.1. Aeromagnetic	59
5.1.2. Ground survey magnetic data	65
5.2. 2D Resistivity imaging	71
5.2.1. Data collection.....	71

5.2.2.	Data analysis.....	74
5.3.	Discussion.....	76
6.	Dataset integration, discussion and rift development model	77
6.1.	Dataset integration and discussion	77
6.1.1.	Field and remotely sensed datasets	77
6.1.2.	Ground survey geophysical datasets and field data of the rupture area	80
6.1.3.	Airborne magnetic data and ASTER image	81
6.2.	Discussion of rift development model.....	83
7.	Conclusions and recommendations.....	85
7.1.	Conclusions.....	85
7.1.1.	Characterizing the surface and subsurface structures	85
7.1.2.	Lithologic investigation of the study area	87
7.2.	Recommendations.....	87
	References.....	89
	Appendix	97

List of figures

Figure 1 The East African Rift System and associated extensional stresses. Fault traces shown are driven from Chorowicz (2005) and direction of extensional stresses shown are derived from Bosworth and Strecker (1997).....	3
Figure 2 Flow chart of methodology and the procedures followed	6
Figure 3 A) Location of the Kenya Rift in the East African Rift System (EARS). Fault traces are derived from Chorowicz (2005). B) Location of the Lake Magadi area in the Kenya Rift.....	10
Figure 4 Location of the Afar and Kenya domes (Furman, 2007; Macdonald et al., 2001; Rogers et al., 2000) in the East African Rift system (EARS).....	13
Figure 5 Epicenter locations of the earthquake swarms (Seht et al., 2001).....	14
Figure 6 Regional geologic map of the Lake Magadi area after Baker and Mitchell (1976). The abbreviations used in the legend are explained below.....	16
Figure 7 Detail geologic map of the Lake Magadi area after Baker and Mitchell (1976) and Baker (1958).....	18
Figure 8 RGB colour composite of ASTER bands 6-2-1 (A) and 2-3-12 (B). Both images were pan-sharpened with hill-shade of ASTER DEM. The identified units are labeled on the image where CC represents Chert and clay.	23
Figure 9 RGB color composite of (A) 2/1-NDVI-4/6 pan sharpened with hill-shade, CC represents Chert and clay; (B) band ratio of $(11*11)/(10/12)$	24
Figure 10 PC134 of ASTER image pan sharpened with hill shade of ASTER DEM, the identified units are labeled on the image, and CC represents Chert and clay.....	26
Figure 11 Sobel filtered image of PC1, the inset indicated with box in (A) is zoomed in (B) and the interpreted faults overlying the zoomed image are shown in (C).	28
Figure 12 A) 3D SRTM DEM hill-shaded from three illumination angles 3150 (NW), 00 (N) and 2700 (W); B) interpreted faults, horst and graben overlain on the hill-shaded SRTM DEM image.....	29
Figure 13 A) Slope map derived from ASTER DEM; B) interpreted faults (gray colour) overlain on the slope map.....	30
Figure 14 Faults (interpreted from all the datasets used) with their throw direction overlying the 3D illuminated ASTER DEM hill-shade.	31
Figure 15 Rose diagram of the faults extracted from ASTER images, DEM and SRTM DEM.	32
Figure 16 A) and B) Z shaped feature showing dextral movement along the NW-SE shear zone.....	33
Figure 17 A) and B) S shaped feature showing sinistral sense of movement along the NE-SW shear zone.	33
Figure 18 Length versus class frequency of faults of the combined result (from the ASTER images, ASTER DEM and SRTM DEM).	35
Figure 19 Logarithmic plot of fault length versus frequency and the fitted line	35
Figure 20 Locations of the six topographic profiles on the ASTER DEM underlain by hill-shade of ASTERDEM.	36
Figure 21 Topographic section (distance versus elevation) along profiles 2 derived from the ASTER DEM. The section runs from west on the left to east on the right, G represents graben.	37
Figure 22 Fault throw (from six profiles along ASTER DEM) versus frequency.....	38
Figure 23 Logarithmic plot of fault throw (from six profiles along ASTER DEM) versus frequency and the fitted line.....	38

Figure 24 locations of photos taken in the field, P stands for photo.....	42
Figure 25 Rose diagram showing strike of different fault sets collected from the field, number of data is 41. The numbers are labeled as reference for estimating the strikes.....	44
Figure 26 Anderson's fault model a) Normal fault where σ_1 acts vertically on top of the earth's surface and σ_3 acts along E-W, b) σ_1 acts along N-S while σ_3 remained E-W.	55
Figure 27 Lower hemisphere Schmidt stereo-plot showing paleostress analysis result of fault planes and slickensides using Right Dihedron Method; σ_1 , σ_2 and σ_3 are maximum, intermediate and minimum principal stresses, respectively.	56
Figure 28 lower hemisphere Schmidt stereo-plot showing paleostress analysis result of fault planes and slickensides using Rotation Optimization Method; σ_1 , σ_2 and σ_3 are maximum, intermediate and minimum principal stresses, respectively.	56
Figure 29 A) Color shaded TMI of the Lake Magadi area, and (B) Color shaded analytical signal map of the Lake Magadi area, labeled units are from existing geological map. In both maps, the lake and the study area are represented in white colour and with rectangular box, respectively.....	62
Figure 30 A) Existing geological map of the study area green and B) Analytical signal of map of the study area. Both maps are overlain with outlines (green colour in A and black colour B) indicating geologic (basalt) interpretation from the analytical signal.	62
Figure 31 TMI pan-sharpened with hill-shade of ASTER DEM the Lake Magadi is represented in gray colour. 3D Euler was applied with SI equal to 1 and 0.5 and window size of 10.	65
Figure 32 locations of magnetic survey sites, zoom in of the ground survey magnetic sites is shown in Figure 33.	66
Figure 33 Zoom in from Figure 32 to show the magnetic survey sites; A) rupture site, B) south of rupture.	68
Figure 34 colour shaded maps of a) TMI and b) analytical signal of TMI; the rupture and the faults observed in the field are respectively indicated with solid lines with dotted lines in both maps.	69
Figure 35 Euler depth solution overlying the analytical signal of TMI; SI is 2 and window size is 5. The rupture is indicated with solid lines and the faults with dotted lines.....	69
Figure 36 colour shaded maps of a) TMI and b) analytical signal of TMI overlain with Euler solution SI is 0.5 and window size is 5.	70
Figure 37 Location of the resistivity survey site (rupture area), zoom in of the site is shown in Figure 38.....	72
Figure 38 resistivity profiles (P1 and P2) taken in the rupture site and the surface rupture is indicated with white lines.	73
Figure 39 inverted resistivity section along profile one on the rupture site. Iteration = 5, RMS = 5.03%, Electrode spacing = 5m.....	75
Figure 40 inverted resistivity section along profile two on the rupture site. Iteration = 5, RMS = 5.19%, Electrode spacing = 5m.....	75
Figure 41 the Euler solution data and the epicenter of the earthquake swarms overlying on the hill-shade of ASTER DEM.....	78
Figure 42 (A) and (B) showing NW-SE structure revealed by the presence of Z shape feature in the ASTER DEM and by the clustering of 3D Euler depth solution along the NW-SE trend. The dextral sense of movement is indicated by the arrows.....	79
Figure 43 show NE-SW structure revealed by the presence of S shape feature in the ASTER DEM in and by the clustering of 3D Euler depth solution along the NE-SW trend; the sinistral sense of	

movement is indicated by the arrows. Field observation photos 11 and 19 showing NE-SE faults (see section 4.2.1 under NE-SW set).....	79
Figure 44 ENE-WSW faults from A) the alignment of 3D Euler depth solution, B) the combined results of ASTER image, ASTER DEM and SRTM DEM. P7 stands for field photo 7 shown in section 4.2.1 under ENE-WSW set.	80
Figure 45 resistivity profiles (P1 and P2), the surface rupture and normal faults observed in the field (white lines) overlaying the analytical ground magnetic map of the rupture site. For resistivity cross-sections of P1 and P2 refer section 5.2.2.	81
Figure 46 A) existing geological map of the study area B) updated geological map of the study area.	83
Figure 47 A) Conceptual tectonic development model for the central and southern part of the Kenya Rift, after Le Turdu et al. (1999) showing the normal N-S, the dextral NW-SE (N130-160 ⁰) and the sinistral NE-SW (N20-30 ⁰) structures created under E-W extension; B) Rose diagram showing orientation of the structures and the corresponding stress fields.	83
Figure 48 Conceptual tectonic development model of the Kenya Rift, modified after Le Turdu et al. (1999) in order to incorporate the NE-SW (N30-60 ⁰) structures for the Lake Magadi area. B) Rose diagram showing orientation of the structures and the corresponding stress fields.	84
Figure 49 Topographic section (distance versus elevation) along profiles 4-6 derived from the ASTER DEM. The section runs from west on the left to east on the right, G represents graben.	98
Figure 50 Topographic section (distance versus elevation) along profiles 1-3 derived from the ASTER DEM. The section runs from west on the left to east on the right, G represents graben.	98
Figure 51 measured resistivity and calculated apparent resistivity pseudo sections along profile one of the rupture area.....	99
Figure 52 Measured resistivity and calculated apparent resistivity pseudo sections of profile two of the rupture area.....	99

List of photos

Photo 1 Laminated clay overlain by chert.....	43
Photo 2 taken looking SW; green and white silt clay deposit in a small graben.	43
Photo 3 N10 ⁰ E fault, photo taken looking SW.....	45
Photo 4 N10 ⁰ E fault escarpment, photo taken looking NE.....	45
Photo 5 Photo taken looking ESE showing N10 ⁰ E fault escarpment and west of the fault is a graben filled with sediments.	46
Photo 6 N140 ⁰ E trending breccia of quartz vein cutting the N-S fault, photo taken looking SE	47
Photo 7 taken plan view where head of the hammer points south; an EW quartz vein cutting the N-S vein.....	48
Photo 8 a mafic dyke oriented N90 ⁰ /45 N cross cutting the clay on the right and weathered trachyte on the left, photo taken looking east.	48
Photo 9 taken looking NNE, fault plane N104 ⁰ E/72 ⁰ SSW with horizontal slickensides.	49
Photo 10 taken looking N28 ⁰ E, the fault plane oriented N104 ⁰ E/72 ⁰ SSW is cut by the N28 ⁰ E fault.	49
Photo 11 taken looking SE, breaks in the hill due to the NE-SW fault sets cutting the N-S fault set.	50
Photo 12 a N40 ⁰ E/78 SE fault cutting the N10 ⁰ E fault, it was taken looking NW. The gray box represents a place where slicken sides was observed as shown in Photo 13.	51
Photo 13 taken looking NW, showing slicken sides [040 ⁰ /48] on the N40 ⁰ E/78 ⁰ SE fault plane.	51
Photo 14 taken looking SW showing N10 ⁰ E fault, the white box represents a place where the cross cutting relation of the two set of faults was observed (see Photo 15).....	52
Photo 15 taken looking NW, plane N44 ⁰ E/86 SE with slickensides (zoomed in Photo 16) cuts the N10 ⁰ E fault. The sinistral sense of movement is indicated with black half arrow.	52
Photo 16 taken looking NW, closer view of the slicken sides 044 ⁰ /45 in photo 15	53
Photo 17 taken looking SW, it shows the sinistral movement along the N60 ⁰ E fault.	53
Photo 18 head of the hammer points NE; photo showing a sinistral N60 ⁰ E fault (with filling) cutting the N-S (N350 ⁰ E) fault.....	53
Photo 19 taken looking NE, it shows two set of faults: N50 ⁰ E/ 45 ⁰ NW (left) cross cutting the N10 ⁰ E/70 ⁰ E (right). Baking effect was observed in the clay (yellow in colour) contact with fault implying that the N50 ⁰ E fault set is younger than the clay rock.....	54
Photo 20 the N28 ⁰ E structure cutting the N100 ⁰ E structure, photo taken looking NE. The N10 ⁰ E fault set is indicated with the white arrow.....	54
Photo 21 the surface rupture observed in the field, north is indicated with the white arrow.	69

List of tables

Table 1 Contributions of each band to the 9 principal components.	25
Table 2 Percentage of information contained in each principal component.....	25
Table 3 Kernel sizes of the Sobel filter.....	27
Table 4 Structural index and corresponding magnetic source models (Reid et al., 1990; Thompson, 1982)	63

Abbreviations

EARS.....	East African Rift System
ASTER.....	Advanced Spaceborne Thermal Emission and Reflection Radiometer
SRTM.....	Shuttle Radar Topography Mission
DEM.....	Digital Elevation Model
Kx.....	filter along the horizontal direction
Ky.....	filter along the vertical direction
X.....	image filtered by Kx
Y.....	image filtered by Ky
NDVI.....	Normalized Difference Vegetation Index

1. Introduction

1.1. Research background

Tectonics is a branch of geology that studies the origin, historical evolution and mutual relations of the regional structures or deformational features of the Earth's crust (Bates and Jackson, 1987; Bates and Jackson, 1995). A subfield of tectonics that deals with young tectonic events which have occurred or are still occurring in a given region after its last significant tectonic setup is called neotectonics (Pavlidis, 1989). In particular, Bates and Jackson (1995) defined neotectonics as the study of post-Miocene structures and structural history of the Earth's crust. The theory of Plate Tectonics states that the outer rigid layer of the Earth, the lithosphere, is divided into several plates that move the earth's surface relative to each other along plate boundaries. There are three primary types of plate boundaries: divergent, convergent and transform plate boundaries. At divergent plate boundaries, lithospheric plates away apart from each other as new crust is created; for example, the East African Rift System (EARS), which is an intra-continental extension where the African Plate is splitting forming the main African Plate and Somalian Plate. At convergent plate boundaries, lithospheric plates move toward each other and one of the plates submerge beneath the other and so the crust is consumed; for example, the Nazca Plate and the South American Plate are colliding each other and the former submerges beneath the latter. Transform plate boundaries are zones where two plates are sliding horizontally past one another; for example, the San Andreas Fault zone.

A rift is a zone of extension, in which a graben of regional extent with long and narrow continental trough is bounded by normal faults resulting from extensional stresses (Bates and Jackson, 1987). A series of tectonically connected rifts are collectively known as a rift system (Olsen and Morgan, 1995). The Rio Grande Rift in south-western US and Rhine Rift in south-western Germany are some examples of a rift, where as the EARS is an example of a rift system. Genetically rifts are classified into either an active or a passive rift. Active rifts are caused by active forces like thermal upwelling of the asthenosphere while passive rifts are the result of extensional stresses (Morgan and Baker, 1983; Rogers, 1993). In active rifts, uplift and volcanism precede rifting whereas in passive rifts, rifting and possibly uplift precede volcanism (Condie, 1997; Sengor and Burke, 1978). Both models of rifting have been proposed for the EARS; however, geophysical and geochemical data as well as timing of magmatic and tectonic evolution of the EARS support the active rifting model (Braile et al., 1995; George et al., 1998; Yirgu et al., 2006).

The EARS extends from Afar depression in the north to Mozambique in the south (Figure 1). In the Afar depression, the EARS meets with the Red Sea and the Gulf of Aden forming a triple junction. The EARS splits into Eastern and Western branches. The Eastern branch starts at the Afar triple junction and crosses Eritrea, Djibouti, Ethiopia, Sudan, Kenya and reaches up to Tanzania. The Eastern branch is further subdivided into series of rifts along its strike. For example in Ethiopia, Kenya and Tanzania, Eastern branches of the EARS are known as Ethiopian Rift, Kenya Rift and Tanzania Rift, respectively.

The EARS is considered as a model of a continental rift that is at the incipient stage of evolution (Chorowicz, 2005). The on-going extension along the rift zone reaches 5-10 mm per year (Skobelev et al., 2004), which is manifested by young faulting, geothermal activity and current seismicity. For example, about 435 earthquakes with magnitudes ranging from 2 to 5 occurred in the Kenya Rift alone in the years 1993-1996 (Achauer and Masson, 2002). In addition, Seht et al.(2001) carried out seismological surveys of the southern Kenya Rift (Lake Magadi area) from November 1997 to June 1998 and demonstrated that the area is seismically active. Furthermore, they reported a surface rupture (without visible displacement) in the northern part of the Lake Magadi area that occurred due to an earthquake during their study period.

Neo-tectonic extension of the EARS is a debated topic and two different models of extensional stress direction have been proposed. The extension direction models are E-W to ESE-WNW (Boccaletti et al., 1998; Fairhead and Girdler, 1972; Hackman et al., 1990; Jestin et al., 1994) and NW-SE, (Bosworth and Strecker, 1997; Bosworth et al., 1992; Chorowicz and Sorlien, 1992; Rosendahl et al., 1992). Extensional stress in the Afro-Arbian Rift System has been investigated by Bosworth and Strecker (1997) and Bosworth et al.(1992) and the results of their studies are summarized in Figure 1. Their studies indicate that there was a change of the extensional stress field in the time span from Miocene to present day from NE-SW to N-S for the northwestern Red Sea and from E-W to NW-SE for central part of the EARS.

Extension along the central Kenya Rift has been studied in more detail compared to extension along the southern part of the Kenya Rift. Hackman et al. (1990) suggested that extensional stress of the central Kenya Rift is oriented E-W to ESE-WNW while Bosworth and Strecker (1997) and Bosworth et al. (1992) proposed that the extensional stress field of the central part of the Kenya Rift changed from NE-SW in the late Miocene to E-W in the Pliocene – mid Pleistocene and the extensional stress field again changed to NW-SE in the late Quaternary. For southern part of the Kenya Rift, a ESE-WNW extensional direction has been suggested by Seht et al.(2001) from focal mechanisms of selected earthquakes and an E-W to ESE-WNW extensional direction by Atmaoui and Hollnack (2003) from joint analysis on two selected sites. The ESE-WNW extension direction by Atmaoui and Hollnack (2003) was deduced in one site only and it is associated with local NW-SE fracture of Precambrian age since the site lies along an old shear zone. However, they recommended further field investigation of the possibility that the ESE-WNW extension could have occurred prior to the NW-SE extension proposed for central part of the Kenya Rift by Bosworth and Strecker (1997) and Bosworth et al.(1992).

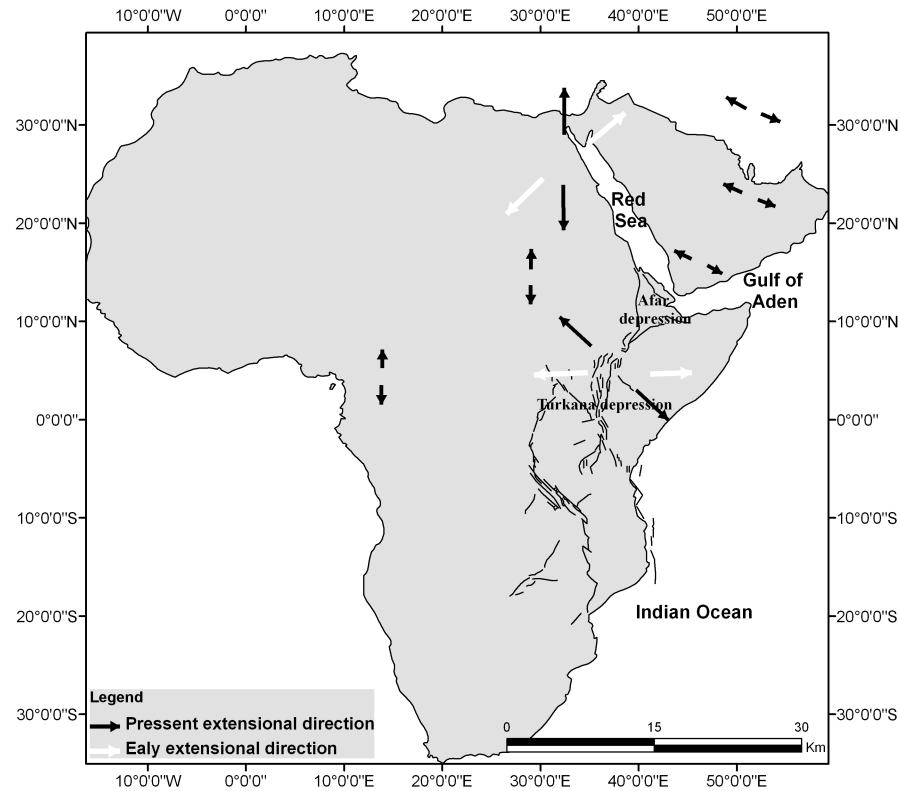


Figure 1 The East African Rift System and associated extensional stresses. Fault traces shown are driven from Chorowicz (2005) and direction of extensional stresses shown are derived from Bosworth and Strecker (1997)

1.2. Research problem

Mapping surface and subsurface faults of the rift is crucial in characterizing its tectonic extension. Proper characterization of tectonic extension of the rift helps to understand seismicity, geothermal activity, volcanicity and general geodynamics of the rift.

In characterizing tectonic extension of a rift, different approaches have been practiced. For example, Kington and Goodliffe (2008) used seismic reflection and magnetic data to characterize rift extension in the Woodlark Basin, Papua New Guinea, while Van Avendonk et al. (In Press) applied seismic and gravity observations to characterize rifting extension in the eastern Grand Banks, Newfoundland. Besides, Lunina and Gladkov (2007) deduced extension along the Barguzin Rift (Baikal region) from field and remote sensing data sets, while Bosworth and Strecker (1997) and Bosworth et al. (1992) integrated field data, hydrocarbon drilling boreholes and tele-seismic earthquake focal mechanisms to characterize extension along the central Kenya Rift.

In the southern part of the Kenya Rift, further neotectonic investigation is required to verify if the NW-SE extension or E-W to ESE-WNW extension represents the recent extensional stress field of the area. The previous neotectonic field study by Atmaoui and Hollnack (2003) did not cover a large area; it was based on two sites only. Besides, their study was limited to surface mapping, which lacks 2D subsurface investigation to properly characterize extension tectonics of the Lake Magadi area. Hence, conjunctive analysis of field and remotely sensed datasets of the Lake Magadi area is essential. Field

data from several locations in a larger area are required in order to obtain representative information about the conditions of extensional stress in the Lake Magadi area. Remotely sensed datasets, which include space-borne multispectral imagery and geophysical (resistivity plus magnetic) data sets are likely to provide useful surface and subsurface geological information, respectively. In the troughs of the Lake Magadi area, the bedrock is covered by soil and sediments, which makes lithological and structural mapping difficult. Thus, subsurface geophysical investigation becomes vital in delineating faults and lithologies in the troughs and visualizing their 2D perspective.

Integration of field and remotely sensed (multispectral and geophysical) datasets enables characterization of surface and 2D subsurface perspective of the faults as well as lithologies in the area. This will help to properly characterize extension tectonics and to unravel the missing knowledge gap on neotectonic extension in the Lake Magadi area as well as to update the geology of the area. Such conjunctive analysis has not been demonstrated in characterizing extension tectonics of the EARS.

1.3. Objectives

1.3.1. General objective

The main objective of this research was to contribute to the understanding of the neotectonic extension of the Lake Magadi area by conjunctive analysis of field collected and remotely sensed (multispectral and geophysical) datasets.

1.3.2. Specific objectives

In order to achieve the main objective of the study, the following specific objectives were set:

- To characterize the spatial distribution and orientations of the surface faults from remotely sensed and field collected datasets.
- To integrate results of surface and subsurface investigations of faults and lithologies in the Lake Magadi area.

1.4. Research questions

The proposed study seeks to answer the following questions:

- Do the field and remotely sensed data sets support the NW-SE or E-W to ESE-WNW extensional neotectonics in the southern Kenya Rift?
- What is the implication of the recent surface rupture observed by Seht et al.(2001) on the neotectonics of the southern Kenya Rift?

1.5. Hypothesis

Two different models of neotectonic extensional direction (NW-SE and E-W to WNW-ESE) have been proposed for the Kenya Rift and the whole EARS. However, there is a knowledge gap in the understanding of neotectonics of the southern Kenya Rift since previous works in the area were based on limited field sites and they lacked subsurface investigations. In the study area, faults extracted from spaceborne data correlate with faults observed in the field and extracted from ground geophysical data. Conjunctive analysis of these datasets provide surface and subsurface information with 2D perspective that would enable characterization of the neotectonic extension in the Lake Magadi area and would aid in unravelling the missing knowledge gap on neotectonic extension in the area as well as in updating the geology of the area.

1.6. Datasets and Methodology

1.6.1. Data sets & Softwares

The data sets used in the study include:

- 1) ASTER datasets
- 2) SRTM DEM
- 3) Aeromagnetic data
- 4) Ground survey magnetic data
- 5) Resistivity data
- 6) Geological maps
- 7) Location of earthquake epicenters
- 8) Field data

Softwares used:

- ERDAS imagine 9.2
- ENVI 4.4
- Rockware (rose diagram)
- Arc GIS 9.3
- Geosoft Oasis Montaj 7
- Earth imager
- WinTensor

1.6.2. Methodology

To answer the above questions and achieve the aforementioned objectives, the following approaches (Figure 2) were followed:

- A) **Literature Review:** relevant literature on geology, tectonics, geophysics and remote sensing were reviewed in order to understand previous works about the geologic and tectonic aspects of the study area and to choose appropriate techniques as well as datasets for achieving the research objectives and answering research questions.

- B) **Digitizing geological maps:** existing geological maps of the area were manually digitized. The maps used geological maps include i) 1: 125000 scale map by Baker, (1958) and ii) 1: 750000 scale map by Baker et al., (1971).
- C) **Processing of remote sensing datasets:** included processing of ASTER images, ASTER DEM and SRTM DEM in order to extract structural and lithologic information.
- D) **Field work:** this included validation of faults and lithologies and collection of structural data. Besides, field magnetic survey and 2D resistivity profiling of selected sites were conducted.
- E) **Analysis of structural data:** structural data collected (strike and dip of faults and slicken-sides) in the field were analyzed and interpreted.
- F) **Geophysical data processing and interpretation:** aeromagnetic data, ground magnetic and resistivity datasets were processed and interpreted using the Oasis montaj and Earth imager software packages.
- G) **Integrated analysis:** Interpretations of the different datasets were integrated in order to characterize surface and subsurface nature of the faults as well as lithologies and then deduce neo-tectonics of the area.

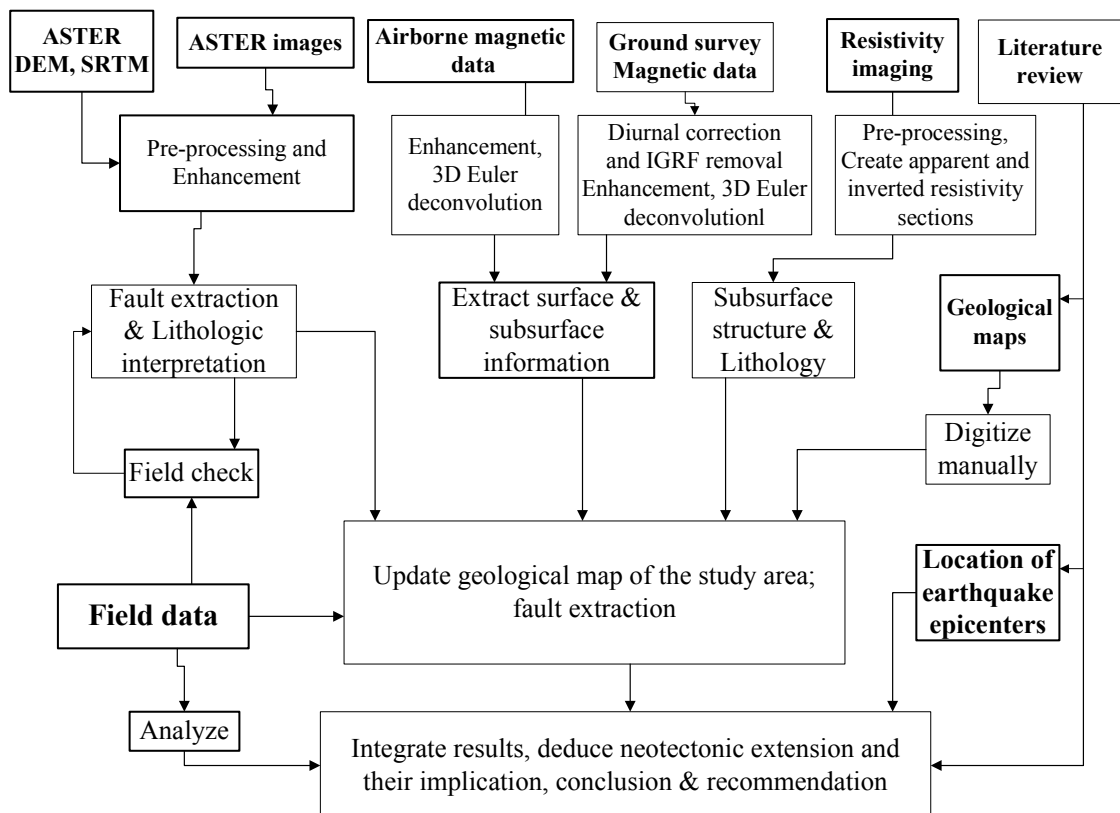


Figure 2 Flow chart of methodology and the procedures followed

1.7. Outline of the thesis

The thesis is outlined in seven chapters. **Chapter one** gives the overall introduction of the thesis. **Chapter two** discusses previous geological, geophysical and remote sensing works done in the region as well as in the study area; **Chapter three** deals with processing and analysis of ASTER datasets and SRTM DEM. **Chapters 4** deals with analysis and discussion of field data. **Chapter 5** explains the theoretical background of the geophysical techniques and processing and analysis of the geophysical datasets. **Chapter 6** discusses results of the remote sensing, geophysical and field data analysis as well as their integration. **Chapter 7** gives conclusions and recommendations.

2. Literature Review

2.1. Location of study area

The study focuses on Lake Magadi area in the southern part of the Kenya Rift which is an eastern branch of the EARS (Figure 3). The study area is an arid land located in the Kaliado district about 100 km southwest of Nairobi. It stretches from 1°30'S to 2°05'S latitudes and from 35°08'E to 36°27'E longitudes. The rift in the Lake Magadi area stretches N-S with Nguruman escarpment to the west, Olorgesailie volcano to the east and Shombole and Lenderut volcanoes to the south. The rift floor has horst and graben structures. The horsts are occupied by volcanic rocks while the grabens are filled by a lake and sediments. The lake in the central part of the rift area has an elevation of about 615m above sea level. It is known as Lake Magadi, from which large amounts of soda is extracted by the Magadi Soda Company.

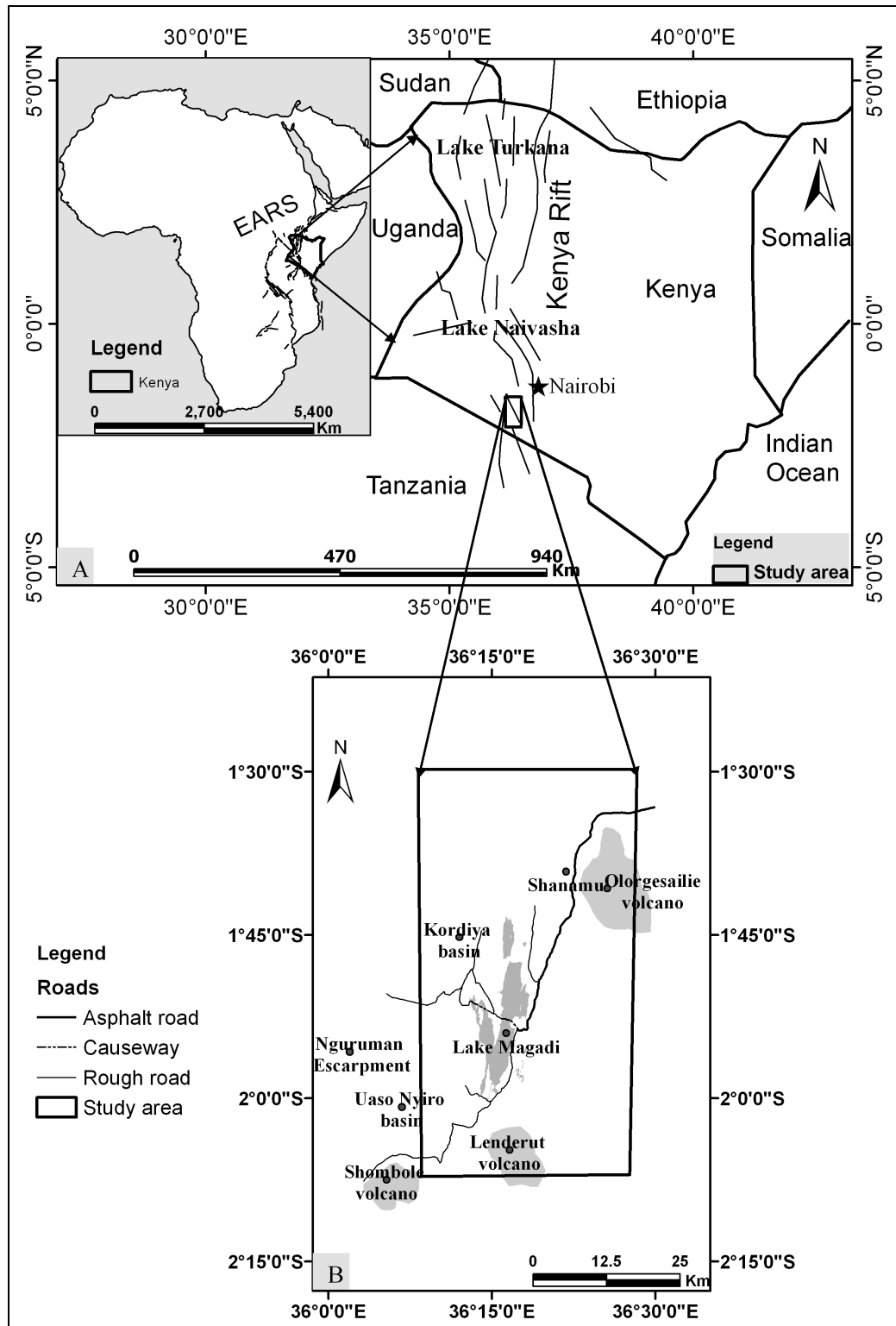


Figure 3 A) Location of the Kenya Rift in the East African Rift System (EARS). Fault traces are derived from Chorowicz (2005). B) Location of the Lake Magadi area in the Kenya Rift.

2.2. Volcanic and tectonic evolution of the EARS

The evolution of the EARS is explained by an active model of rifting, which is supported by geophysical and geochemical data as well as by the timing of magmatic and tectonic events during the Cenozoic (Braile et al., 1995; George et al., 1998; Yirgu et al., 2006). The EARS is characterized by deep rifts and voluminous volcanism manifested by volcanoes in many areas (Keller et al., 1994; Mariita and Keller, 2007). Such abundant volcanism along the EARS is related to plumes (Chorowicz, 2005; Keller et al., 1994). The existence of hot asthenosphere plumes and crustal intrusions beneath the EARS is revealed by seismic and gravity models (Achauer and Masson, 2002; Braile et al., 1995; Mariita and Keller, 2007; Yirgu et al., 2006). The two known plumes along the EARS are the Afar and Kenya mantle domes (Figure 4), which are separated by the Turkana Depression in the northern part of Kenya and southernmost part of Ethiopia (Furman, 2007; Furman et al., 2004). Besides, geochemical data supports the existence of two compositionally distinct mantle plumes beneath the EARS; the first volcanism of the Kenya plume occurred during Eocene in the Turkana area, while the first volcanic manifestations for the Afar plume are Oligocene flood basalts that cover present day Ethiopia, Eritrea, Djibouti and Yemen (Rogers et al., 2000). Succeeding the respective volcanisms, extension started at ~25Ma in the Turkana area (George et al., 1998; Morley et al., 1992; Wolfenden et al., 2004) and at ~11Ma in the Afar depression (Chernet et al., 1998; Wolfenden et al., 2004).

The volcanic rocks in EARS have been deposited pre-rift, syn-rift and post-rift periods (Furman, 2007). The oldest recorded volcanic activity in the EARS is 40–45Ma (Eocene) in the Turkana Depression (Ebinger et al., 2000; Ebinger et al., 1993; Furman, 2007; George et al., 1998; Yirgu et al., 2006). Afterwards, the Turkana Depression became volcanically active and it was followed by the late Oligocene flood basalts, which are associated with the break-up of the Afro-Arabian continent (Furman, 2007; George et al., 1998; Ukstins et al., 2002). The break-up of the Afro-Arabian continent resulted in the formation of the Red Sea during ~28 Ma (Furman, 2007; Wolfenden et al., 2004; Yirgu et al., 2006), the Gulf of Aden during ~35 Ma (Watchorn et al., 1998) and the EARS, which represents the third arm of the triple junction (Furman, 2007).

The earliest extension documented in the EARS occurred in the Turkana area during ~25 Ma; associated volcanism and faulting propagated from this region to the north and south (Furman, 2007; George et al., 1998; Morley et al., 1992; Wolfenden et al., 2004; Yirgu et al., 2006). Cenozoic volcanism is widespread in the northern part of the EARS but it becomes sparse in the southern parts (Chorowicz, 2005). Miocene (19–11 Ma) was an event of volcanism in southern Ethiopia (Ebinger et al., 1993; George et al., 1998). At about 11 Ma, volcanism occurred in the central and northern portions of the Main Ethiopian Rift and was followed by the commencement of rifting and development of the Afar triple junction (Chernet et al., 1998; Wolfenden et al., 2004). On parallel geologic event, magmatism and rifting developed from the Turkana depression southward to the Western Rift and the Kenya Rift (Baker et al., 1971; Bosworth et al., 1992; Kampunzu et al., 1998) and further toward Tanzania at about 1 Ma (Furman, 2007; Nonnotte et al., 2008).

The existing neo-tectonic extension models of the EARS are summarized as E-W to ESE-WNW (Boccaletti et al., 1998; Fairhead and Girdler, 1972; Hackman et al., 1990; Jestin et al., 1994) and

NW-SE (Bosworth and Strecker, 1997; Bosworth et al., 1992; Chorowicz and Sorlien, 1992; Rosendahl et al., 1992). During Miocene to Recent times, the extensional stress fields along the Afro-Arabian Rift System have re-oriented together with the well-documented stress fields in the Tanzania Rift, Kenya Rift, Red Sea and Gulf of Suez during the Late Pleistocene (Bosworth and Strecker, 1997). In the Gulf of Suez and northern Red Sea, the extensional stress field changed from NE-SW to N-S after 125ka (Bosworth and Strecker, 1997). The extensional stress field changed from E-W in the Late Pleistocene to NW-SE in present day in the Kenya Rift (Bosworth and Strecker, 1997; Bosworth et al., 1992) and in the Malawi Rift (Chorowicz and Sorlien, 1992).

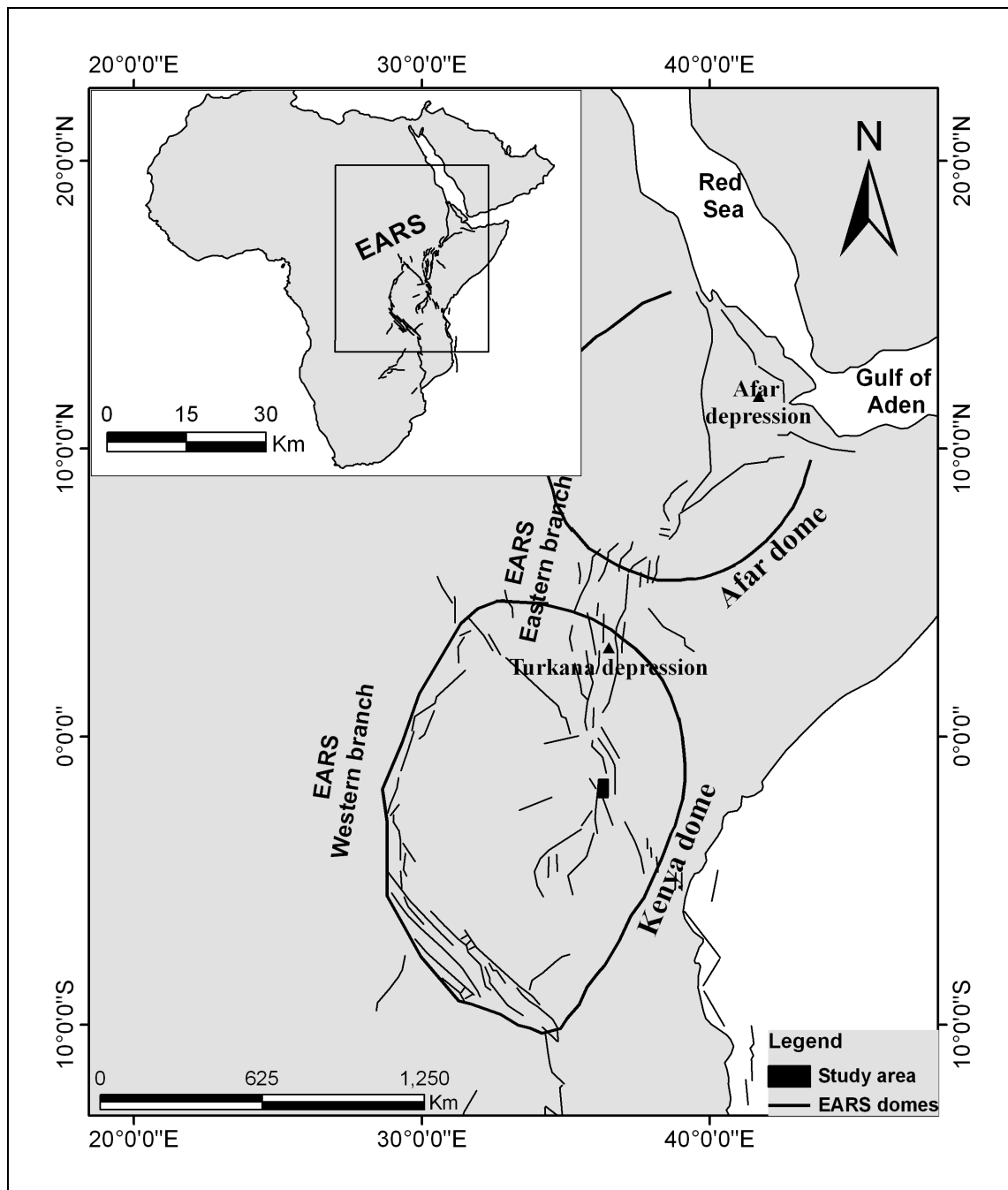


Figure 4 Location of the Afar and Kenya domes (Furman, 2007; Macdonald et al., 2001; Rogers et al., 2000) in the East African Rift system (EARS).

2.3. Tectonic setting and geology of the Kenya Rift

2.3.1. Tectonic setting of the Kenya Rift

The Kenya Rift is a prototype of a continental rift in the early stages of rifting (Achauer and Masson, 2002), which is evidenced by the presence of hot springs (Jones, 1996) and earthquakes (Hollnack and Stangl, 1998; Seht et al., 2001).

As shown in Figure 3, the Kenya Rift is subdivided into sub-basins along its strike (Achauer and Masson, 2002). The northern part (Lake Turkana area) is further split into two parallel N10⁰E trending rift valleys having elevation of about 1050m while central part of the rift (Lake Naivasha area) has a trend direction of N150⁰E and the elevation reaches about 2100m. Going further south (Lake Magadi area) the rift valley drops to an elevation of about 600m and trend of the rift is NNE.

In the Kenya Rift, volcanism and rifting started, respectively, at 40-45Ma and ~25Ma ago in the north (Turkana area) and propagated southward. In the southern parts of the Kenya Rift, volcanism took place in the last 15Ma and structural evolution started 7Ma ago resulting into formation of a graben during 4 - 3 Ma (Baker, 1986; Crossley and Knight, 1981). Regional seismic and gravity studies indicate that the crustal thickness in the Kenya Rift decreases from 35 km in the south to 22 km in the north (Achauer and Masson, 2002; Mariita and Keller, 2007; Mechie et al., 1994; Mechie et al., 1997), indicating increased crustal extension in the north and the later southward migration of crustal extension.

According to Hackman et al. (1990), the extensional stress field in the central part is oriented E-W to ESE-WNW while Bosworth and Strecker (1997) and Bosworth et al. (1992) proposed that the extensional stress field was re-oriented from NE-SW in the late Miocene to E-W in the Pliocene – Mid Pleistocene and the extensional stress field further changed to NW-SE in the late Quaternary. For southern part of the Kenya Rift, a ESE-WNW extensional direction has been suggested by Seht et al.(2001) from focal mechanisms of selected earthquakes and an E-W to ESE-WNW extensional direction by Atmaoui and Hollnack (2003) from joint analysis on two selected sites. The ESE-WNW extension direction by Atmaoui and Hollnack (2003) was deduced in one site only and it is associated with local NW-SE fracture of Precambrian age since the site lies along an old shear zone. However, Atmaoui and Hollnack (2003) recommended further field investigation of the possibility that the ESE-WNW extension could have occurred prior to the NW-SE extension proposed for the central part of the Kenya Rift by Bosworth and Strecker (1997) and Bosworth et al.(1992).

The southern Kenya Rift is seismically active (Achauer and Masson, 2002; Seht et al., 2001). Seht et al.(2001) carried out seismological surveys of the southern Kenya Rift (Lake Magadi area) from November 1997 to June 1998 and reported earthquake swarms in the area (Figure 5). Epicentres of the earthquake swarms show clustering in the northern part of the Lake Magadi area where Seht et al.(2001) observed a surface rupture that occurred due to an earthquake during their study period.

Besides, their study show that depth of the earthquakes vary from 9km to 27km in northern (from the cluster of earthquake swarms) and in southern part of the Lake Magadi area, respectively. Seht et al.(2001) associated the cluster and the shallow depth of hypocenter with the presence of lower crustal magmatic intrusion beneath the cluster.

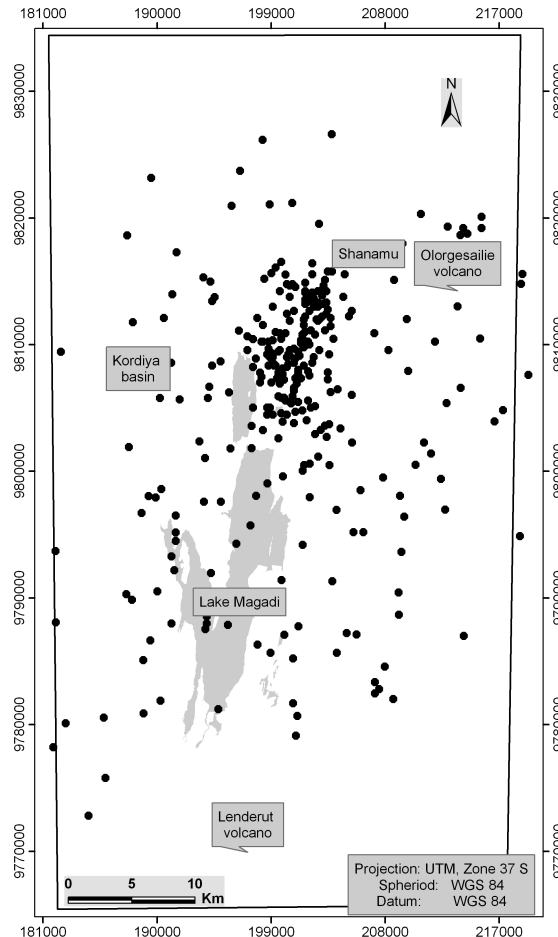


Figure 5 Epicenter locations of the earthquake swarms (Seht et al., 2001)

2.3.2. Geology of the Kenya rift

The Kenya rift is characterized by late Cenozoic volcanic and sedimentary rocks overlying the Neoproterozoic rocks (Bosworth et al., 1992). However, the oldest volcanic activity of 40-45Ma age has been reported in the Turkana area in the northern part of Kenya Rift (Ebinger et al., 2000; Ebinger et al., 1993; Furman, 2007; George et al., 1998; Yirgu et al., 2006), extending the age range of volcanic rocks in northern Kenya Rift to Eocene. Besides, the earliest extension inferred in the Turkana area is at about 25 Ma (Furman, 2007; George et al., 1998; Morley et al., 1992; Wolfenden et al., 2004).

According to Baker et al. (1971), the late Cenozoic volcanic rocks in the Kenya Rift is divided in to four litho-stratigraphic units: Miocene basalts, Miocene phonolites, Pliocene volcanic rocks and Quaternary volcanic rocks and sedimentary deposits. After the commencement of extension in the Turkana area, the oldest volcanic rock unit in the central and northern parts of the Kenya Rift is the

Miocene (23-14Ma) basalt, which is overlain by 14-6.2 Ma phonolites (Baker et al., 1971; Bosworth et al., 1992). Phonolites represent the oldest Tertiary volcanic rocks in the southern part of the Kenya Rift (Baker et al., 1971). The third unit comprises Pliocene volcanic rocks, which are composed of trachytes, phonolites and nephelinites covering the central and southern parts of the Kenya Rift, where as the Pliocene basalts occur along whole length of the rift. The fourth and youngest unit in the Kenya Rift includes late Pliocene to Quaternary volcanic rocks (trachyte in the rift valley floor and basalt in the eastern fringes of the rift) as well as Quaternary sedimentary deposits (Baker et al., 1971; Bosworth et al., 1992; Chorowicz, 2005).

The northern part of the Kenya Rift is characterized by volcanic rocks consisting of pyroclastics, tuffs, trachytes, rhyolites and basalts with an intervening volcanic cone (Macdonald, 1994). The central part of the Kenya Rift is covered by a Miocene sequence of mafic volcanic flows with substantial intercalations of sedimentary sequences (Behrensmeyer et al., 2002). In addition to the Quaternary volcanic rocks and sediments (Ngecu and Njue, 1999), the southern part of the Kenya Rift has Basement rock exposures along its western and eastern flanks (Baker and Mitchell, 1976; Simiyu and Randy Keller, 1998).

Geology of the Lake Magadi area

Integrated interpretations of geological, seismic, drill hole and gravity data by Simiyu and Keller (1998) reveal the upper crustal structures in the Lake Magadi area. Their model shows Basement rocks at the bottom (outcropping at western and eastern flanks of the rift) overlain by Miocene-Pliocene volcanic and sediments, plateau trachytes, phonolites and basalts, Pleistocene-Recent pyroclastics and sediments. Regional geology of the Lake Magadi area has been summarized by Baker and Mitchell (1976) as shown in Figure 6.

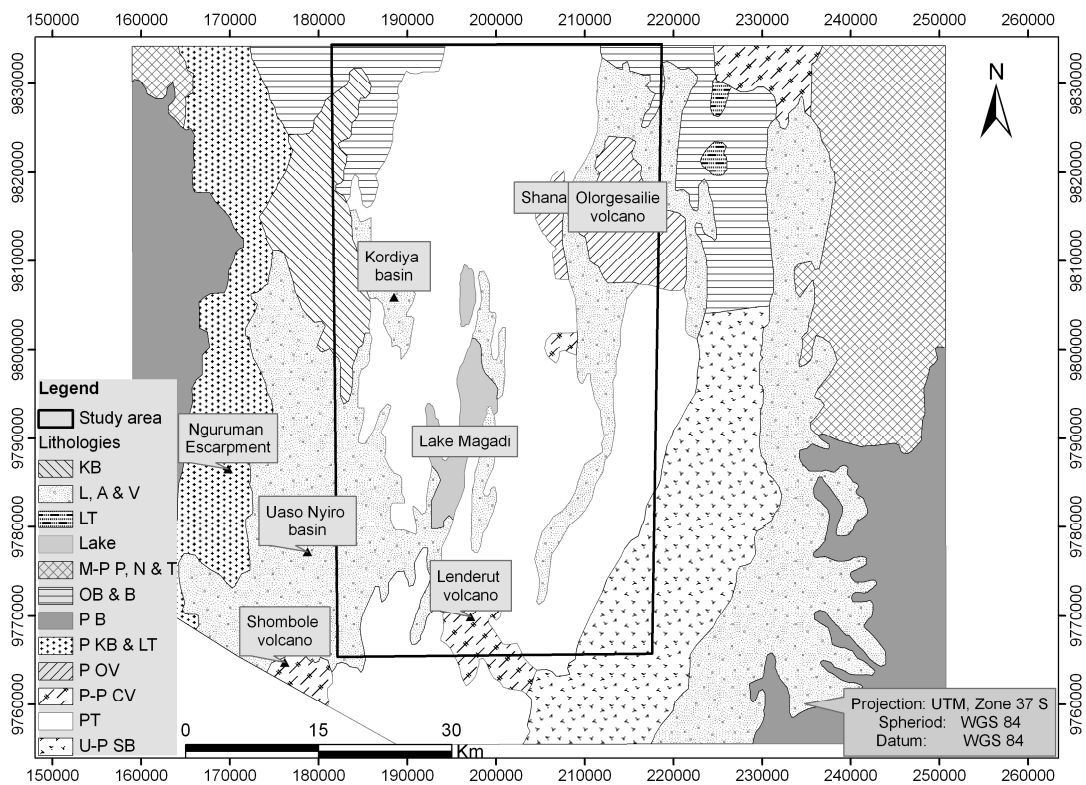


Figure 6 Regional geologic map of the Lake Magadi area after Baker and Mitchell (1976). The abbreviations used in the legend are explained below.

<u>Abbreviations</u>	<u>Lithologies</u>
L, A & V	Lacustrine sediments, alluvium, volcanic ash
LT	Limuru trachytes
M-P P, N & T	Miocene-Pliocene phonolites, nephelinites and trachytes (pre-rift)
OB & B	OI Tepsi basalts and benmoreites
P-P CV	Pliocene-pleistocene central volcanoes
P B	Precambrian basement
P KB & LT	Pliocene Kirikiti basalts and Lengitoto trachytes
P OV	Pliocene Ologesaile volcanics
PT	Plateau Trachytes
U-P SB	Upper Pliocene Singarani basalts

The geology of the Lake Magadi area has been surveyed by Baker (1958) and the lithological units has been classified into Basement rocks, volcanic rocks, lake beds and lake sediments accumulated in the troughs (Figure 7).

Baker reported that the Basement rocks are composed of schists, gneisses and quartzites outcropping at a far western part of the Lake Magadi area known as Nguruman escarpment. The basement rocks are overlain by conglomerates and sandstones.

The volcanic rocks are classified into Miocene – Pliocene nephelinites, phonolites and trachytes, Pliocene Kirikiti basalts, Lengitoto trachyte, Ologesailie lavas, Ol Keju Nero and Singaraini basalts and Early Pleistocene plateau-type alkali trachytes (Baker, 1958; Baker, 1986; Baker and Mitchell, 1976; Baker et al., 1971).

In the southern part of the Kenya Rift, volcanism started about 15 Ma ago with the eruption of nephelinites, phonolites and trachytes (Baker, 1986; Baker et al., 1971); these Miocene – Pliocene rocks outcrop in the northwestern and northeastern flanks of the Lake Magadi area (Baker and Mitchell, 1976).

In the meantime structural evolution of the southern rift was progressing. It started about 7 Ma ago with Nguruman faulting, which resulted in the formation of a half graben that developed into a full graben at about 4-3 Ma (Baker, 1986).

During Pliocene, volcanism in the Lake Magadi area was mainly basaltic and trachytic in composition (for example: Kirikiti basalts, Lengitoto trachyte, Ologesailie lavas, Ol Keju Nero and Singaraini basalts). The Kirikiti basalts occur in the Nguruman escarpment lying unconformably on the eastward slopes of the Basement rocks. The Kirikiti basalts are overlain by the Lengitoto trachyte (Baker, 1958). In the eastern part of the Lake Magadi area there is a central type of volcano known as Ologesailie, which is the highest mountain in the area. This volcano is made up of a pile of lavas consisting of basalts, trachyandesites, alkali trachytes and nephelinites (Baker, 1958; Baker et al., 1971). These Ologesailie lavas are overlain by Ol Keju Nero and Singaraini basalts which are correlated with the Kirikiti basalts (Baker, 1958). Moreover, Baker's field observation indicates that the faulting in the eastern side of the Rift began after the Ologesailie vulcanicity. Thus, during the Pliocene period the floor of the Rift Valley must have been partly covered by Kirikiti basalt and Lengitoto trachyte, Ol Keju Nero and Singaraini basalts overlying the Ologesailie lava.

In the Plio-Pleistocene age, an extensive period of extrusion of plateau-type alkali trachytes occurred and covered greater part of the rift floor. Vulcanicity of the plateau trachyte ended with the formation of a number of small ash and scoriaceous lava cones (Baker, 1958; Baker et al., 1971).

A cherty rock consisting largely of silicified bedded clays was deposited on top of the plateau trachytes. Then during the Pleistocene time thin layers of lake beds known as the Oloronga Beds were deposited unconformably on the chert unit (Baker, 1958; Baker, 1986). The Oloronga Beds, which consist of cherts, silts, clays as well as reworked volcanic dust and debris (Baker, 1986) cover the northern and southern ends of Lake Magadi area. The deposition of the Oloronga Beds was followed by a series of sub-parallel faulting that resulted in the creation of the rift floor of the Lake Magadi area with several subsidiary fault troughs. In the Middle Pleistocene, lake sediments were accumulated in the fault troughs. The lake beds in Ologesailie area are diatomaceous clays with artifacts of Middle Pleistocene age whereas the lake beds in Uaso Nyiro depression are fine silts and clays.

A period of further lake deposition was confined to the Magadi trough and the Uaso Nyiro basin while in other fault troughs, lacustrine gravels and clays were deposited (Baker, 1958). In the Magadi trough, fine silts and clays (the High Magadi Beds) were laid down to a level 12 m higher than the

present surface of the lake. Finally, the onset of alkaline spring activity, together with the accumulation of mud resulted in the deposition of a series of beds of sodium carbonates intercalated with clays forming the Evaporite series, which is still in the process of formation at the present day (Baker, 1958).

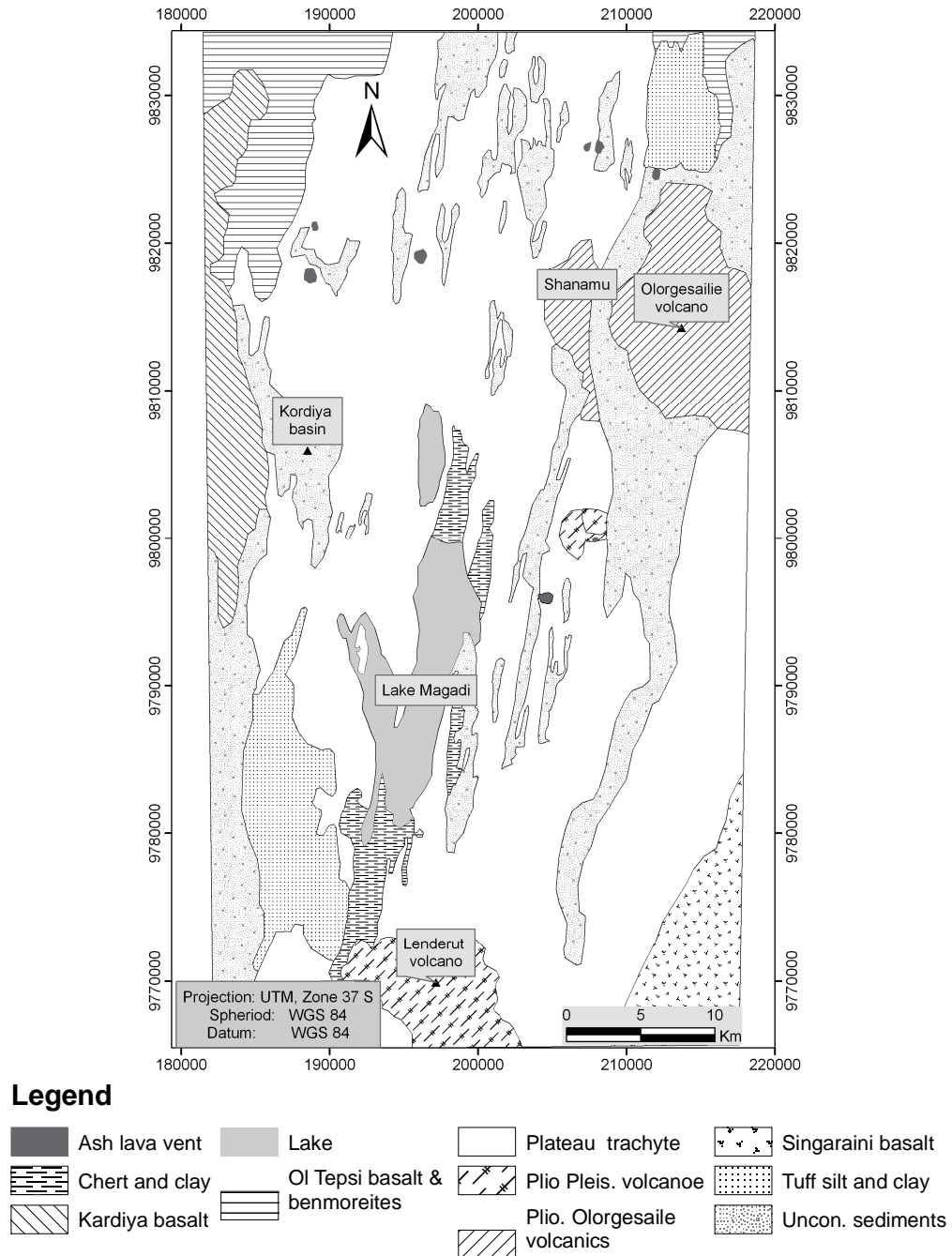


Figure 7 Detail geologic map of the Lake Magadi area after Baker and Mitchell (1976) and Baker (1958).

2.3.3. Remote sensing and geophysical works on the Kenya rift

Some researchers used remote sensing datasets to understand the tectonic and geologic aspects of the Kenya Rift. Le Turdu et al. (1999) used SPOT images to illustrate the influence of pre-existing structures on the evolution of extensional faults of the Kenya Rift. Jutz and Chorowicz (1993) integrated SPOT and Landsat images to map geological and structural units of the Kenya Rift. Vétel et al. (2005) portrayed morphology and fault geometry of the northern Kenya Rift from SRTM and Landsat image. Besides, Gloaguen et al.(2007) demonstrated object oriented automatic fault extraction technique and performed fractal analysis of radar datasets in the southern part of the Kenya Rift. Atmaoui and Hollnack (2003) deduced the neotectonic extension of the Lake Magadi area by integrating remote sensing and field data; however, their study had limited field sites so that they recommended further field investigations.

Geophysical in the Kenya Rift had focused on the understanding of seismicity as well as crustal and upper mantle structures of the Kenya Rift. Henry et al. (1990), Mechie et al. (1994) and Mechie et al (Mechie et al., 1997) depicted crustal structures beneath the Kenya Rift by using seismic profiling data. Mariita and Keller (2007) deduced crustal and upper mantle structures in the northern part of the Kenya Rift by integrating gravity, seismic refraction, seismic reflection, aeromagnetic, and geologic and drilling datasets. Bosworth and Strecker (1997) and Bosworth et al.(1992) integrated field data, hydrocarbon drilling boreholes and tele-seismic earthquake focal mechanisms in order to characterize the extension stresses the central part of the Kenya Rift. For the southern Kenya Rift, Simiyu and Keller (1998) characterized the upper crustal structures by integrating geology, borehole data, gravity and seismic data, while Byrne et al. (1997) used reflection and refraction seismic profiles in order to depict the upper mantle structure. Hollnack and Stangl (1998) and Seht et al. (2001) studied the seismicity of the southern Kenya Rift, while Reeves (1989) interpreted aeromagnetic data in southeastern Kenya.

3. Processing and analysis of the remote sensing datasets

Remote sensing aids geological mapping of large areas that could not be managed through conventional field work. The remote sensing datasets used in this study include SRTM DEMs, ASTER DEMs and ASTER images. SRTM is acquired by radar technology at a resolution of 90m whereas ASTER DEM is acquired at 30m resolution from the stereoscopic view provided by ASTER bands 3N (forward view) and 3B (backward view). Owing to their diverse sensor technology and their different spatial resolutions, the SRTM and ASTER DEMs provide complementary valuable structural information. ASTER images cover three wavelength ranges; bands 1-3 in the visible and near infrared range (VNIR) between 0.52 and 0.86 μm , bands 4 - 9 in the shortwave infrared range (SWIR) between 1.6 and 2.43 μm and bands 10-14 in the thermal infrared range (TIR) between 8.125 and 11.65 μm , with corresponding resolutions of 15m, 30m and 90m, respectively (Abrams, 2000; Thurmond et al., 2006). Since ASTER image has high spectral and spatial resolution, it is useful for discriminating lithological units and mapping geological structures.

In satellite images, rocks and their constituent minerals and other earth materials have different reflection and absorption features. For example, transition metals particularly iron and chlorophyll-bearing vegetation display absorption spectra in the VNIR bands, carbonates and hydroxyl minerals show absorption features in the SWIR bands whereas quartz and feldspars have absorption spectra in the TIR bands (Drury, 2001; Rowan and Mars, 2003). Such spectral features are crucial in identifying rock units and geological structures that aids in geological mapping.

3.1. Pre-processing of the remote sensing datasets

In image processing and data analysis, pre-processing is a crucial step. The following pre-processing activities were performed:

- Removal of bad values from the SRTM and ASTER DEMs.
- Mosaicing of ASTER DEM scenes and subsetting the study area.
- Mosaicing of SRTM scenes and subsetting the study area.
- Co-registration of the datasets to WGS 84 zone 37S
- Layer stacking to create colour composites of ASTER Images. This involved re-sampling the TIR and SWIR bands to the spatial resolution of the VNIR bands (15m).
- Mosaicing of ASTER Image scenes and creating subset of the study area.
- Stretching of images to improve visualization.

The ASTER image scenes used were:

- AST_L1B_00301232007080055_20080704132348_5571
- AST_L1B_00301232007080046_20080704132338_5514

The ASTER DEMs used were:

- AST14DEM_00302242007080108_20080904030332_4671
- AST14DEM_00308232006080633_20080904030332_4668
- AST14DMO_00303082003080724_20081027094344_7041

3.2. Enhancement methods

Several image enhancement techniques can be used in order to improve interpretation and extraction of structural and lithological information from the remote sensing datasets. Some examples include principal components analysis (PCA), derivatives of DEM (slope, aspect and shaded relief), colour composites, spatial domain filtering and integration of different datasets. Application of PCA, colour composites, band ratios and spatial domain filtering enhance lineaments from multispectral satellite images and enable extraction of structural as well as lithologic information (Arlegui and Soriano, 1998; Suzen and Toprak, 1998; Won-In and Charusiri, 2003). Moreover, application of PCA, colour composites and band ratios enhance lithologic and structural information from ASTER dataset (Gani and Abdelsalam, 2006; Gomez et al., 2005; Qari et al., 2008; Rowan and Mars, 2003; Rowan et al., 2005). Obtaining derivatives of DEM (eg. slope, aspect and shaded relief) also enhance lineaments from SRTM (Ganas et al., 2005; Gloaguen et al., 2007; Jordan and Schott, 2005). Furthermore, lithological and structural information can be extracted better by fusing a DEM with multispectral images (Gani and Abdelsalam, 2006; Owusu et al., 2006; Thurmond et al., 2006; Van Roij et al., 2006).

In this research, different enhancement methods have been used since a single enhancement technique may not provide optimum structural and lithologic information. Colour composite, band ratio, spatial domain filtering, PCA, derivatives of DEM (slope and shaded relief) and dataset integration were used to enhance lithological and structural information from the ASTER datasets and SRTM DEM.

Faults and lithologies were interpreted visually and digitized manually from enhanced remote sensing data sets.

3.2.1. Enhancement of ASTER images

Color composite and band ratio analysis

Colour combination enhances interpretability of an image since the human eye can distinguish more colours than grey. Appropriate bands of ASTER imagery were selected for analysis by considering resolution and relevance of the bands for lithological and structural interpretations. For example, colour composite images were prepared by combining the bands in VNIR, SWIR and TIR ranges. The RGB composites of 6-2-1 and 2-3-12 (Figure 8) were used since they enhanced structures and lithologic units better than other RGB composites. Both images were pan-sharpened with a hill-shaded image of ASTER DEM. The ASTER colour composites were good in discriminating the

sediments from each other and from the volcanic rocks; however, they were not useful in discriminating between the different types of volcanic rocks except the volcanoes due to their unique texture.

In the RGB colour composite 6-2-1 (Figure 8 A), tuff silt and clay appear as white whereas chert and clay appear as light blue. Volcanic rocks appear as various shades of brown except in vegetated areas and where they are covered with alluviums where they appear as deep blue and yellow, respectively. The RGB colour composite 2-3-12 (Figure 8 B) was also not useful in differentiating the volcanic rocks in the area because they all appear as blue with no textural difference. However, with the 2-3-12 band combination, sediments and vegetation are better enhanced; chert and clay appear as red, vegetation as green and tuff silt and clay as light red. Structures are shown as prominent ridges in both colour composites.

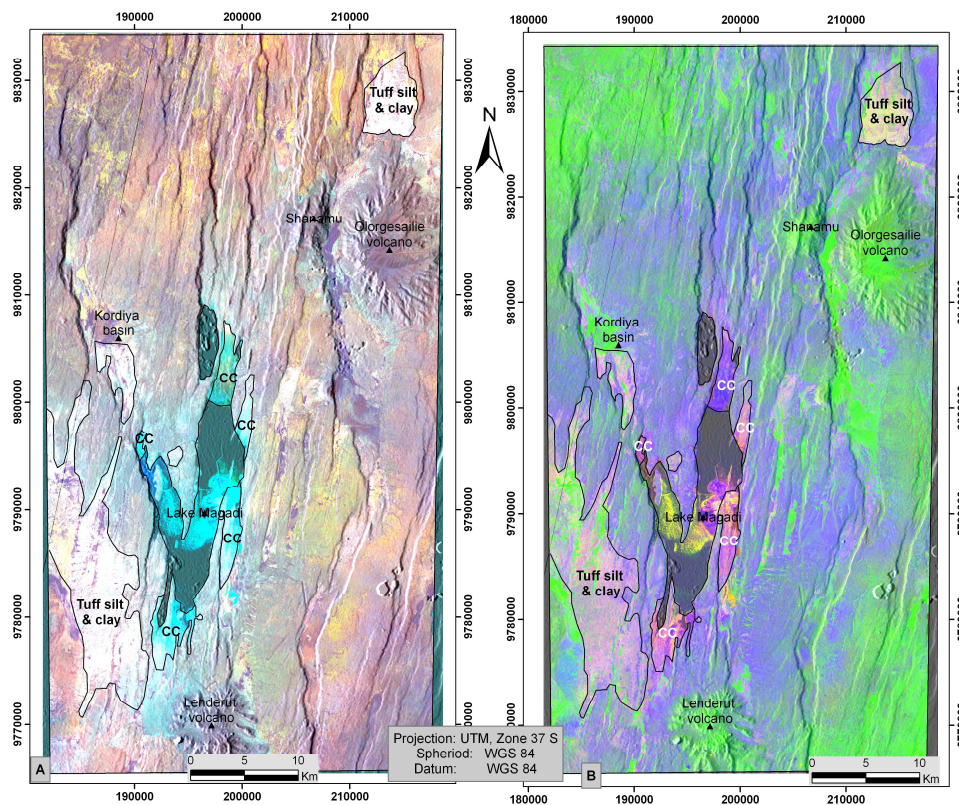


Figure 8 RGB colour composite of ASTER bands 6-2-1 (A) and 2-3-12 (B). Both images were pan-sharpened with hill-shade of ASTER DEM. The identified units are labeled on the image where CC represents Chert and clay.

Besides colour composite of single bands, colour composites of band ratios were analysed. Band ratios 2/1, $(11 \cdot 11) / (10/12)$ and 4/6 enhance iron bearing, silica bearing rocks and clay minerals, respectively. However, high values of 4/6 could also be due to vegetation. Thus, in order to assess the distribution of vegetation in the area, image of Normalized Difference Vegetation Index (NDVI) was used. NDVI is equal to $(NIR - RED) / (NIR + RED)$, which is equivalent to $(b3 - b2) / (b3 + b2)$ based on ASTER images. Ultimately, an RGB colour composite of 2/1 - NDVI - 4/6 was created. In the RGB

colour composite 2/1-NDVI-4/6 (Figure 9 A), vegetation appears as light blue while the chert and clay (outlined in black and labelled as CC) appear as pink and the lake appears as green. Tuff silt and clay as well as alluvium and volcanic rocks appear as red, which implies that iron-bearing minerals exist in the different rocks as well as in the alluvial cover in the area. Figure 9 B shows image of silica index calculated using thermal bands $(11*11)/(10/12)$ (Kalinowski and Oliver, 2004). High ratios in the image indicate higher silica content and appear as white in the image; thus, the rock units in central part of the study area have higher content of silica which implies the presence of acidic rocks in those particular areas. On the other hand, the gray to dark colour in the image indicates lower silica content signifying that those areas are covered by mafic, intermediate rocks or vegetation. To verify if mafic rocks exist, the airborne magnetic data has been used and it is explained in section 5.1.1.

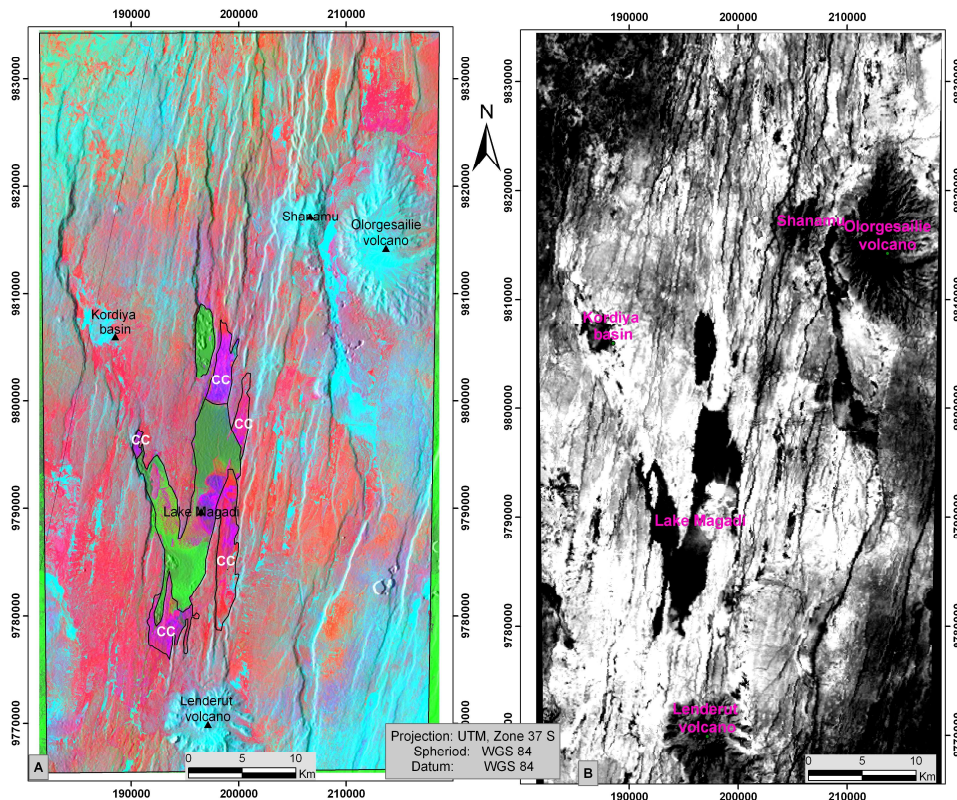


Figure 9 RGB color composite of (A) 2/1-NDVI-4/6 pan sharpened with hill-shade, CC represents Chert and clay; (B) band ratio of $(11*11)/(10/12)$

Principal component analysis (PCA)

PCA is a means of removing redundant information from highly correlated multi-spectral remote sensing data (Drury, 2001) so that it enhances geological information and enables discrimination of structures and lithologies.

PCA was applied on bands 1 to 9 of the ASTER imagery and the result is summarized in Table 1 and Table 2. Contributions of each band to the nine principal components (Table 1) show that the first four components are mainly contributed from the VNIR bands and band 4 while the principal components 5 to 9 are mainly contributed from the SWIR bands. As shown in Table 2, the first four principal components (PC1, PC2, PC3 and PC4) have higher contribution where as the remaining five

components (PC5 to PC9) have very low contribution (less than 0.1%) and their images were dominated noise so that they were insignificant for geologic classification.

Table 1 Contributions of each band to the 9 principal components.

	Band 1	Band 2	Band 3	Band 4	Band 5	Band 6	Band 7	Band 8	Band 9
PC 1	0.65	0.16	-0.69	0.28	0.03	0.01	0.00	0.00	0.00
PC 2	0.68	0.29	0.57	-0.35	-0.05	-0.01	0.00	0.00	0.00
PC 3	0.31	-0.94	0.02	-0.14	0.02	0.00	0.00	0.00	0.00
PC 4	0.10	-0.09	0.40	0.81	-0.40	0.04	0.03	0.01	-0.01
PC 5	0.03	-0.01	0.12	0.19	0.48	-0.71	0.46	0.04	-0.03
PC 6	0.03	-0.01	0.12	0.20	0.45	-0.16	-0.84	0.02	0.03
PC 7	0.03	0.00	0.11	0.16	0.48	0.48	0.21	-0.64	0.18
PC 8	0.02	0.00	0.08	0.10	0.36	0.43	0.14	0.51	-0.62
PC 9	0.01	0.00	0.04	0.05	0.18	0.22	0.11	0.57	0.76

Table 2 Percentage of information contained in each principal component.

Principal components	PC1	PC2	PC3	PC4	PC5	PC6	PC7	PC8	PC9
Variance in %	73.6	23.9	1.91	0.56	0.016	0.001	0.001	0.001	0.001

RGB colour composite PC1-2-3, PC1-2-4 and PC1-3-4 were prepared for interpretation of lithologies and geological structures. The RGB colour composite PC1-3-4 was found good for enhancing the rock units and structures in the study area so that it was further pan sharpened with hill-shade of ASTER DEM as shown in Figure 10. In the RGB colour composite PC1-3-4, tuff silt and clay appear as brown yellow, chert and clay appear as pink, vegetation as faded blue tint and volcanic rocks appear as green.

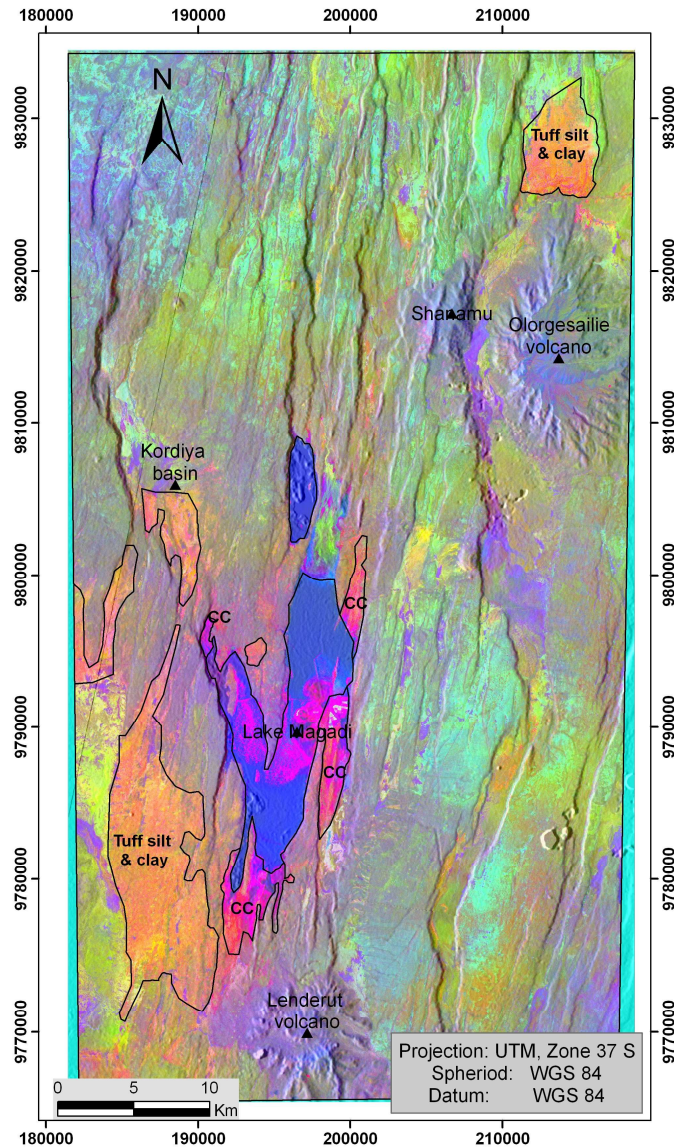


Figure 10 PC134 of ASTER image pan sharpened with hill shade of ASTER DEM, the identified units are labeled on the image, and CC represents Chert and clay.

Filtering techniques

Filtering is good for enhancing linear features from remote sensing datasets. Filtering can be performed through frequency domain or spatial domain (Bonham-Carter, 1994; Drury, 2001). Owing to their relative simplicity, spatial domain filtering operations are used by most image processing systems (Drury, 2001) to extract lineaments from remote sensing datasets.

Spatial domain filtering operations are classified as: low pass filters, which have smoothing effect; high pass filters (e.g. Laplacian), which have edge sharpening effect; and directional filters, which enhance linear features oriented in specific directions (Bonham-Carter, 1994; Drury, 2001). Sobel and Prewitt filters are examples of directional filters. The Sobel filter is more commonly used than Prewitt filter because the former has good performance and computational efficiency (Suzen and Toprak, 1998; Wang et al., 2004); thus, the Sobel filter was also used in this study.

The Sobel filter in ERDAS 9.2 has three different kernel sizes: 3x3, 5x5 and 7x7. After trying both options, the 5 x 5 kernel size sobel filter was found suitable for this study. Sobel filter simultaneously filters an image along the horizontal direction (Kx) and along the vertical direction (Ky). The matrixes of the 5x5 sobel filter along Kx and along Ky are shown in Table 3.

Table 3 Kernel sizes of the Sobel filter

a) Sobel kernel in the horizontal direction (Kx)

-1	-2	0	2	1
-2	-3	0	3	2
-3	-4	0	4	3
-2	-3	0	3	2
-1	-2	0	2	1

b) Sobel kernel in the vertical direction (Ky)

-1	-2	-3	-2	-1
-2	-3	-4	3	-2
0	0	0	0	0
2	3	4	3	2
1	2	3	2	1

According to Levin (1999), the result of Sobel filtered image (SFI) is calculated using the following equation:

$$SFI = \text{SQRT}(X^2 + Y^2) \dots\dots\dots \text{Equation 1}$$

Where SQRT stands for square root, X represents image filtered by Kx and Y represents image filtered by Ky.

The Sobel filters were applied to the single ASTER bands in the VNIR range and the SWIR range as well as to the principal component one (PC1). Visually, PC1 showed better spatial discrimination of structures and was selected for that for structural interpretation. The Sobel-enhanced image of PC1 had noisy appearance so that it was filtered with a 5x5 kernel low pass filter in order to reduce the noise. As shown in Figure 11 the structures, which are represented by white linear features, are enhanced in the Sobel filtered image of PC1.

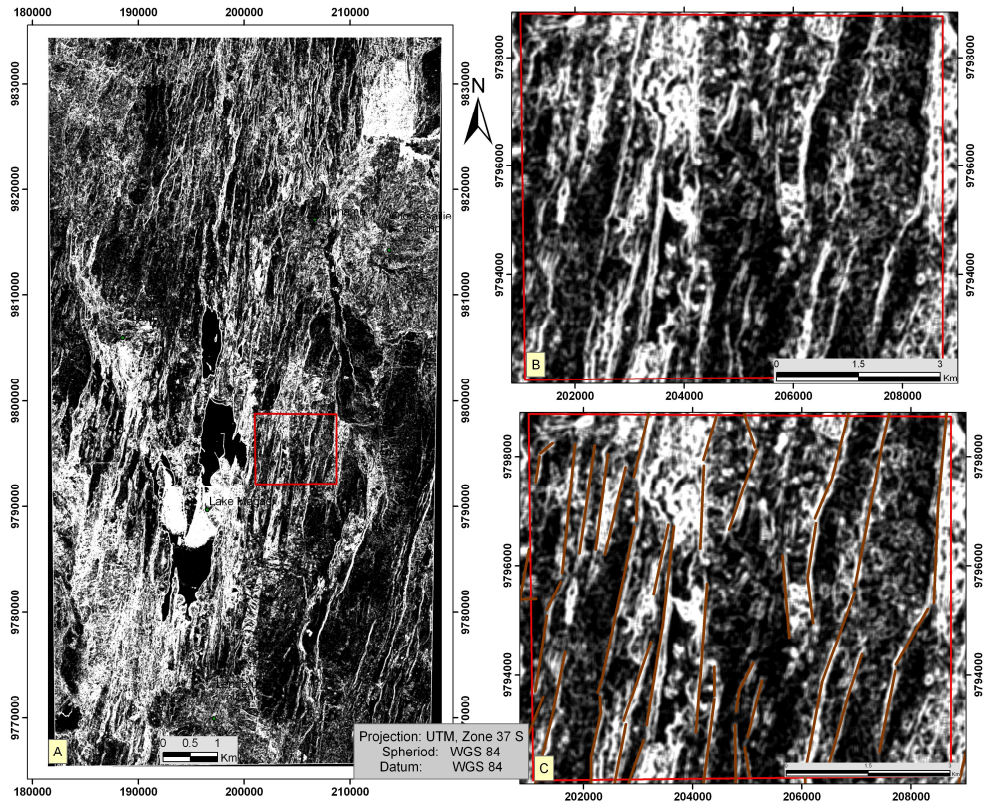


Figure 11 Sobel filtered image of PC1, the inset indicated with box in (A) is zoomed in (B) and the interpreted faults overlying the zoomed image are shown in (C).

3.2.2. Enhancement of SRTM DEM and ASTER DEM

Derivatives of a DEM have been demonstrated to be useful in enhancing structures (Ganas et al., 2005; Gloaguen et al., 2007; Jordan and Schott, 2005); thus, secondary products (slope map and shaded relief) were created from the SRTM DEM and ASTER DEM.

Shaded relief

In order to enhance faults with different orientations, hill-shading using sun elevation angle of 45° and illumination angles of 315° (NW), 0° (N), and 270° (W) were applied to the ASTER DEM and SRTM DEM. In addition, 3D DEM visualization was applied in ILWIS; the software enables to visualize 3D of the study area by hill-shading using sun elevation angle of 45° and three illumination angles 315° (NW), 00° (N) and 2700° (W). The 3D hill-shaded SRTM DEM and the interpreted faults are shown in Figure 12A and B, respectively. The different faults are clearly shown in the image and the 3D view enables to deduce the fault throw directions and to identify the horst and graben structures in the area. For clarity purpose only few horst and graben which are labeled on the image as H and G, respectively while the fault throw directions are not shown in this figure; they are shown in Figure 14.

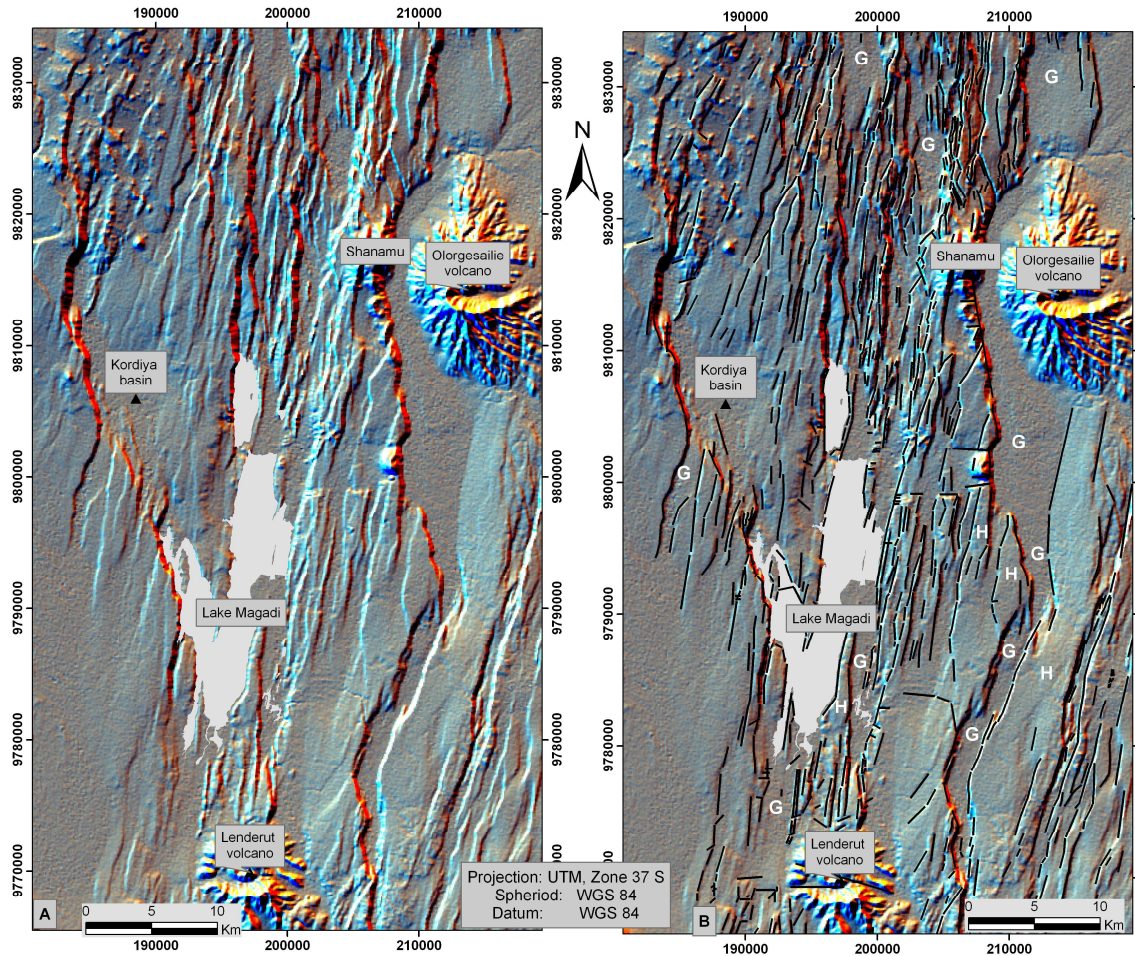


Figure 12 A) 3D SRTM DEM hill-shaded from three illumination angles 3150 (NW), 00 (N) and 2700 (W); B) interpreted faults, horst and graben overlain on the hill-shaded SRTM DEM image.

Slope map

Faults in a DEM are characterized by steep slopes, which makes slope and aspect information crucial in identifying faults from a DEM (Gloaguen et al., 2007). In the study area, steep faults are associated graben and horst structures. The presence of such steep faults in the area favors the use of a slope map for the interpretation of faults. A slope map of ASTER DEM and a slope map SRTM DEM were prepared and interpreted. Figure 13 shows (A) slope map from the ASTER DEM (the faults appear as bright lines) and (B) the interpreted faults represented in gray colour. In this slope map, the N-S structures are better enhanced owing to their steep slope.

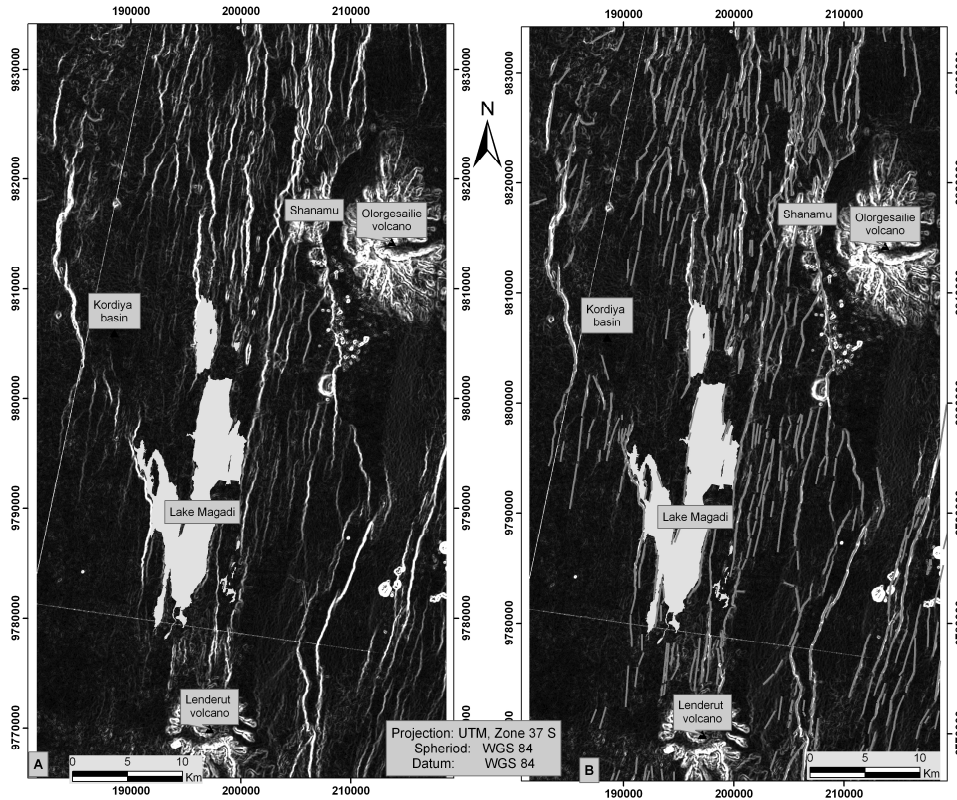


Figure 13 A) Slope map derived from ASTER DEM; B) interpreted faults (gray colour) overlain on the slope map.

3.3. Analysis on faults extracted from the remote sensing datasets

3.3.1. Map and orientation of the faults

After applying different enhancement techniques on the remote sensing datasets, the faults were interpreted visually and extracted manually; and the combined results (from ASTER images, ASTER DEM and SRTM DEM) are presented in Figure 14. Besides, rose diagram of the faults was prepared (Figure 15) in order to categorize orientations of the faults in the area in to sets. The rose diagram and the fault map show that there are more than one set of faults in the study area. The fault trends in the area are grouped in to two main sets: N-S and ENE-WSW.

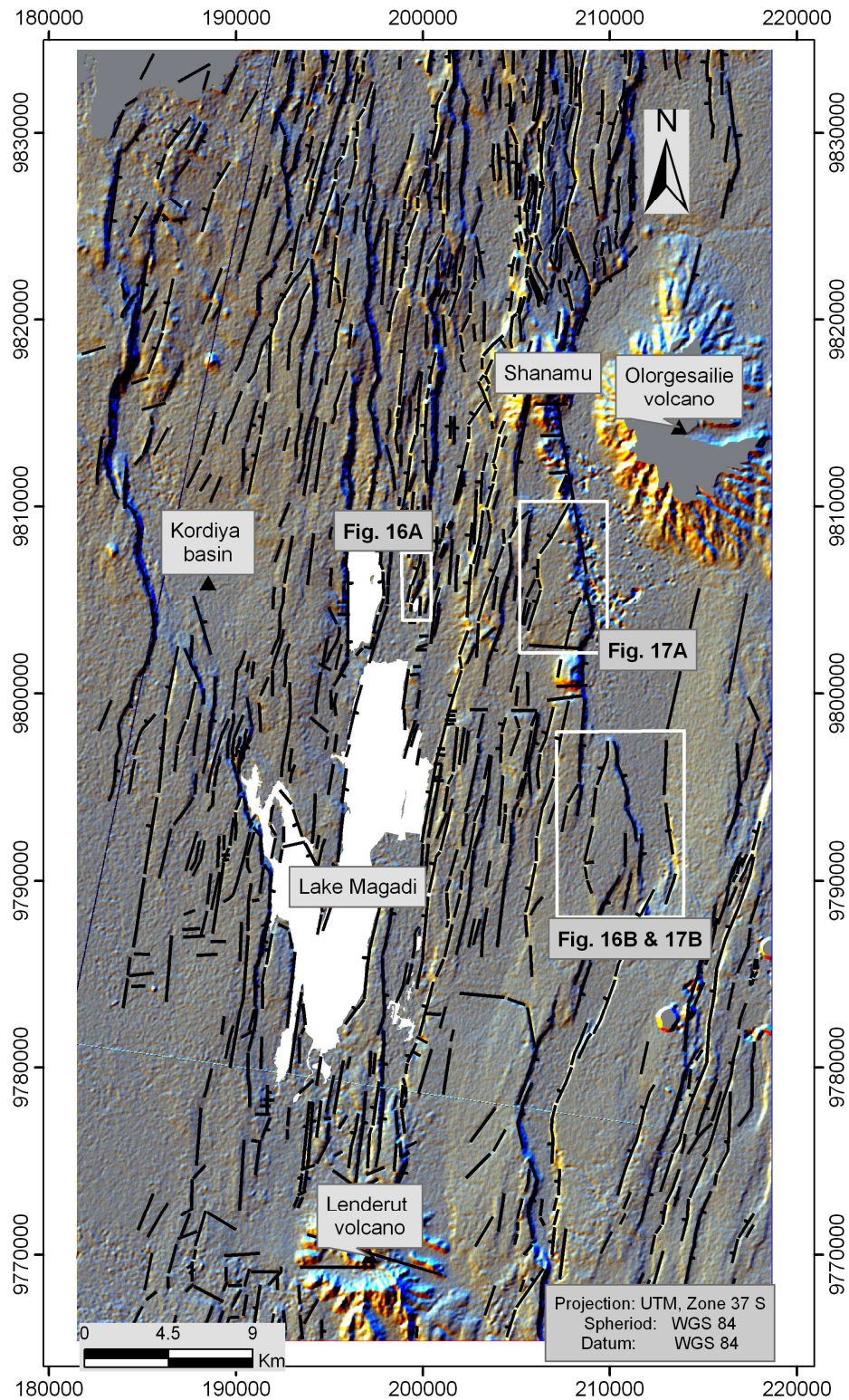


Figure 14 Faults (interpreted from all the datasets used) with their throw direction overlying the 3D illuminated ASTER DEM hill-shade.

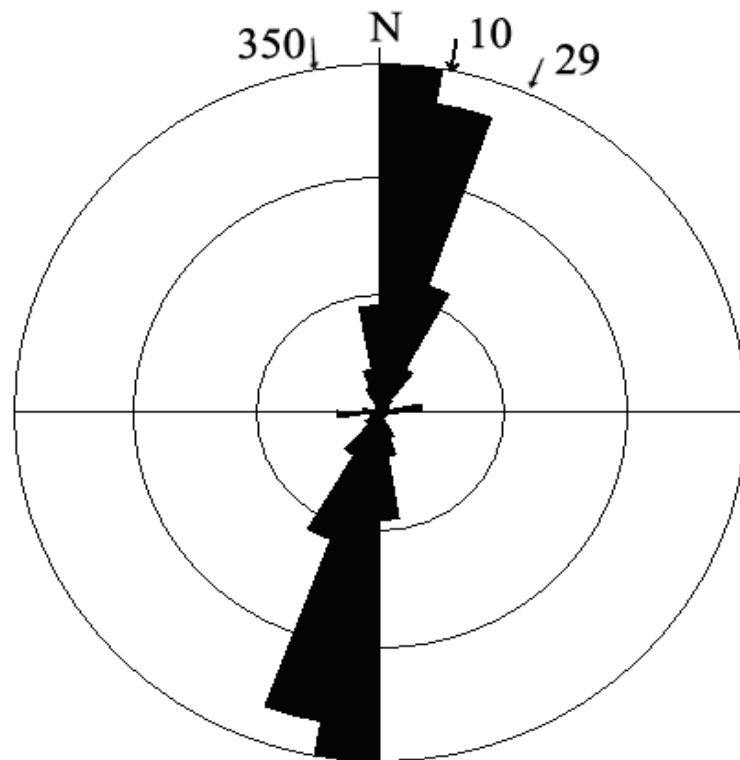


Figure 15 Rose diagram of the faults extracted from ASTER images, DEM and SRTM DEM. No. of Data = 1023, Mean Resultant strike = 011-191; the numbers are labelled as reference for estimating the strikes.

The N-S faults

This fault set encompasses a wide range of trends (N-S, NNW-SSE and NNE-SSW) and it is the most dominant structure in the study area forming horst and graben features which are associated with the formation of the rift under an E-W extension. Average strike of these faults is N10°E. The N-S trending faults are the most prominent set in the Kenya Rift that makes them easily recognizable from various remotely sensed data. They have been reported from the Kenya Rift (Atmaoui and Hollnack, 2003; Gloaguen et al., 2007; Hackman et al., 1990; Le Turdu et al., 1999).

The N-S faults deflect their orientation to NNW-SSE (N160-170°) and NNE-SSW (N15-30°) forming Z and S shaped fault patterns, respectively. Such Z and S fault patterns develop when the N-S faults intersect with pre-existing NW-SE and NE-SW structures (Jarrige et al., 1990; Le Turdu et al., 1999). Reactivation of the pre-existing structures has resulted in the formation of NW-SE and NE-SW trending faults that have been observed in the field and they are discussed in section 4.2.1.

a) The Z shape features

As shown in Figure 16 A and B, the Z shape features mark orientation change of the N-S faults to NNW-SSE. They have dextral sense of movement as indicated by the arrows in both figures. These types of fault patterns are associated with reactivation of NW-SE pre-existing structures and they have

been observed in central Kenya Rift and the Lake Magadi area by Le Turdu et al. (1999), see section 6.2 .

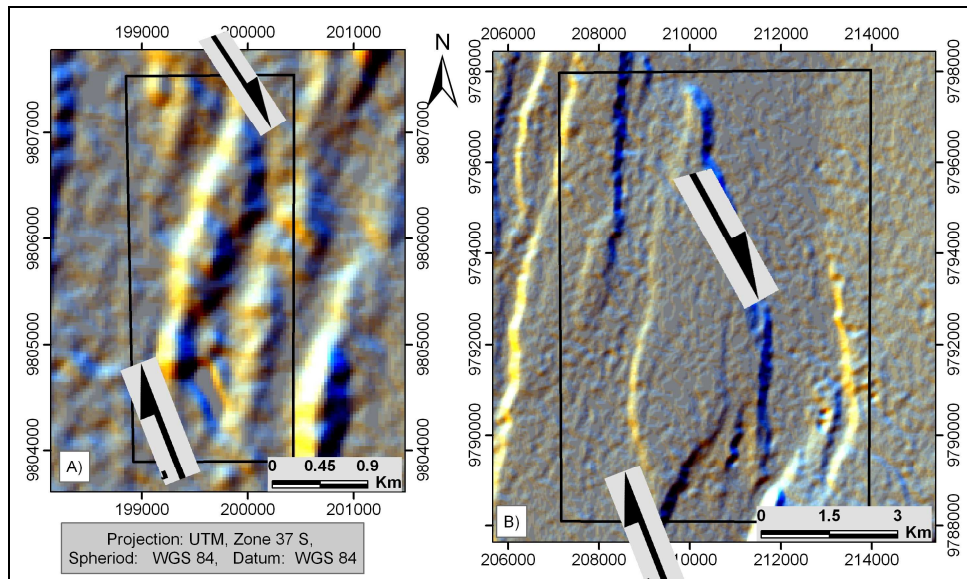


Figure 16 A) and B) Z shaped feature showing dextral movement along the NW-SE shear zone.

b) The S shape features

The S shape features show deflection of orientation from N-S to NNE-SSW with sinistral sense of movement as indicated with the arrows in

Figure 17 A and B. Besides, slickensides observed in the field indicated sinistral sense of movement (section 4.2.1). As discussed in section 6.2, the S shape fault patterns have been reported from the central Kenya Rift by Le Turdu et al. (1999) and they are associated with reactivation of NE-SW pre-existing structure; however, they have not been reported from the Lake Magadi area.

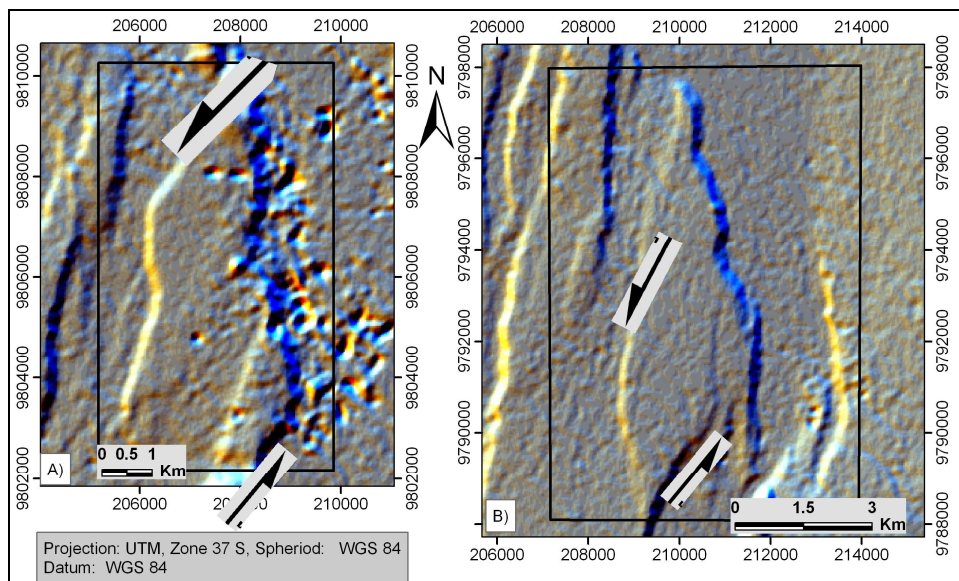


Figure 17 A) and B) S shaped feature showing sinistral sense of movement along the NE-SW shear zone.

The ENE-WSW fault set

The ENE-WSW faults are sparsely distributed in central part of the study area. In the field, slicken-side with strike slip movement was observed on this fault (section 4.2.1). Such ENE-WSW structure has been reported from the Turkana area in northern Kenya Rift (Hackman et al., 1990; Vétel et al., 2003); an E-W volcanic mountains alignment (Monduli, Meru and Kilimanjaro) also exist in northern Tanzania Rift (Le Gall et al., 2008). Thus, the ENE-WSW fault set in the study area is related to regional structures that have active role in geo-tectonics of the rift.

3.3.2. Fractal analysis

Fault dimensions such as length and displacement are useful for understanding evolution of fault system. Plots of certain quantitative properties of faults (eg., length, displacement, etc) and frequencies or numbers of fault plot in a log- log graph can be characterized by a power-law relationships, which can be generally expressed as (Gloaguen et al., 2007; Marrett and Allmendinger, 1992; Needham et al., 1996; Walsh et al., 2003; Yielding et al., 1996).

$$N = gL^{-D} \dots\dots\dots \text{Equation 2}$$

Where N is the number of faults with characteristics L (e.g., length, displacement, etc.), g is the constant or proportionality between N and L, and D is the scaling component or fractal dimension of the distribution of N with respect to L.

The value of D is an indicator of the contribution of small size (cm to mm size) faults to tectonic extension in a given area (Marrett and Allmendinger, 1992; Walsh and Watterson, 1992; Yielding et al., 1996). A value of D less than one implies that the contribution of small size faults to extension is negligible, whereas value of D equal to or greater than one implies that the contribution of small size faults is higher than that of large faults (Marrett and Allmendinger, 1992).

Faults interpreted from remote sensing datasets approximate real world faults so that fractal analysis (eg. length versus frequency on logarithmic scale) can be done on their displacement and length. Then, fractal dimension (D) of the study area can be determined using Equation 2.

In this research, fractal analysis was applied on fault length and fault displacement in order to understand tectonic significance of the interpreted faults.

Fault length

Length versus frequency of the faults extracted from ASTER image, ASTER DEM and SRTM DEM were plotted on histogram as well as on logarithmic scale.

As shown in the histogram plot of the fault length versus frequency (Figure 18), the dominant faults in the area range from 0.7km to about 2.5km long. The average length of the extracted faults is 1.61km.

The log-log plot of fault length versus fault frequency (Figure 19) in the length range of 1.6 km to 10 km can be fitted with a straight line, which implies that, in the study area the frequency distribution of faults with lengths greater than 1.6 km has a fractal behaviour. However, the frequency distribution of faults shorter than 1.6 km do not seem to have a fractal behaviour, although the results could be attributed to under-sampling effects (Walsh et al., 2003). However, in this research higher resolution datasets (ASTER DEM and ASTER image) that could reveal small details were used so that under-sampling is possibly not a reason for the non-fractal behaviour of the frequency distribution of faults shorter than 1.6 km. Rather, it is likely that short faults merged or connected with each other to form longer faults during growth of the rift. Thus, a power function was fitted to the linear portion of the plot giving a fractal dimension D value of 3 with R^2 equal to 0.93; the fitted function is indicated by the solid line in the figure. The large value of D (i.e. greater than 1) implies that short faults (<1.6 km), compared to longer faults (>1.6 km), possibly have higher contribution to extensional tectonics of the rift in the study area. This implication was verified in the field by the observations of minor scale faults and the recent rupture, which are good examples active tectonics in the area.

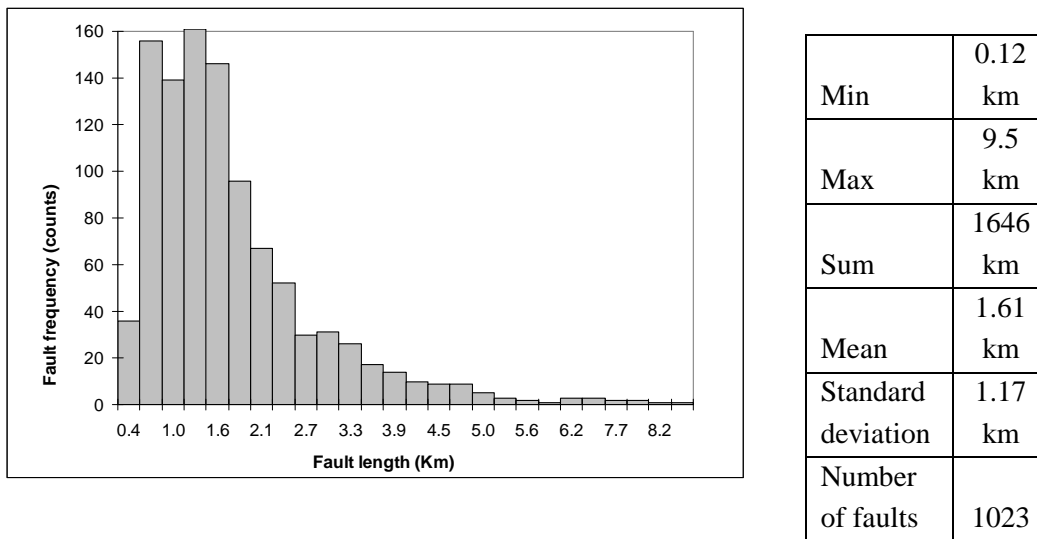


Figure 18 Length versus class frequency of faults of the combined result (from the ASTER images, ASTER DEM and SRTM DEM).

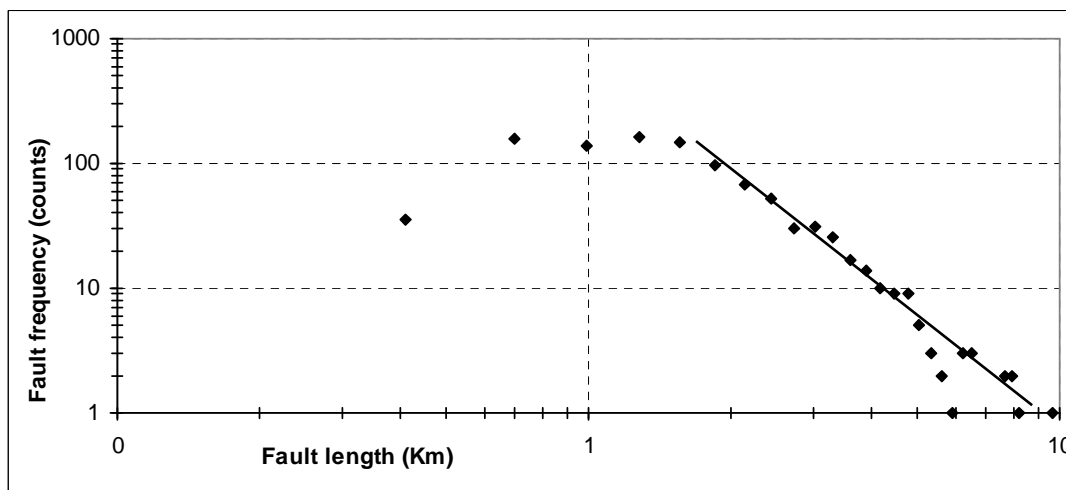


Figure 19 Logarithmic plot of fault length versus frequency and the fitted line

Fault throw

Six topographic profiles about 10km apart from each other were drawn on the ASTER DEM (Figure 20) that run from west to east perpendicular to strike of the dominant fault set. Topographic section along profile 2 is shown in Figure 21 as an example; topographic sections of all the profiles are put in the Appendix (see Figure 49 and Figure 50). In the produced sections, the horsts and graben in the rift are clearly shown where the grabens are labeled as G in the all the sections. Fault throws were estimated from the faults intersecting the topographic sections and the data of amounts of fault throw and frequency were plotted on a histogram and on log-log graph.

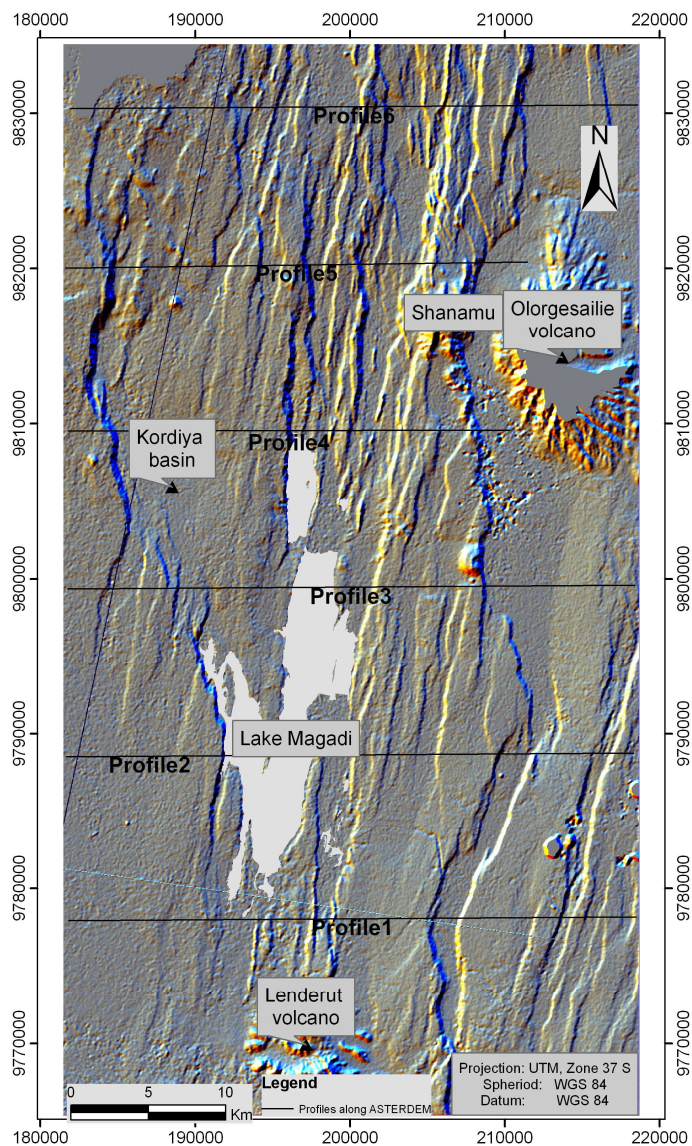


Figure 20 Locations of the six topographic profiles on the ASTER DEM underlain by hill-shade of ASTERDEM.

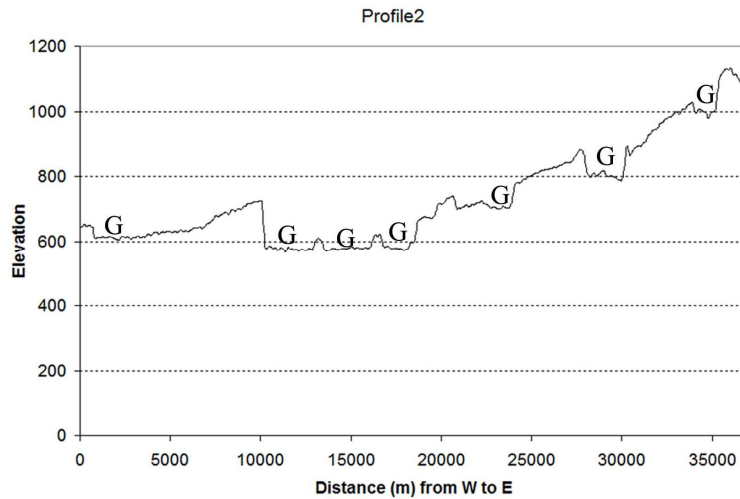
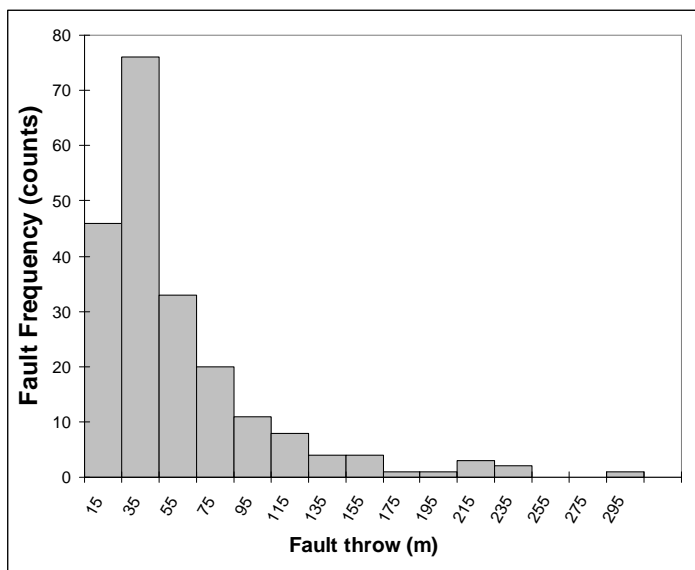


Figure 21 Topographic section (distance versus elevation) along profiles 2 derived from the ASTER DEM. The section runs from west on the left to east on the right, G represents graben.

The histogram of the fault throws (Figure 22) shows that the dominant amounts of throw ranges from 15-75m, with an average throw of 46m and the most frequent throw is 35m while the largest throw along the profiles reaches 295m. However, estimates of displacements considered to be conservative because erosion has already removed the upper parts of the faults and that sediments have been deposited in the grabens there by covering the lower limit of the faults in the study area.

The Log-Log graph of the fault throws versus fault frequency (Figure 23) has a linear component except in the small displacement range of less than 30 m, which could be due to under-sampling because the spatial resolution of the data set used were not favourable in estimating smaller throws. Hence, a power function was fitted to the linear pattern of the plot as indicated by the solid line in the figure and the fractal dimension derived was 2.2 with R^2 equal to 0.91. The high value of D implies that small fault throws (i.e., <30 m) in the area have significant contribution to tectonics of the rift.



Min	7m
Max	294m
Count	210
Mean	46m
Standard deviation	46

Figure 22 Fault throw (from six profiles along ASTER DEM) versus frequency

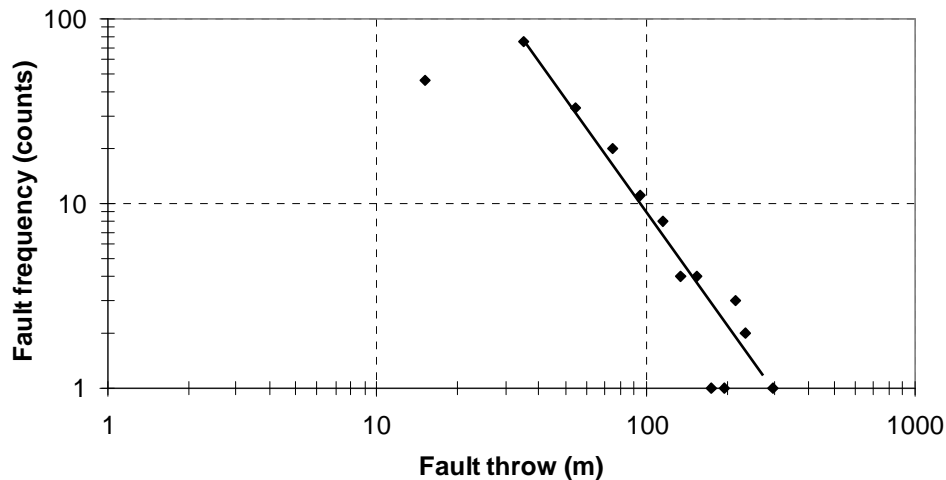


Figure 23 Logarithmic plot of fault throw (from six profiles along ASTER DEM) versus frequency and the fitted line

3.4. Discussion

In this chapter lithologic and structural information has been extracted from the remote sensing datasets after applying different enhancement methods.

In order to extract optimum lithologic information, colour composites of: the ASTER image bands, the principal components and the band ratios were used. By combining results of the different enhancement methods, the sediments in the study area were discriminated from each other and from the volcanic rocks. The discriminated sediments include chert and clay and tuff silt and clay. Thus, lithologic boundary of these units obtained from the ASTER images can be used for updating the existing old geological map of the study area by Baker, (1958) which was prepared through reconnaissance survey. However, the ASTER image did not help in discriminating the volcanic rocks so that band ratio (11*11)/ (10/12) was used as a general indicator of silica content of the volcanic rocks in the study area. The silica content image showed that rocks in central part of the study area are rich in silica while the rocks in the flanks of the rift and in some horsts at the central part have low silica content. Hence, airborne magnetic data was used to further classify the volcanic units (section 5.1.1).

Structural information was extracted from the ASTER image, ASTER DEM and SRTM DEM. The faults extracted from all the datasets were combined and rose diagram of the faults gave two main trends: N-S and ENE-WSW. The N-S faults are the most dominant structures in the area. They show deflections to NNW-SSE and NNE-SSW forming Z and S shaped fault patterns, respectively. The Z

and S fault patterns develop when the N-S faults intersect with pre-existing NW-SE and NE-SW structures. Reactivation of the pre-existing structures has resulted in the formation of NW-SE and NE-SW faults in the study area which have been observed in the field (section 4.2.1). Both fault patterns have been reported from the central Kenya Rift; while previous works on the Lake Magadi area have reported only Z patterns. However, this research has found an S shape pattern on remote sensing data and its corresponding sinistral fault was observed in the field (section 4.2.1).

Therefore, the over all structures deduced from the remote sensing data are the two main trends (N-S and ENE-WSW) visible in the rose diagram and the reactivated dextral NW-SE and sinistral NE-SW structures which were observed in the field and are represented in the remote sensing data sets with Z and S shapes, respectively.

On the other hand, fractal analysis was done on length of the extracted faults and on fault throw of faults intersecting six profiles. The fractal dimension D obtained from the throw and length are 2 and 3, respectively. These large D values signify that short faults (<1.6 km) and faults with small throws (<30m) possibly have higher contribution to extensional tectonics of the rift in the study area. This implication was verified in the field by the observations of minor scale faults and the recent rupture, which are good examples active tectonics in the area.

4. Field data collection and analysis

Field investigation was conducted in the study area in September 15 - 30, 2008. In addition to the magnetic and resistivity surveys, structural and lithologic field data were collected (Figure 24). Structural data were taken on minor scale faults because the large scale and steep faults were inaccessible. The structural data collected consists of strike and dip of faults as well as trend and plunge of slickensides when ever and where ever those are found.

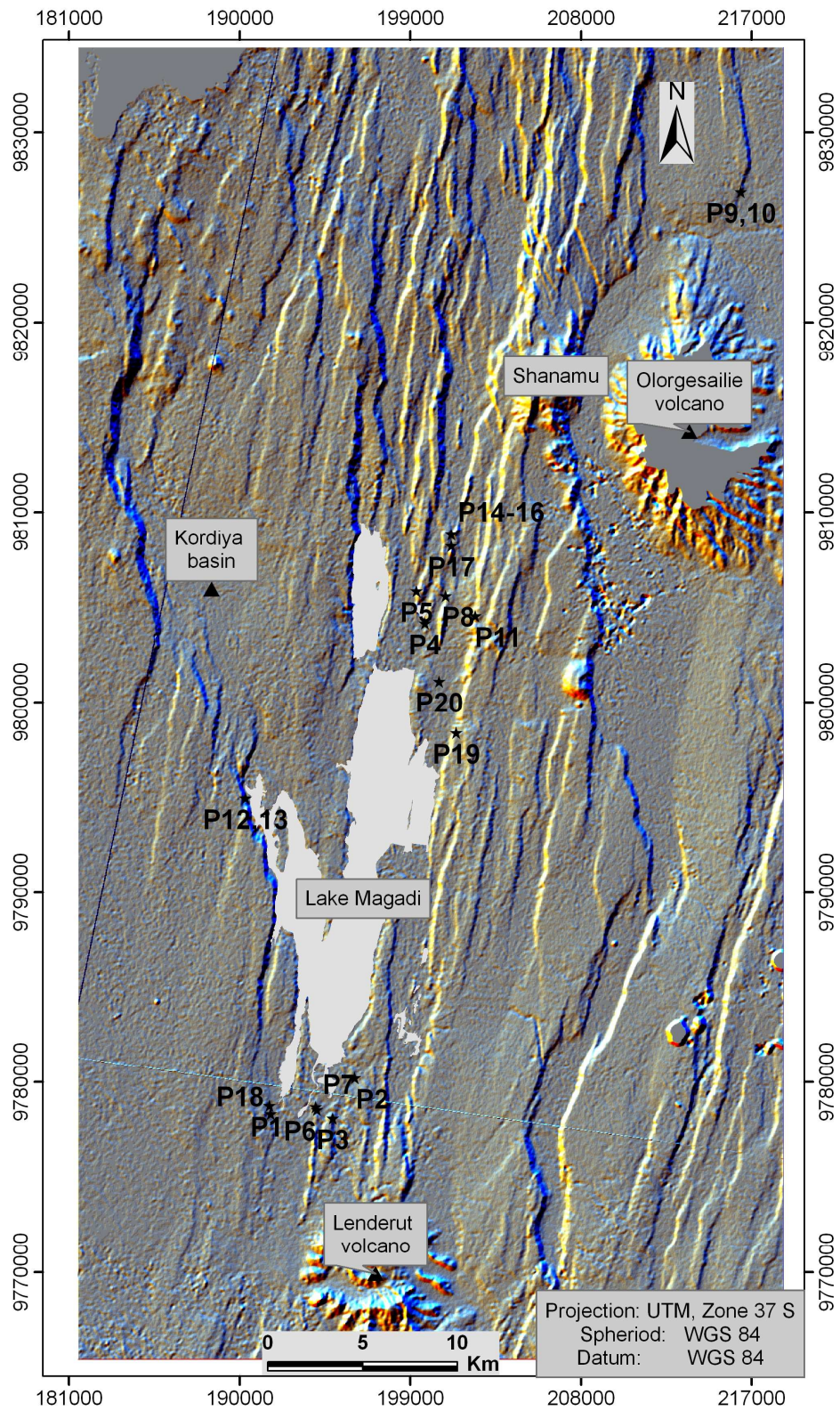


Figure 24 locations of photos taken in the field, P stands for photo.

4.1. Rocks

The lithologies observed in the field consist of volcanic rocks that occur in the horst and sediments that fill the graben. The volcanic rocks which cover most part of the study area are fine-grained with abundant felsic minerals and mafic minerals that give it intermediate colour. Thin section and chemical analysis by Baker (1958) showed that the volcanic rocks are trachytes; however, mafic volcanic rock was also observed in north eastern part of the study area. On the other hand, the sediments include fluvial to lake deposits (silt clay and chert). The clay and chert occur together and in some places as intercalations (Photo 1). The silt clay unit in the area has variable colour ranging from white, green to yellow (Photo 2) suggesting variation in chemical composition or source parent material.



Photo 1 Laminated clay overlain by chert.

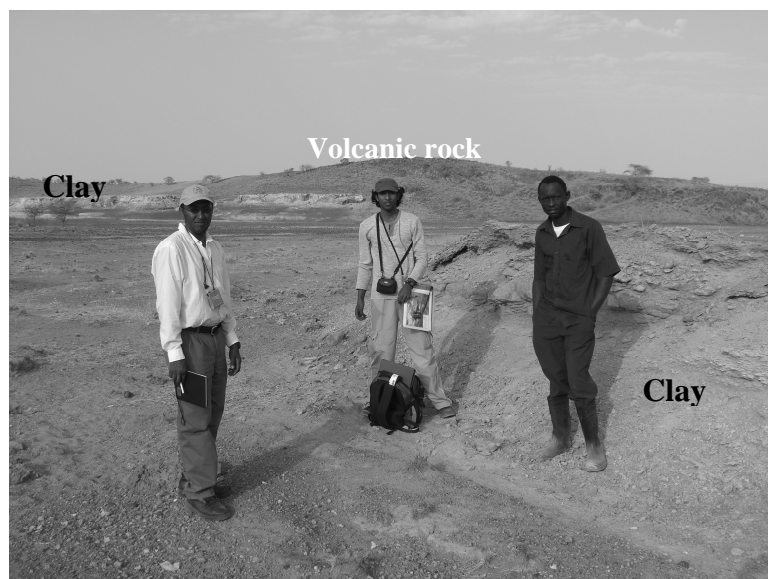


Photo 2 taken looking SW; green and white silt clay deposit in a small graben.

4.2. Faults and other structures

The structural data collected from minor-scale faults were analyzed using rose diagram in order to group them into set of certain trends and then explain tectonic significance of each set as well as reconstructing paleostress from the faults and slickensides in order to understand extension history of the study area.

4.2.1. The different sets of structures

Rose diagram is good means of representing strike of faults so that sets having similar strikes are grouped together. As shown in Figure 25 , the faults observed in the field are trending into N-S, NW-SE, ENE-WSW and NE-SW directions. The N-S and ENE-WSW structures are in general agreement with the two main trends in the remote sensing results (section 3.3.1). The NW-SE and NE-SW faults observed in the field are reactivation of pre-existing structures and which are represented with Z and S fault patterns in the remote sensing data, respectively as discussed in section 3.3.1.

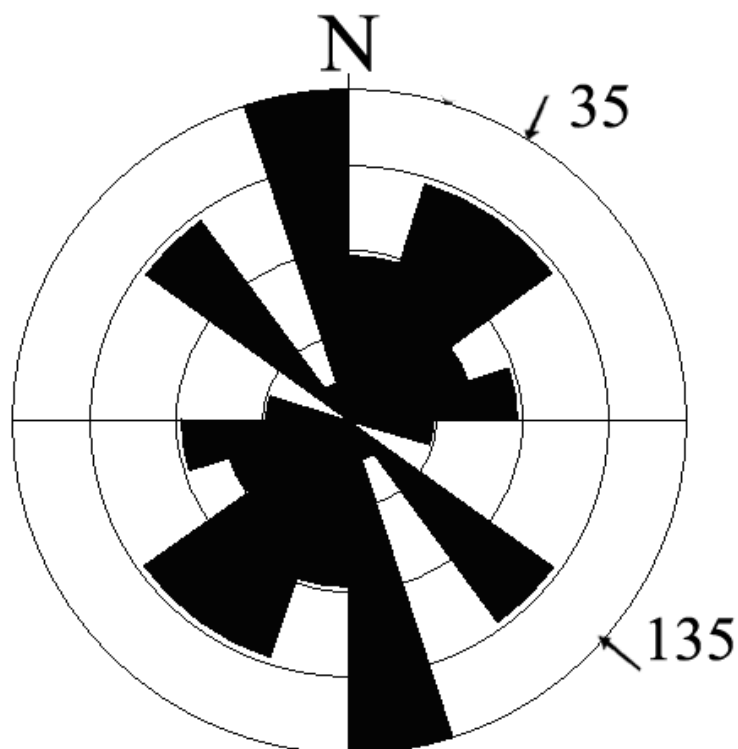


Figure 25 Rose diagram showing strike of different fault sets collected from the field, number of data is 41. The numbers are labeled as reference for estimating the strikes.

The N-S fault sets

This fault set includes N-S, NNE-SSW and NNW-SSE trending faults with an average strike of N100E. As mentioned in section 3.3.1, these faults are the most prominent and dominant set in the Kenya Rift. In the field this fault set was seen to be cut by all set of faults making them the oldest fault set in the area. As shown in photos 3, 4 and 5, they form steep escarpments and extend for long distance. These steep faults are the result of normal faulting which is manifested in the horst and graben structures in particular and rifting in general that has been created in the area.



Photo 3 N10°E fault, photo taken looking SW.



Photo 4 N10°E fault escarpment, photo taken looking NE

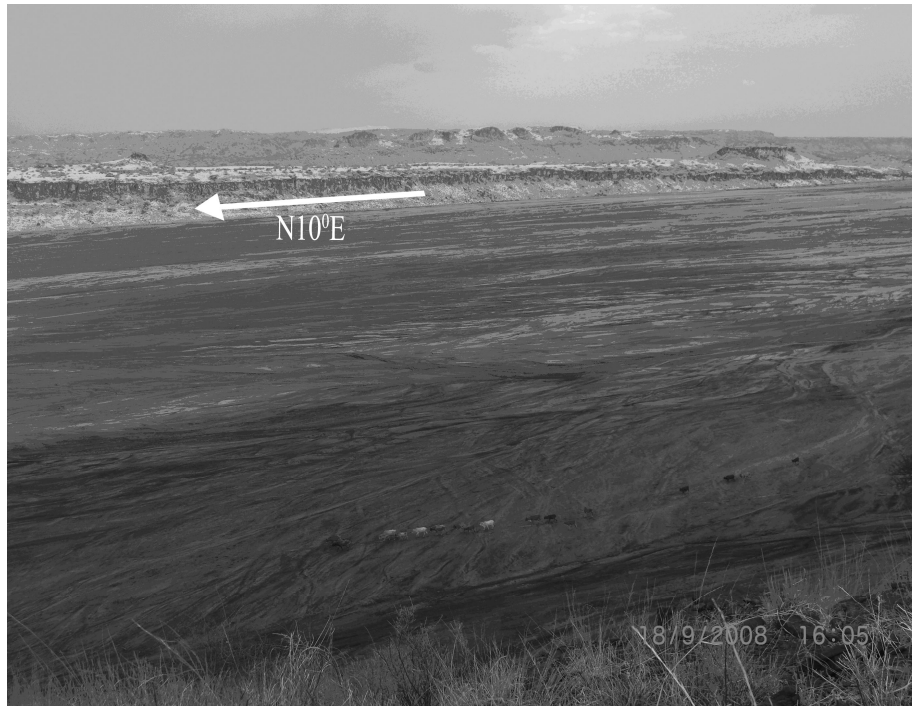


Photo 5 Photo taken looking ESE showing N10⁰E fault escarpment and west of the fault is a graben filled with sediments.

The NW-SE structure

This set has average strike of N140⁰E and it was observed in the field to cross-cut the N-S faults in the southern (Photo 6) and in the northern part of the Lake Magadi area. They have dextral sense of movement which is marked with Z-shaped fault patterns in the remote sensing datasets (section 3.3.1). The NW-SE faults are reactivation of pre-existing shear zone and has been reported in the Lake Magadi area (Atmaoui and Hollnack, 2003; Le Turdu et al., 1999), in central Kenya Rift (Le Turdu et al., 1999; Vétel et al., 2005) and in northern Tanzania Rift (Le Gall et al., 2008) and in the Gulf of Suez and northern Red Sea (Jarrige et al., 1990). Their occurrence in different parts of the EARS and the Red Sea region shows that they are regionally prevalent structures.



Photo 6 N140⁰E trending breccia of quartz vein cutting the N-S fault, photo taken looking SE

The ENE-WSW set

The ENE-WSW set includes trends ranging from N610 E to N1000E. This set includes faults (Photo 9 and Photo 10), quartz veins (Photo 7) and dykes (Photo 8). The ENE-WSW set cross-cuts the dominant N-S faults (Photo 7) and the ENE-WSW set itself is cut by the NE-SW fault set (Photo 20). As shown in Photo 9, the ENE-WSW set has horizontal slickensides which indicate an E-W strike slip movement; however, sense of slip movement indicators were not observed on this fault set.

Such ENE-WSW structure has been reported from the Turkana area in northern Kenya Rift (Hackman et al., 1990; Vétel et al., 2003); an E-W volcanic mountains alignment (Monduli, Meru and Kilimanjaro) also exist in northern Tanzania Rift (Le Gall et al., 2008). Besides, Jarrige et al.(1990) reported E-W structures in the Gulf of Suez and northern Red Sea. Thus, the ENE-WSW fault set in the study area is related to regional structures that have active role in geo-tectonics of the rift.

Atmaoui and Hollnack (2003) have reported the ENE-WSW fault set from the Lake Magdi area; however, they did not report slickensides from this set and neither did they explain tectonic significance of the fault set.



Photo 7 taken plan view where head of the hammer points south; an EW quartz vein cutting the N-S vein



Photo 8 a mafic dyke oriented $N90^{\circ}/45^{\circ} N$ cross cutting the clay on the right and weathered trachyte on the left, photo taken looking east.



Photo 9 taken looking NNE, fault plane $N104^{\circ}E/72^{\circ}$ SSW with horizontal slickensides.

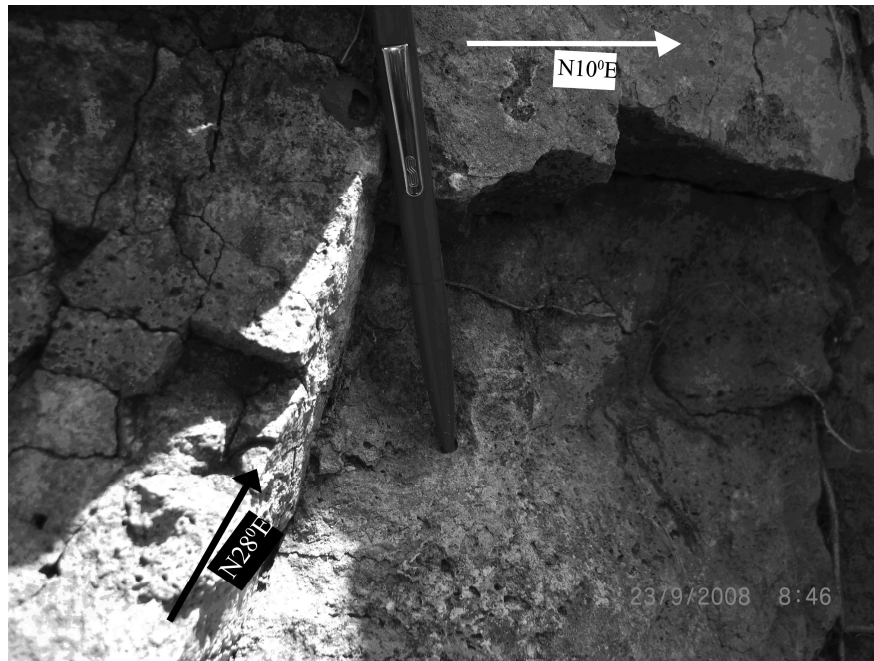


Photo 10 taken looking $N28^{\circ}E$, the fault plane oriented $N104^{\circ}E/72^{\circ}$ SSW is cut by the $N28^{\circ}E$ fault.

The NE-SW fault set

The NE-SW fault set has strikes that range from N28⁰E to N60⁰E with an average of N44⁰E so that strike of the set is taken as NE-SW. The NE-SW fault set was observed to cut all set of faults and rock types in the area (Photo 11, Photo 12, Photo 15, Photo 18, Photo 19 and Photo 20) which makes it the youngest fault set in the area. Slickensides with a plunge of 45 to 48 were observed in the field (Photo 13 and Photo 16) that enables to categorize the NE-SW set as oblique slip type of fault with a sinistral sense of movement as shown in Photo 15. This sinistral fault set is marked with S-shaped fault patterns in the remote sensing datasets (section 3.3.1).

Such oblique fault striking NE-SW has not been reported from the Lake Magadi area. However, it has been reported from other parts of the rift system. For example, a sinistral fault set striking N30⁰ to N60⁰ exists in the central and Northern Kenya Rift (Hackman et al., 1990; Le Turdu et al., 1999; Vétel et al., 2005), in northern Tanzania Rift (Le Gall et al., 2008), in the Ethiopian Rift (Kurz et al., 2007) and in the Gulf of Suez and northern Red Sea Jarrige et al.(1990) which was interpreted to have exploited pre-existing structures; besides, a NE-SW to ENE-WSW transform fault model has been postulated for the East African Rift System by Katz (1987). Therefore, this fault set is widely perceived and significant in geo-tectonics of the rift.

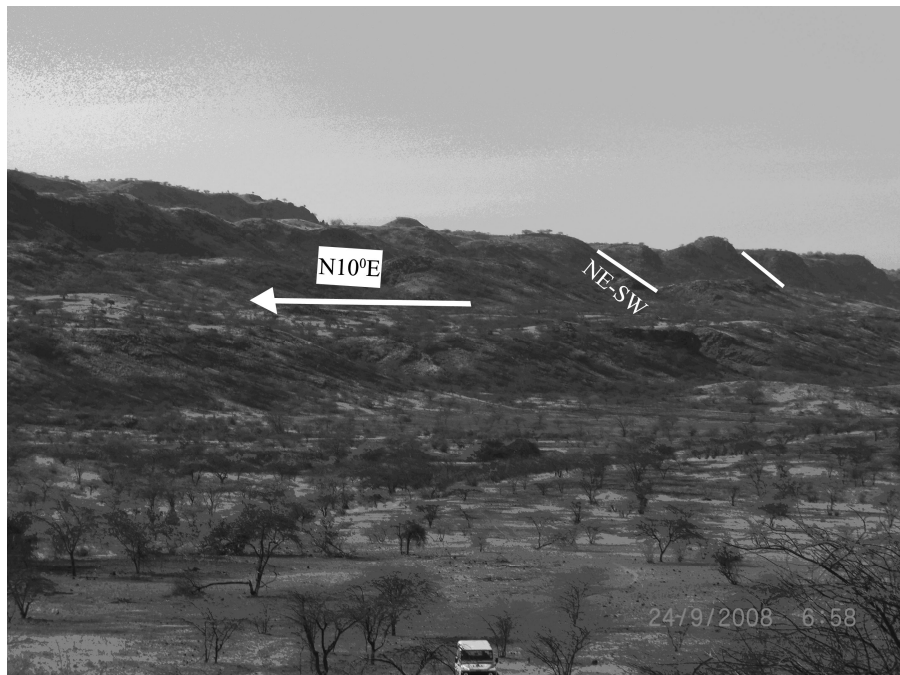


Photo 11 taken looking SE, breaks in the hill due to the NE-SW fault sets cutting the N-S fault set.

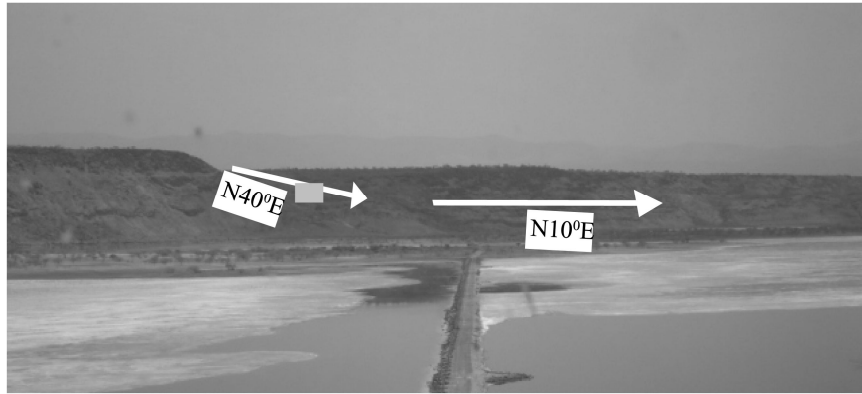


Photo 12 a $N40^{\circ}E/78$ SE fault cutting the $N10^{\circ}E$ fault, it was taken looking NW. The gray box represents a place where slicken sides was observed as shown in Photo 13.

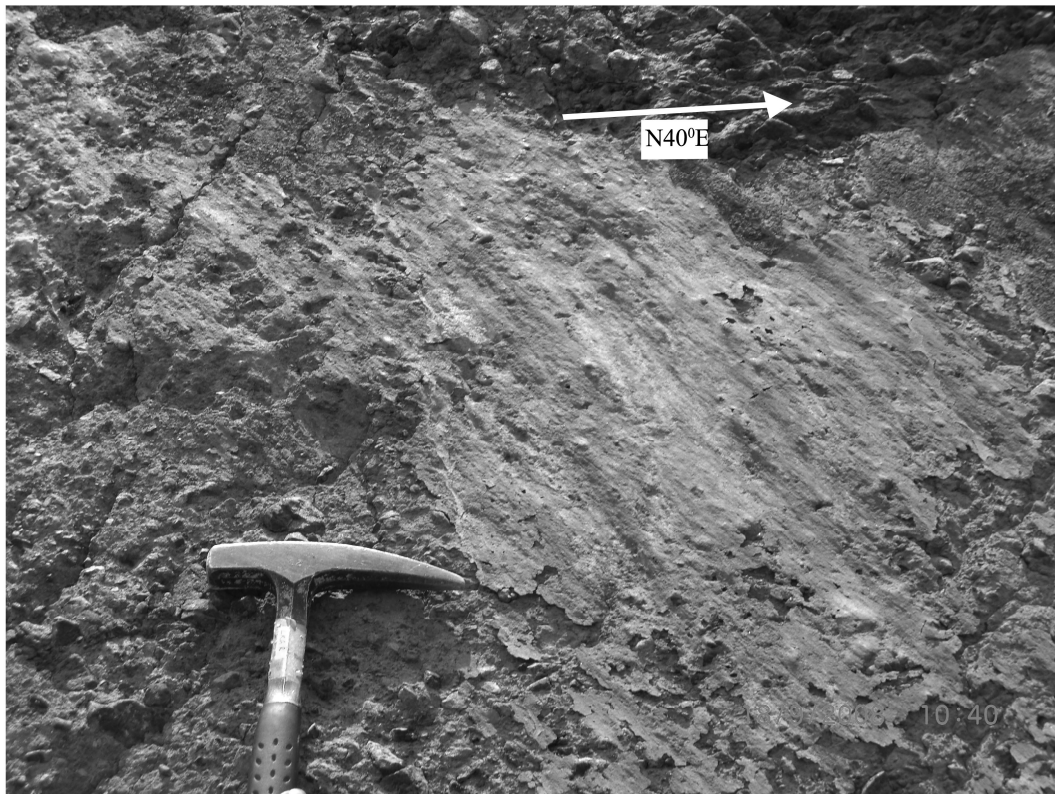


Photo 13 taken looking NW, showing slicken sides $[040^{\circ}/48]$ on the $N40^{\circ}E/78^{\circ}$ SE fault plane.



Photo 14 taken looking SW showing N10⁰E fault, the white box represents a place where the cross cutting relation of the two set of faults was observed (see Photo 15).



Photo 15 taken looking NW, plane N44⁰E/86 SE with slickensides (zoomed in Photo 16) cuts the N10⁰E fault. The sinistral sense of movement is indicated with black half arrow.



Photo 16 taken looking NW, closer view of the slicken sides 044⁰/45 in photo 15

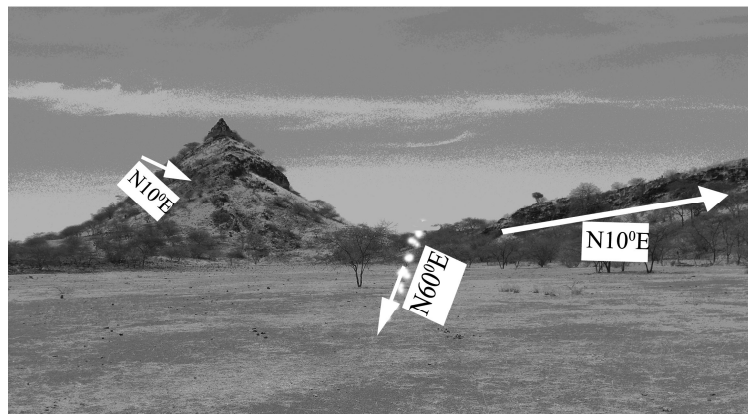


Photo 17 taken looking SW, it shows the sinistral movement along the N60⁰E fault.



Photo 18 head of the hammer points NE; photo showing a sinistral N60⁰E fault (with filling) cutting the N-S (N350⁰E) fault.

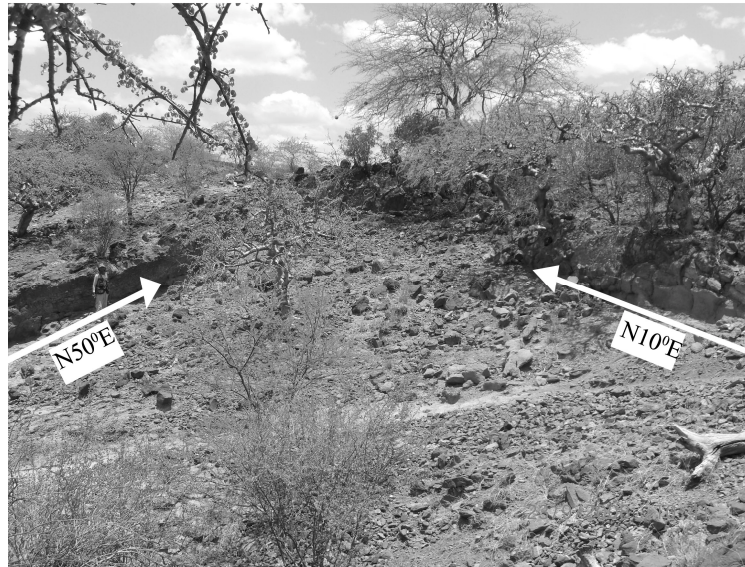


Photo 19 taken looking NE, it shows two set of faults: $N50^{\circ}E/45^{\circ}NW$ (left) cross cutting the $N10^{\circ}E/70^{\circ}E$ (right). Baking effect was observed in the clay (yellow in colour) contact with fault implying that the $N50^{\circ}E$ fault set is younger than the clay rock.

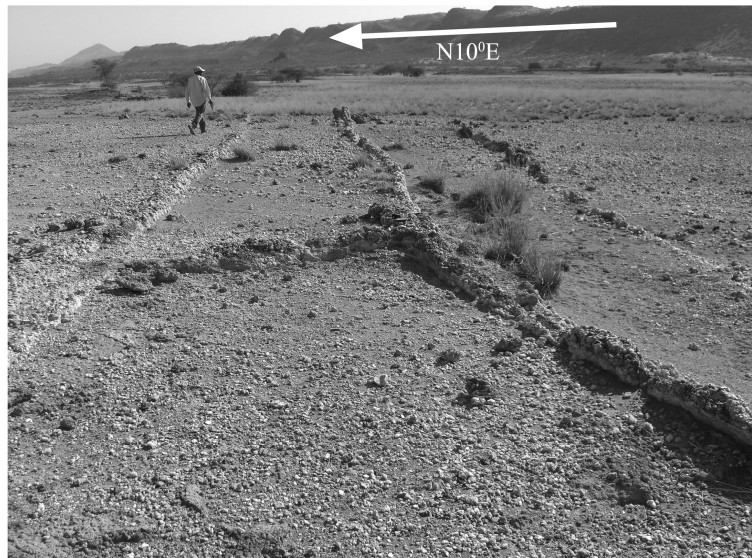


Photo 20 the $N28^{\circ}E$ structure cutting the $N100^{\circ}E$ structure, photo taken looking NE. The $N10^{\circ}E$ fault set is indicated with the white arrow.

4.2.2. Tectonic significance the different fault sets

The existence of four set of faults (oldest normal N-S faults, dextral NW-SE, strike slip ENE-WSW and youngest sinistral NE-SW) having different styles and different relative ages signify that there has been geodynamic change in tectonics of the rift that could have resulted in the formation of the four fault sets. This tectonic phenomena is explained by Anderson's theory of faulting (Anderson, 1951).

Anderson's theory states that orientation of the principal stresses: maximum (σ_1), intermediate (σ_2) and minimum (σ_3) relative to the earth's surface determines the type of faults that can be created; a

normal fault is formed when σ_1 acts vertically on top of the earth's surface while strike slip faults are formed when the σ_1 and σ_3 are oriented horizontal to the earth's surface (Figure 26 a and b).

Applying Anderson's theory to the study area, the extension direction is deduced. Finding an old normal fault in the study area implies that at its early stage the rift experienced normal faulting with σ_1 acting vertically on top of the earth's surface and σ_3 acting horizontally along E-W (Figure 26 a) that resulted an E-W extension. Then as a result of geo-tectonic change in the rift, σ_1 changed orientation from acting vertically on top to acting horizontally along N-S while σ_3 remained E-W (Figure 26 b) which means an E-W extension was maintained. The geo-tectonic change reactivated the pre-existing structures in the rift creating dextral NW-SE, strike slip ENE-WSW and sinistral NE-SW faults.

Therefore, to accommodate the geo-tectonic changes it faced during its life span, the rift has changed its strike and style while maintaining an E-W extension direction. The E-W extension explains the N-S normal faulting, the dextral NW-SE fault, the strike slip ENE-WSW fault and the sinistral NE-SW oblique fault movement in the area. In order to verify the extension direction in the study area, preliminary paleostress analysis has been done and it is discussed in the next section.

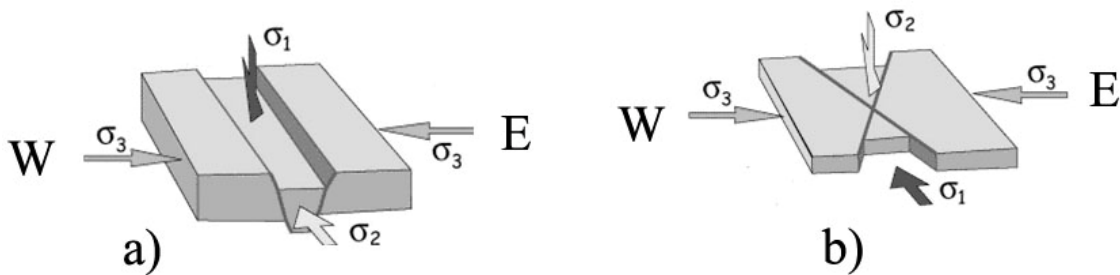


Figure 26 Anderson's fault model a) Normal fault where σ_1 acts vertically on top of the earth's surface and σ_3 acts along E-W, b) σ_1 acts along N-S while σ_3 remained E-W.

4.2.3. Paleostress analysis

Paleostress analysis is relevant to faults that have slickensides or to fracture without slip lines (Angelier, 1994; Delvaux and Sperner, 2003). In this research, paleostress analysis was accomplished using window version of Win-Tensor program following the procedures explained in Delvaux and Sperner (2003).

Win-Tensor is a paleostress analysis program developed by Dr. Damien Delvaux of the Royal Museum for Central Africa, Tervuren, Belgium. The program has two options: Right Dihedron Method, which is an interactive approach, and Rotation Optimization Method that accounts for angular deviations between the observed slip lines and the modelled shear on each plane.

Using both methods, the state of paleostress of the study area was reconstructed from the faults collected in the field. The results of the Dihedron Method (Figure 27) and the Rotation Optimization Method (Figure 28) show that trend of the minimum compression is 880 which indicates an E-W extension direction.

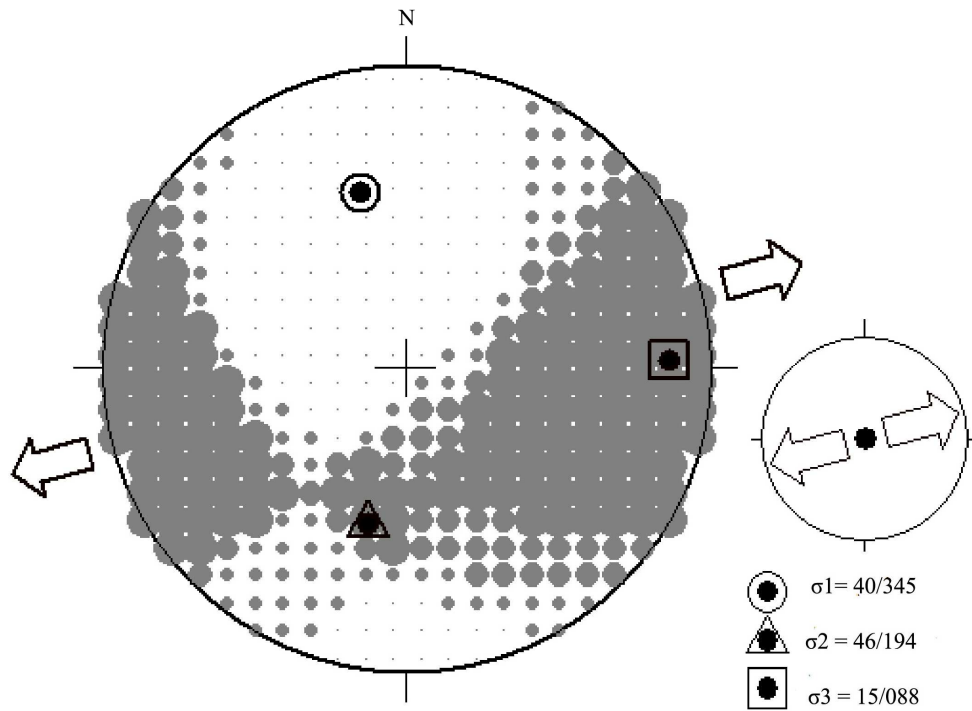


Figure 27 Lower hemisphere Schmidt stereo-plot showing paleostress analysis result of fault planes and slickensides using Right Dihedron Method; σ_1 , σ_2 and σ_3 are maximum, intermediate and minimum principal stresses, respectively.

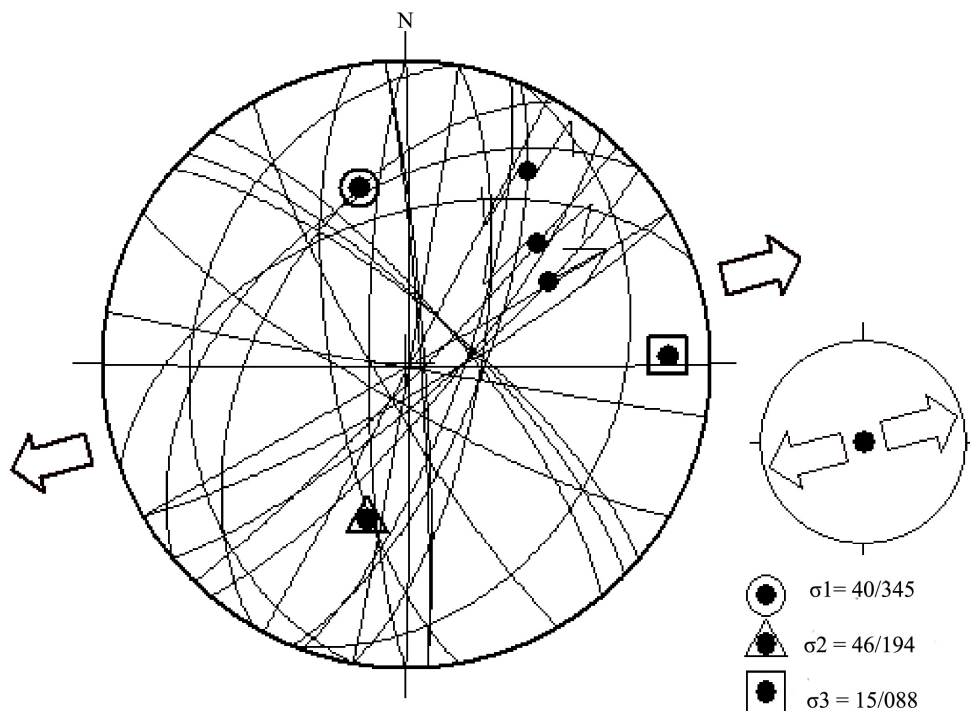


Figure 28 lower hemisphere Schmidt stereo-plot showing paleostress analysis result of fault planes and slickensides using Rotation Optimization Method; σ_1 , σ_2 and σ_3 are maximum, intermediate and minimum principal stresses, respectively.

In order to see if there was a change in the direction of extension with time, stress analysis was performed on the younger NE-SW oblique slip fault set alone. However, the direction remains E-W. This result implies that the extension direction in the area has not changed from the commencement of the rift that led to the formation of N-S faults up to present. This result supports the analysis made in section 4.2.2.

This finding bridges the gap in suggestions on neo-tectonic extension of the rift that has been forwarded by different authors. Bosworth and Strecker (1997) advocated a NW-SE neo-tectonic extension from their work on central Kenya Rift while Atmaoui and Hollnack (2003) argued an E-W to ESE-WNW neotectonic extension for the Lake Magadi area by assuming the NW-SE dextral movement is localized. However, both views did not realize the existence of the sinistral oblique slip NE-SW fault nor did they consider contribution of the strike slip E-W.

4.3. Discussion

This section summarizes the lithologic observations and discusses the structural field data analysis and finding. Lithologic field observation showed that the volcanic rocks in the area are mainly trachytes with some mafic outcrops while the sediments are found deposited on the grabens.

The structural field data were grouped into sets of certain trends using rose diagram. The main sets are normal N-S, dextral NW-SE, strike slip ENE-WSW and sinistral NE-SW trending faults. The N-S and ENE-WSW structures are in general agreement with the remote sensing results (section 3.3.1). While the NW-SE and NE-SW faults observed in the field are reactivation of pre-existing structures and they are represented with Z and S fault patterns in the remote sensing data, respectively.

Crosscutting relationship among the different fault sets show that the N-S faults are the oldest faults in the area since they are cut by all set of faults and the reactivated NE-SW faults are the youngest faults. All the fault sets have been reported from different parts of the EARS in general and from the Kenya Rift in particular. However, the sinistral NE-SW fault has not been reported from the Lake Magadi area.

The presence of four set of faults (oldest normal N-S faults, dextral NW-SE, strike slip ENE-WSW and youngest sinistral NE-SW) having different styles and different relative ages signify that there has been geodynamic change in tectonics of the rift that could have resulted in the formation of the four fault sets. This tectonic phenomenon is explained by Anderson's theory of faulting. At its early stage, the rift experienced normal faulting under E-W extension; then the rift encountered geo-tectonic change that reactivated pre-existing structures creating dextral NW-SE, strike slip ENE-WSW and sinistral NE-SW faults under E-W extension. This analysis suggests that the rift maintained an E-W direction of extension throughout its life span and the E-W extension was verified by the paleostress analysis. Further more, the paleostress analysis was performed on the younger NE-SW oblique slip fault set alone in order to check if there was a change in the direction of extension with time.

However, the direction remains E-W implying that the neotectonic extension of the Lake Magadi area is E-W.

Different suggestions on neo-tectonic extension of the Kenya Rift have been forwarded by different authors. Bosworth and Strecker (1997) advocated a NW-SE neo-tectonic extension from their work on central Kenya Rift by assuming the NW-SE structures as direction of extension while Atmaoui and Hollnack (2003) argued an E-W to ESE-WNW neotectonic extension for the Lake Magadi area by assuming the NW-SE dextral movement is localized; however, the NW-SE structure occurs in all parts of the Kenya Rift. Both views did not realize the existence of the sinistral oblique slip NE-SW trending faults which were created under an E-W extension to counterbalance the NW-SE faults. Therefore, the finding of sinistral oblique slip NE-SW faults bridges the gap in suggestions on neo-tectonic extension of the rift that has been forwarded by different authors.

5. Processing and analysis of geophysical datasets

The geophysical datasets include airborne magnetic data, ground survey magnetic data and resistivity imaging data. All datasets were used for surface and subsurface structural and lithologic interpretation. The airborne magnetic data covers the whole study area and its surrounding while the ground surveyed magnetic data and resistivity imaging data have limited coverage since they were collected from selected sites in the study area.

5.1. Magnetic data

Magnetics is a technique that measures the magnetic field of the earth. Subsurface structures and anomalous geological bodies can be identified with the help of magnetic survey. Owing to their magnetic minerals, many geological formations have associated magnetic field. Generally, metamorphic and igneous rocks show variable magnetic properties where as sedimentary rocks are usually non-magnetic.

Magnetization in rocks is classified in to induced and remanent magnetization (Reeves, 1989). Induced magnetization (J_i) is the result of the present day geomagnetic field. It is expressed as $J_i = kF$ where J_i = magnitude of induced magnetisation, F = magnitude of earth's magnetic field, k = magnetic susceptibility of the rock. Remanent magnetization (J_r) is not related to the present day's earth magnetic field; rather it is acquired by the earth's magnetic field that existed when the rock was formed (Dobrin and Savit, 1988).

Magnetic data can be collected via airborne technique or ground surveying. In this research, both aeromagnetic and magnetic ground survey datasets were used.

5.1.1. Aeromagnetic

A pre-processed aeromagnetic grid was obtained and a subset of total magnetic intensity (TMI) for the study area was created. Then analytical signal was applied on the TMI and depth of the magnetic sources was estimated using 3D Euler deconvolution.

5.1.1.1 Data source and pre-processing

The aeromagnetic dataset used is part of the African Magnetic Mapping Project (AMMP) which compiled airborne magnetic data covering most part of Africa (Barritt, 1993). The airborne survey covering the study area was conducted in 1987 by Compagnie Générale de Géophysique (CGG) with line spacing of 2 km and flight direction of 90^0 (W-E) at a flying height of 2896 m above sea level. The magnetic data was processed by AMMP that included levelling correction and regional field removal and then creating a 1km by 1km cell size magnetic grid with a projection system of AMMP grid.

TMI map

Total magnetic intensity (TMI) grid and analytical signal grid of the Lake Magadi area are shown in Figure 29 A and B, respectively where the study area is represented with rectangular box. In both grid maps, the magnetic highs and lows are shown with red and blue colors respectively. However, outlining lithologic units on the TMI map was difficult due to the asymmetrical shape of the anomalies so that the analytical signal map was used for lithologic interpretation.

5.1.1.2 Data enhancement and analysis

Magnetic anomalies are the result of different geologic features located at variable depths and the anomalies are interpreted depending on their wavelengths (anomaly widths). Short wavelengths are the result of shallow sources where as long wavelengths are the result of deep sources (Grauch, 2002). Therefore, image enhancement is essential in separating and amplifying the subtle anomalies caused by different sources that may not be visible in the total magnetic grid.

In this research analytic signal was used to interpret the lithologic units since it is good in outlining the contacts between rocks (Parsons et al., 2006). Moreover, downward continuation and vertical derivative that enhance shallow magnetic sources (Dobrin and Savit, 1988; GETECH, 2007; Kis and Pusztá, 2006) were attempted. However, the derivatives introduced too much noise (possibly because magnetic data was recorded at a high flying height of 2896 m) so that they are not shown here.

Analytic signal map

The absolute value of analytic signal is defined as the square root of the squared sum of the vertical and the two horizontal derivatives of the magnetic field (Nabighian, 1984; Roest et al., 1992).

$$|AS(x,y)| = \text{SRT} [(dT/dx)^2 + (dT/dy)^2 + (dT/dz)^2] \dots \dots \dots \text{Equation 3}$$

Where AS(x,y) is the amplitude of analytical signal at point (x,y) and T is the total magnetic field at point (x,y).

Regardless of the ambient magnetic field and source magnetization directions, analytic signal shows maxima on the magnetic contrasts and over the magnetic sources; thus, position of the maxima outlines of magnetic sources (De Castro et al., 2007; GETECH, 2007; Roest et al., 1992).

Updating the geological map using analytic signal map

Analytic signal map of the total magnetic grid for the Lake Magadi region (Figure 29 B) and for the study area (Figure 30 B) were created in Oasis. The maps produced symmetrical signal of the anomalies and clearly outlines the lithologic units as magnetic highs and lows where the signals have formed zones.

The analytical signal maps were compared with the existing regional and local geological maps in which good matching were observed. For example, the low magnetic signal in south western part of

the area has been reported as basement rock (quartzite and schist) and the high signals coincide with basalt rocks and volcanoes (mainly basaltic) in the region (see the labels in Figure 29 B). Moreover, the local analytical signal map (Figure 30 B) shows good matching with the local geology (Figure 30 A). For example, the basalts (Kardiya basalt and Ol Tepsi basalt) and the volcanoes (Lenderut, shanamu and Olorgesailie) have high signals.

After verifying the analytical signal map using the known geologic units, it was used to classify the undifferentiated units and update the existing geological map of the area. Geologic works in the southern Kenya Rift by Baker and Mitchell (1976) and Baker (1958) indicate that the rift had encountered basaltic and trachytic volcanic episodes resulting in a basaltic and trachytic rocks in the area. Based on this fact, by referring the existing geological maps and the ASTER image as well as by considering wavelength of the anomaly and taking field observation into account, interpretation of the analytical signal was made. Short wave wavelength anomalies are caused by shallow sources or surface outcrops while long wavelength anomalies are caused by deep seated anomalies.

Owing to its constituent minerals (mafic minerals and oxides of iron), basalt shows magnetic property. Thus, in the study area basalt corresponds with the high magnetic signal which appears as red to pink colour in the analytical map Figure 30 B. The Lenderut volcano has high value of analytical signal which is interpreted as basaltic with name assigned Lenderut basalt. The rocks of Olorgesailie volcano and Shanamu volcano have been reported as trachyte and basalt by Baker (1958); however, there was no further classification of the units. Based on the magnetic interpretation (Figure 30 B), south eastern portion of the Olorgesailie volcano is basalt. Besides, the Shanamu volcano has high magnetic signal which is interpreted as basalt. Thus, the basalts in Olorgesailie and Shanamu volcano are assigned Olorgesailie basalt. Whereas the long wave length signals (red colour) around Lenderut volcano, Shanamu volcano and Olorgesailie volcano could be due to basalts occurring on subsurface.

The sediments in the area are not thick (maximum 49m as calculated by ground magnetic survey and 30-60m from borehole data (Baker, 1958)) and they occur on few grabens so that their effect on the airborne magnetic intensity is not significant. Hence, the low magnetic signal in the map is interpreted as trachyte which has low content of mafic minerals.

5.1.1.3 Depth estimation using 3D Euler deconvolution

Determining depth of a magnetic source is important aspect of magnetic analysis since it provides surface and subsurface information of the rock units and the geologic structures under investigation. Different depth estimation methods exist; for example 3D Euler deconvolution (Reid et al., 1990), the 3-D analytic-signal technique (Roest et al., 1992), the enhanced analytic-signal technique (Hsu et al., 1996) and Source Parameter Imaging SPITM method (Thurston and Smith, 1997).

In this study 3D Euler deconvolution was used owing to its multi depth solution capacity and availability of the algorithm in Oasis and it is a commonly used method (Mushayandebvu et al., 2001; Reid, 1995). 3D Euler deconvolution is independent of magnetic field direction, dip or strike of the magnetic feature and it is insensitive to the direction of induced and remnant magnetisation vectors (Reid et al., 1990). The equation of Euler's homogeneity relation is written as:

$$(x - x_0) dT/dx + (y - y_0) dT/dy + (z - z_0) dT/dz = N(B - T) \dots \dots \dots \text{Equation 4}$$

Where (x_0, y_0, z_0) is the position of a magnetic source whose total field T is detected at (x, y, z) . The total field has a regional value of B . The degree of homogeneity N may be geophysically interpreted as a structural index (SI), which is a measure of the rate of change with distance of a field.

The 3D Euler deconvolution involves calculation of the three orthogonal derivatives of the total magnetic field along x , y and z directions, choosing an appropriate square window size that is applied to the data grid of total magnetic field & the three derivatives, setting structural index and uncertainty of solutions then finally solving (x_0, y_0, z_0) with in the window. The window moves through out the whole data grid.

Window size, structural index and solution uncertainties are set by user. Window size is a function of the grid cell and it must be set in such a way that it includes large variations but it does not skip small details. Structural index which relates to source type (e.g., contact, dike, and point) is set by considering geological knowledge of the survey area as well as structure that the interpreter is intending to represent; some magnetic models and their SI values are summarized in Table 4 The structural index can be determined by observing the clustering of solutions for different SI values; for a particular feature, the correct SI yields a tight cluster (Dewangan et al., 2007). Solution uncertainties of depth (z) and location (x, y) of the source are calculated as a percentage of the modeled depth by inversion of the data while solving the Euler's equation. The uncertainty values are used for evaluating the depth model solution; solutions with high uncertainty value are eliminated.

Table 4 Structural index and corresponding magnetic source models (Reid et al., 1990; Thompson, 1982)

Structural Index (SI)	magnetic source model
0	Contact
0.5	Fault
1	Sill/dyke
2	Pipe

3	Sphere
---	--------

3D Euler deconvolution applied on the study area

In this research, the standard 3D Euler deconvolution was used for the depth estimation with a depth error of less than 15%. Considering the 1km resolution of the dataset and the anomaly width observed in total magnetic intensity map that reach about 10km on average, window size of 10 was found appropriate for this study. The depth estimation was applied by varying structural index values. The best Euler clustering solutions for the window size of 10 was obtained using SI of 1 and 0.5 resulting depth range of 2m to 2.4km (Figure 31). The Euler solutions form linear feature along N-S, NW-SE, ENE-WSW and NE-SW as labeled on the figure. Such linear alignment supports the presence of four sets of faults in the area which were obtained from the ASTER datasets and SRTM (section 3.3.1) and observed in the field (section 4.2.1). The depth range extends from surface to about 2.4km deep which imply that the faults are acting as conduits to the hot-springs in the area.

As shown with white arrow labels in Figure 31, the alignment of Euler solutions coincide with the change of orientation of the N-S faults, which marks the NW-SE and NE-SW faults that substantiates the Z and S fault patterns discussed in section 3.3.1.

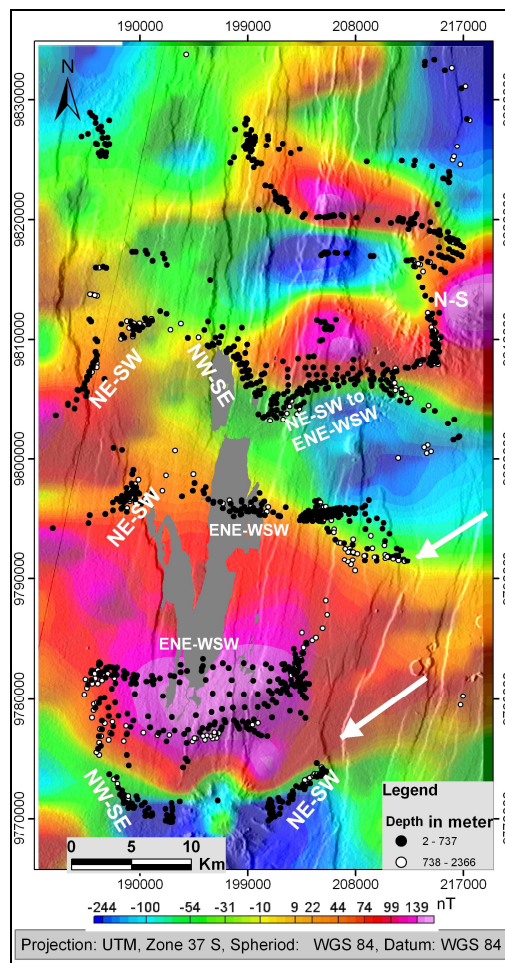


Figure 31 TMI pan-sharpened with hill-shade of ASTER DEM the Lake Magadi is represented in gray colour. 3D Euler was applied with SI equal to 1 and 0.5 and window size of 10.

5.1.2. Ground survey magnetic data

The ground magnetic data collected from the study area were corrected for diurnal and regional magnetic effects and then the magnetic data was enhanced using analytical signal. Finally, depth of the magnetic sources was estimated using 3D Euler deconvolution.

5.1.2.1 Data collection

The magnetic ground survey was conducted on two sites (Figure 32 and Figure 33) using the magnetic field equipment G856 proton precession magnetometer. The sites are located in northern part of Lake Makadi which is seismically active area. Magnetic profiles in both sites were run W-E which is perpendicular to strike of the dominant fault set in the area.

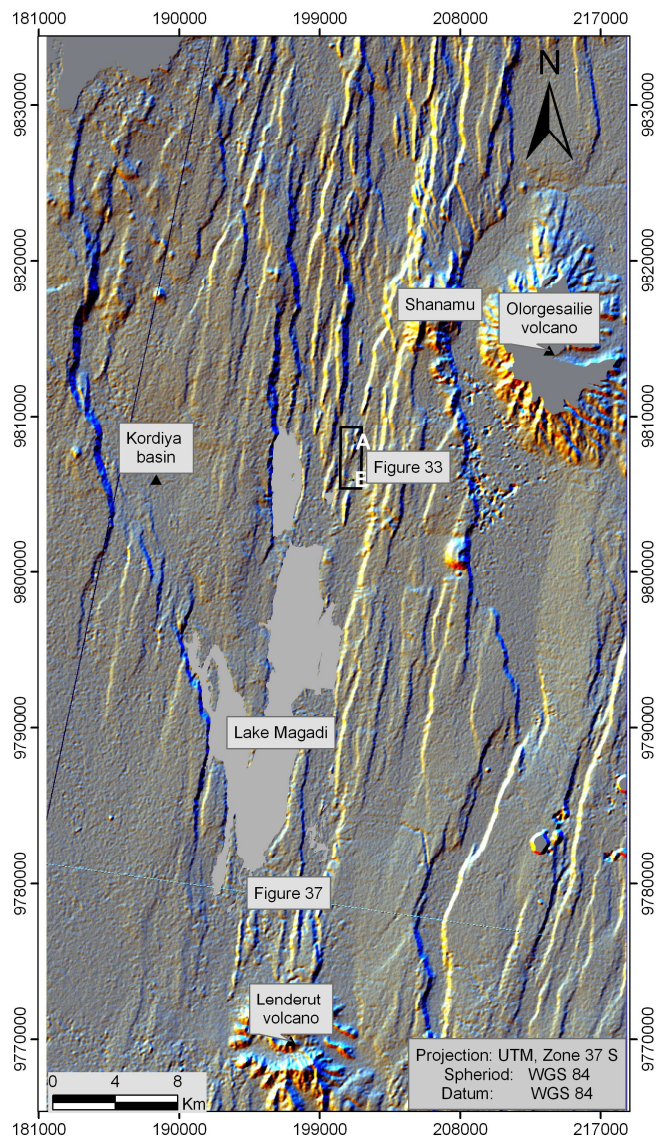


Figure 32 locations of magnetic survey sites, zoom in of the ground survey magnetic sites is shown in Figure 33.

A) The rupture site

As a result of the seismic activity in the area, recent rupture has occurred in this site. On this site, twelve parallel magnetic profiles were carried out. Profiles spacing was 25m and magnetic reading was taken every 10m.

B) South of the rupture

This site is located about 2km south of the recent rupture. Three parallel magnetic profiles were conducted having line spacing of 25m and with magnetic reading taken every 10m.

5.1.2.2 Corrections

Diurnal correction

Short period variations (diurnal and magnetic storms) of magnetic field with time must be monitored and subtracted by suitable procedure. Diurnal variations occur during local daylight hours and they are direct or indirect consequence of solar winds with respect to rotation of the earth (Roux, 1980).

In order to monitor the diurnal variation, base stations were established for each site. Magnetic readings at the base stations were recorded hourly during the survey dates. Ultimately diurnal correction was made to all the magnetic datasets of all the sites using the respective base station readings.

Removal of International Geomagnetic Reference Field (IGRF)

In magnetic measurements, the recorded value is the sum of local magnetic field caused by the lithologic units and regional magnetic field of the earth. Measurements taken in such locality show anomaly from the undisturbed earth's magnetic field in the vicinity; size of the anomaly vary depending on the depth of burial, degree and direction of magnetisation as well as orientation (strike & dip) of the geologic unit in relation to the direction of the earth's field at that locality (Roux, 1980).

In order to map local variations in magnetic field attributable to the local geology and get the local magnetic anomaly, the global magnetic field must be subtracted from the magnetic data. The removal is done through International Geomagnetic Reference Field (IGRF) which is mathematical model of the magnetic field of the earth (Dobrin and Savit, 1988). IGRF is a function of date, elevation and location which is updated every five years based on magnetic observation stations in different part of the world. IGRF correction is made by subtracting IGRF value of each point calculated by recent IGRF model from the measured magnetic value.

In the study area, IGRF of each point (considering the magnetic survey date, location and elevation of each point) was calculated using the IGRF2005 model embedded in Geo-soft Oasis montaj. The calculated IGRF value was subtracted from each point.

5.1.2.3 Data analysis

After setting projection of the database to WGS84 zone 37S, grids of the corrected magnetic datasets were generated using the minimum curvature gridding method with a resolution of 10m. The magnetic grids were enhanced using different enhancements (eg analytical signal and vertical derivatives) with best result obtained from the analytical signal. Depth estimation of the magnetic sources in the sites was accomplished with 3D Euler deconvolution by varying structural index.

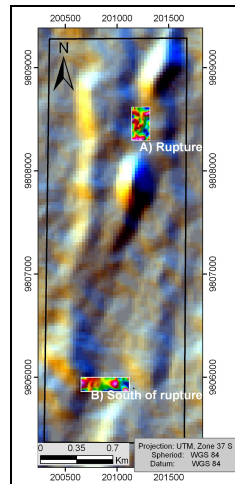


Figure 33 Zoom in from Figure 32 to show the magnetic survey sites; A) rupture site, B) south of rupture.

A) TMI and analytical signal of the rupture site

Total magnetic intensity grid was generated with grid cell size of 10 m (Figure 34 a). In order to see distribution of the rock units and structures in the site, analytical signal was applied on the TMI as shown in Figure 34 b. The volcanic rocks on western and eastern part of the graben are represented by high signals while the sediments (clay and chert) filling the graben are shown with low value of analytical signal. Spots of high signals also appear in the graben which is possibly due to noise because the signals have small wavelengths, which is less than the line spacing used in the survey. The N-S fault structures observed in the field (white lines) and the surface rupture (black lines) are represented as linear feature between the magnetic highs and lows on the analytical signal map. The result of ground magnetic data was integrated with the result of resistivity imaging from the rupture site (section 6.1.2).

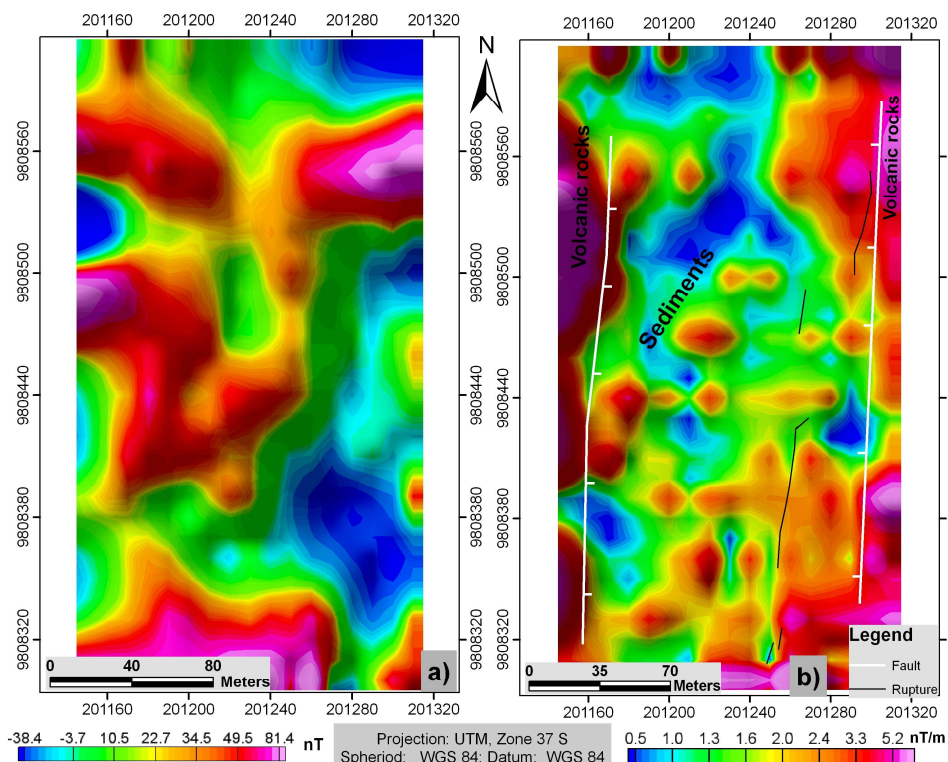


Figure 34 colour shaded maps of a) TMI and b) analytical signal of TMI; the rupture and the faults observed in the field are respectively indicated with solid lines with dotted lines in both maps.



Photo 21 the surface rupture observed in the field, north is indicated with the white arrow.

3D Euler deconvolution

Furthermore, depth of the magnetic sources was estimated using 3D Euler deconvolution with a window size of 5 and depth error of less than 15%. Different structural indexes were experimented; the best clustering of the Euler solution was obtained with SI value of 2. The depth estimates show that the magnetic source in the site occurs in the depth range of 13 to 41 meters (Figure 35). Thus, thickness of the sediments in the site has maximum thickness of 41 meters.

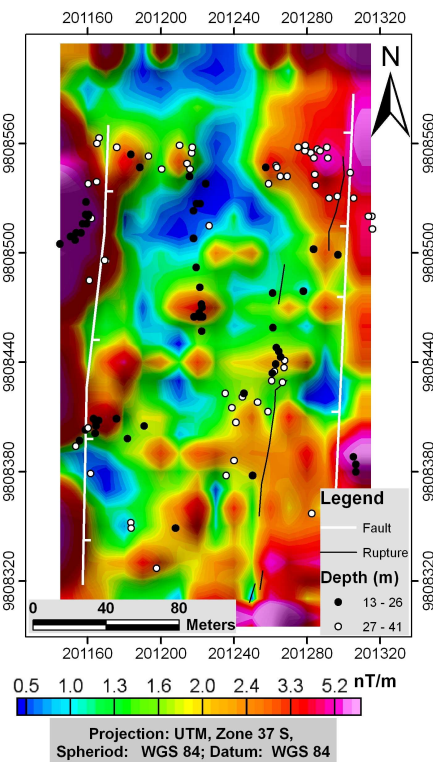


Figure 35 Euler depth solution overlying the analytical signal of TMI; SI is 2 and window size is 5. The rupture is indicated with solid lines and the faults with dotted lines.

B) TMI, analytical signal and 3D Euler deconvolution of South west of the rupture

Total magnetic intensity map having a resolution of 10 m was generated (Figure 36 a) from the corrected magnetic data. Analytical signal map was to identify the rock units in the site. The analytical signal map depicts the graben and its low signal sediments distinguished from the high signal volcanic rocks. The N-S fault structures which were observed in the field to separate the volcanic hills from the graben on its western and eastern sides are represented as a linear feature between the magnetic highs and lows.

3D Euler depth estimate was applied with a window size of 5 and depth error of less than 15% by varying the structural indexes. The best clustering of Euler solution was obtained with SI value of 0.5 giving a depth range of 12 to 49 meter (Figure 36 b). The result shows maximum thickness of the sediments in the site is 49 meter.

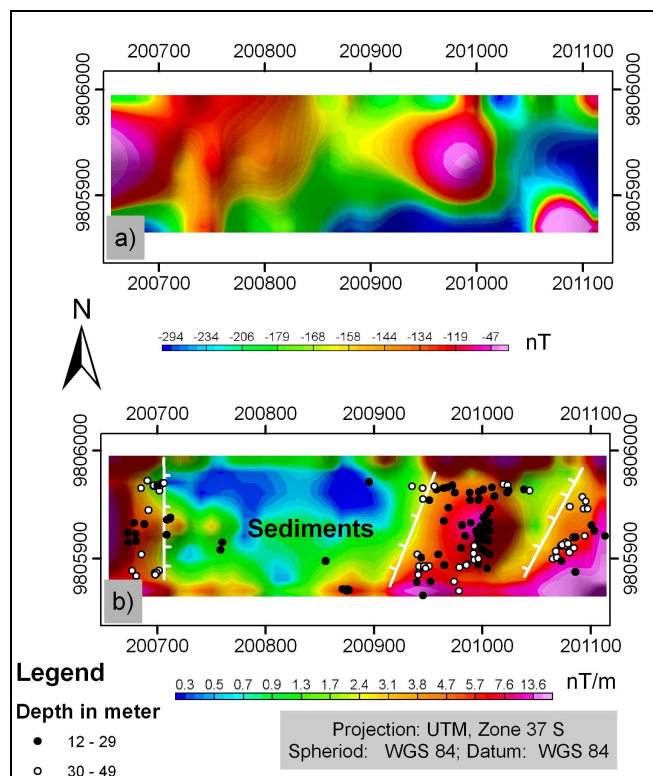


Figure 36 colour shaded maps of a) TMI and b) analytical signal of TMI overlain with Euler solution SI is 0.5 and window size is 5.

5.2. 2D Resistivity imaging

Resistivity is a fundamental property of rocks (Dobrin and Savit, 1988) so that resistivity measurements can provide useful subsurface structural and lithologic information. Resistivity technique has been widely used in groundwater, geological and engineering investigations. In this research, resistivity imaging (tomography) technique has been used lithologic and structural investigation. The tomography technique involves the arrangement of collinear and equally spaced multiple electrodes on the surface. It lays multi-electrode arrays and automatically records profiling plus sounding simultaneously providing 2D image of the subsurface.

5.2.1. Data collection

Resistivity data was collected in the rupture area (Figure 37) using the resistivity imaging equipment SYSCAL R1 PLUS SWITCH-72. The rupture area is the same as the ground magnetic data were collected (section 5.1.2).

The SYSCAL equipment combines profiling using Wenner array and sounding using Schlumberger array. The equipment has 72 electrodes that were laid out equally to the left and right of a survey center line with 5m spacing such that a survey line covers 360 m length and 50 m depth of penetration. After configuring the electrodes, the program installed in the equipment was setup to automatically execute the survey. In order to increase the depth of penetration, a “roll-along” was used. During roll-along, the already recorded data from the 72 electrodes were kept in the memory of the equipment and 18 electrodes were moved from one end of a profile line to the other end where the profile was extended so that the total profile length reaches 450 m and a 65 m depth of penetration is achieved.

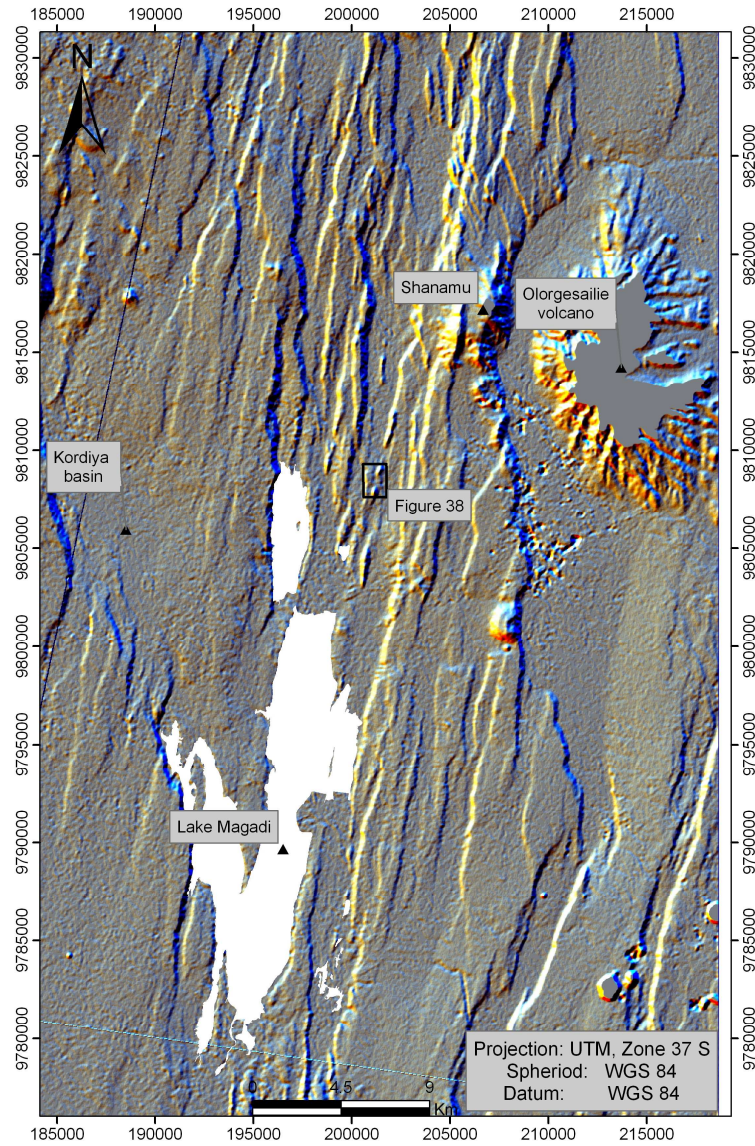


Figure 37 Location of the resistivity survey site (rupture area), zoom in of the site is shown in Figure 38.

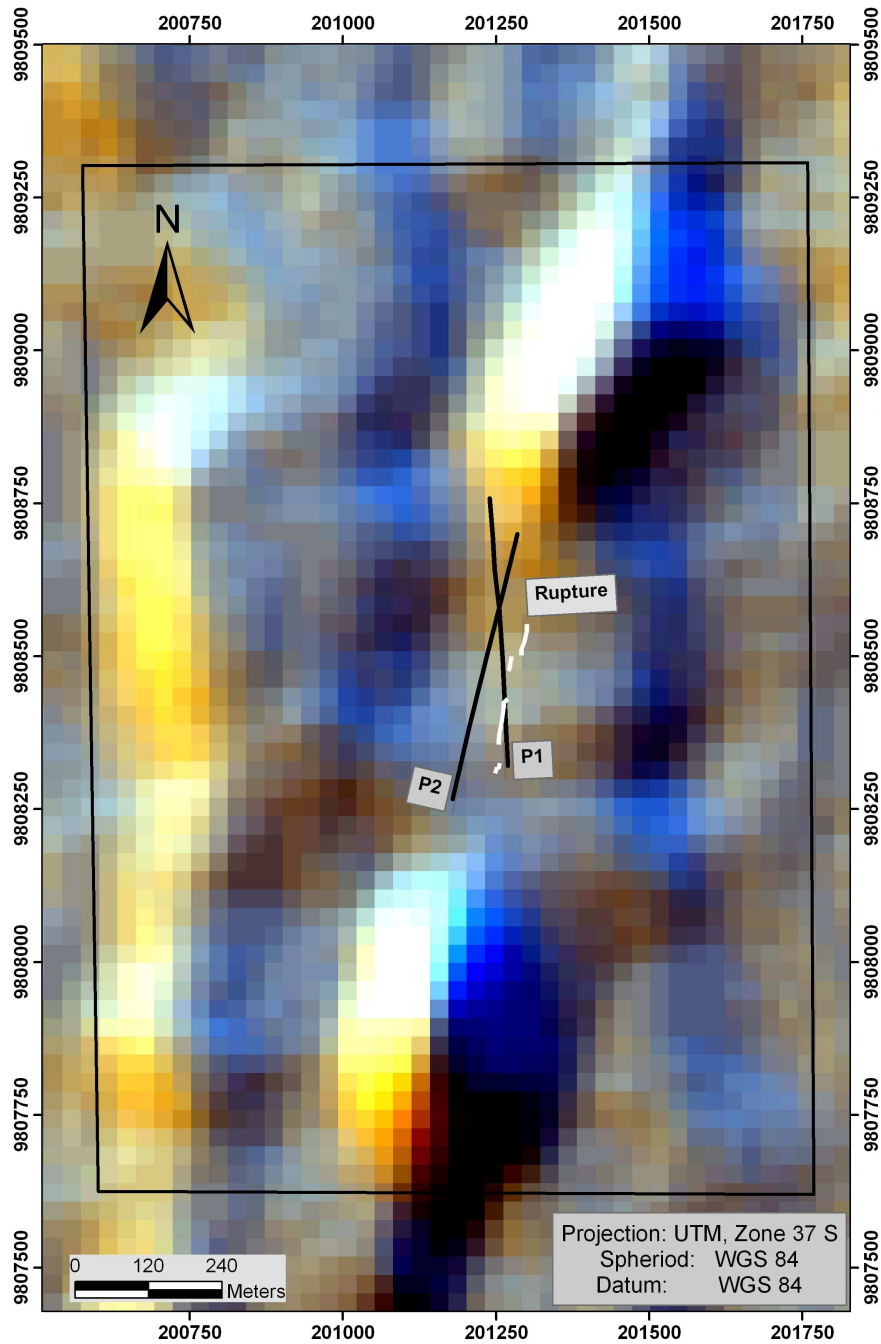


Figure 38 resistivity profiles (P1 and P2) taken in the rupture site and the surface rupture is indicated with white lines.

5.2.2. Data analysis

After downloading data from the imaging equipment to a laptop, the measured apparent resistivity data were filtered in order to remove bad signals. The resistivity data were analyzed in Earth Imager in order to create cross-section for calculated apparent resistivity and inverted resistivity using a smooth model inversion method that is stable and robust.

In this area, two profiles (P1 and P2) intersecting each other (Figure 38) were surveyed. In addition, the P1 crosses the recent surface rupture. The intersection of the two profiles and the intersection of the P1 with the rupture are shown in Figure 38 and indicated with arrows in

Figure 39 and

Figure 40. The main aim of these two survey profiles was to deduce subsurface behavior of the rupture (indicated with arrow at 108m and 150m in P1) and to explore if there are other possible hidden ruptures in the area. The rocks observed in the area include highly fractured volcanic rocks, chert and clay.

Profile one

This section was carried out along p1 (Figure 38) and intersects p2 at 262 meter. The two profiles were made to intersect in order to compare the results. Both profiles resulted in similar thickness estimate based on the low resistivity data at the intersection. The intersections of the P1 with the rupture, indicated by black arrows in Figure 39, show abrupt changes in resistivity. In particular, the rupture at point 150 m of the P1 intersecting the surface rupture suggests that the rupture persists at further depths and it is labeled as rupture zone 1. On the other hand, the intersection of P1 with P2 (indicated with dotted arrow) show abrupt change of resistivity value which continues to a subsurface depth of greater than 66m implying that there is another rupture in the area and it is labeled as rupture zone 2. The presence of N-S to NNE-SSW trending surface and hidden ruptures which persist at further depth signify that the site is active resulting intense rupturing under E-W neotectonic extension.

Thickness of the low resistivity material (chert and clay) along the profile reaches 17m. The depth estimates in P1 are in agreement with the depth estimates from p2 and with depth estimates from ground magnetic data (i.e. 13 to 26m, see section 5.1.2). In the first 135m length of the P1, the higher resistivity value toward the surface corresponds with the fractured volcanic rock that was observed to be outcropping (with thin soil cover in some cases) in the site.

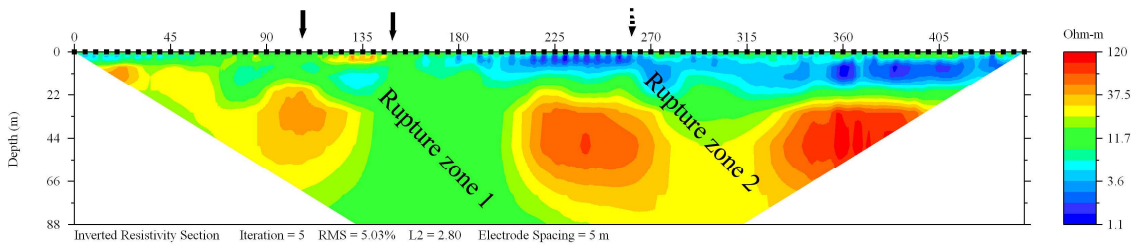


Figure 39 inverted resistivity section along profile one on the rupture site. Iteration = 5, RMS = 5.03%, Electrode spacing = 5m

Profile two

As shown in Figure 38, P2 intersects with P1; the point of intersection is at 325 meter as marked with the arrow in Figure 40. The intersection supports the existence of the subsurface rupture (rupture zone 2) mentioned in discussion of P1.

The thickness of the low resistivity material along this profile reaches 22m. This depth is in agreement with the depths estimated from the ground magnetic data ranging from 13 to 26 m along this profile (section 5.1.2). The occurrence of fractured chert and clay explain the top low resistivity unit in the site. The relatively higher resistivity unit in the profile is associated with the fractured volcanic rock.

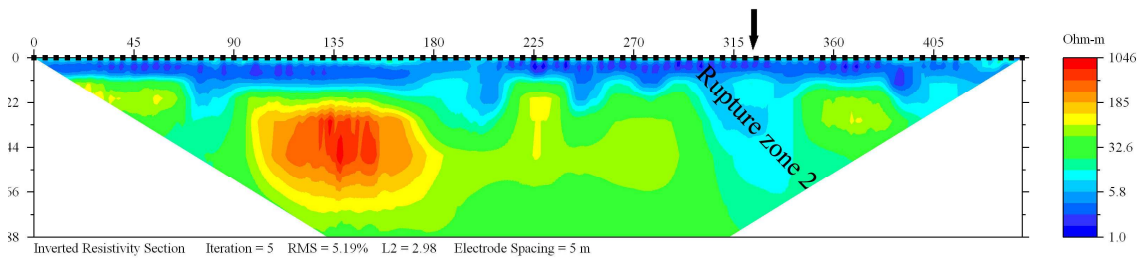


Figure 40 inverted resistivity section along profile two on the rupture site. Iteration = 5, RMS = 5.19%, Electrode spacing = 5m

5.3. Discussion

This section discusses the results obtained from the analysis of aeromagnetic, ground magnetic and resistivity datasets. Analytical signal and 3D Euler deconvolution were used for analyzing the magnetic datasets. For the resistivity data, smooth model inversion method in Earth imager was used to produce 2D inverted resistivity section.

The analytical signal applied to the airborne magnetic data was useful in outlining the lithologic units. The magnetic analytical signal map was crosschecked with existing regional and local geological maps in which it showed good matching. However, the local geological map is old and it was produced by reconnaissance mapping so that it had undifferentiated units in some places. Based on previous works (that showed the area is mainly basalt and trachyte), interpretation from the ASTER image and field observation, interpretation from the analytical signal was used for updating the existing geological map. For example, the high magnetic signal rocks in the Olorgesailie volcano and Shanamu volcano were classified as Olorgesailie basalt; the Lenderut volcano was assigned basalt since it has high analytic signal. The 3D Euler deconvolution was applied to deduce surface and subsurface depth information of the rock units and the geologic structures in the study area. The 3D Euler solution points showed alignment along N-S, NW-SE, ENE-WSW and NE-SW suggesting the presence of four set of structures that trend along the alignment of the Euler solutions. This result agrees with the result of remote sensing datasets (section 3.3.1) and the field data (section 4.2.1).

The ground magnetic data collected from the rupture area and 2km south of the rupture were analyzed using analytical signal and 3D Euler deconvolution. The analytical signal of both sites was good in differentiating the sediments (chert and clay) from the volcanic rocks and in delineating the structures in the area. 3D Euler result gave depth estimates of the sediments ranging 13 to 41m in the rupture area and 12 to 49m for the site south of the rupture area which area in agreement with borehole data of the sediments in the area that range 30-60m (Baker, 1958).

The resistivity data from the rupture area enabled to characterize subsurface nature of the rupture and to suggest the presence of another rupture in the area. Both ruptures continue to a depth of greater than 66m. The presence of N-S to NNE-SSW trending surface and hidden ruptures which persist at further depth signify that the site is active resulting intense rupturing due to an E-W neotectonic extension. Thickness of the low resistivity unit that corresponds to chert and clay from the two resistivity profiles range between 17-22m which is in agreement with depth estimated by ground magnetic data.

6. Dataset integration, discussion and rift development model

6.1. Dataset integration and discussion

The datasets used in this research were integrated in order to check if the structural and lithologic information extracted from the different datasets correlate with each other. The integration was made among the remotely sensed datasets and between field data and the remotely sensed datasets that include ASTER DEM, earthquake epicentre and airborne magnetic data, ground magnetic data and resistivity data. The conjunctive analysis was done in Arc GIS software package by overlying the different datasets on each other after projecting them to the same coordinate system.

6.1.1. Field and remotely sensed datasets

The remote sensing datasets showed two main sets of faults: N-S and ENE-WSW. The N-S set has wide range of trends that include N-S, NNW-SSE and NNE-WSW. This fault set are the dominant structures in the area; in some parts of the study area, they deflect to NNW-SSE and NNE-WSW forming a Z-shape and S-shape patterns, respectively which are due to reactivated NW-SE and NE-SW trending structures. The Z-pattern associated with a dextral NW-SE structure is demonstrated in Figure 41 and Figure 42 A and B which is supplemented by the NW-SE alignment of the 3D Euler depth solutions in the same figures. The S-pattern representing a sinistral NE-SW structure in the ASTER DEM is shown in Figure 43 and it is supplemented with the NE-SW alignment of the 3D Euler depth solutions in Figure 41 with example shown in Figure 43 and in the field photos 11 and 19 showing NE-SE faults (refer to section 4.2.1 under NE-SW set).

The second set of fault extracted from the remote sensing datasets trends ENE-WSW. As shown in Figure 41, some of the Euler depth solutions also align along ENE-WSW. Figure 44 is an example that demonstrates how the two datasets complement each other. Alignment of the Euler depth solutions along ENE-WSW (Figure 44 A) agrees with the ENE-WSW trending faults extracted from the ASTER image, ASTER DEM and SRTM DEM (Figure 44 B).

Therefore, integration of the field observation and the remotely sensed datasets has revealed four sets of faults in the study area: normal N-S, dextral NW-SE, strike slip ENE-WSW and sinistral NE-SW. These faults sets played significant role in development of the rift (section 6.2) and in seismicity of the area. In addition, the presence of these four sets of faults that goes as deep as 2.4km have created conducive environment for the movement of groundwater and its interaction with hot subsurface fluid resulting hot-springs in the area. The high fractal dimension value (2 to 3) analyzed under section 3.3.2 implies that the short faults (<1.6 km) and faults with small throws (<30m) have significant

contribution in the area. Thus, the presence of short faults and faults with small throws coupled with the big faults having different orientation act as suitable conduits for the hot springs.

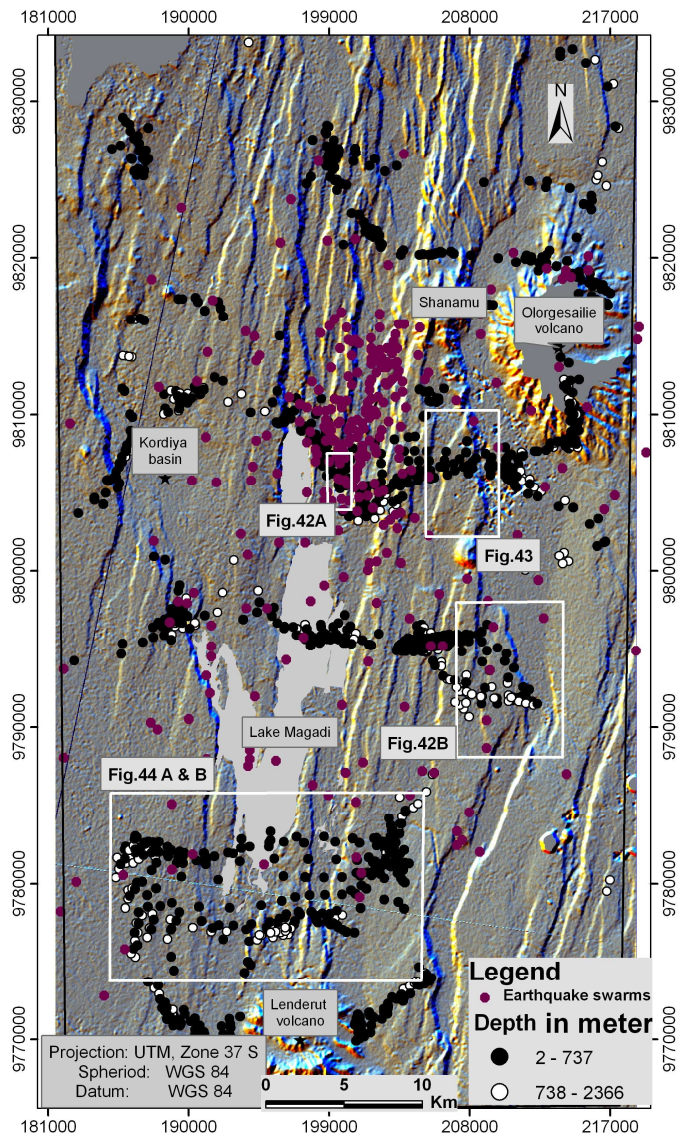


Figure 41 the Euler solution data and the epicenter of the earthquake swarms overlying on the hillshade of ASTER DEM.

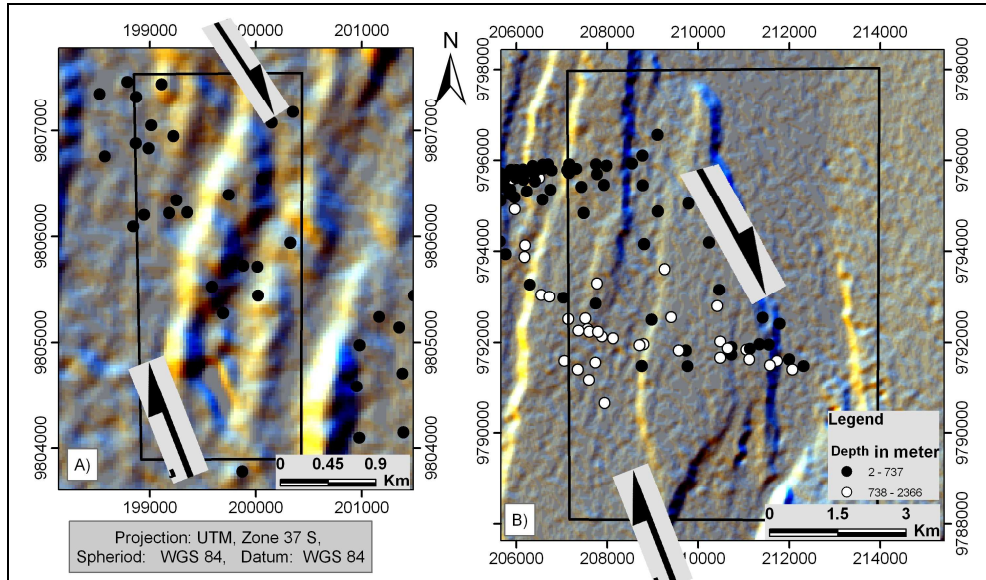


Figure 42 (A) and (B) showing NW-SE structure revealed by the presence of Z shape feature in the ASTER DEM and by the clustering of 3D Euler depth solution along the NW-SE trend. The dextral sense of movement is indicated by the arrows.

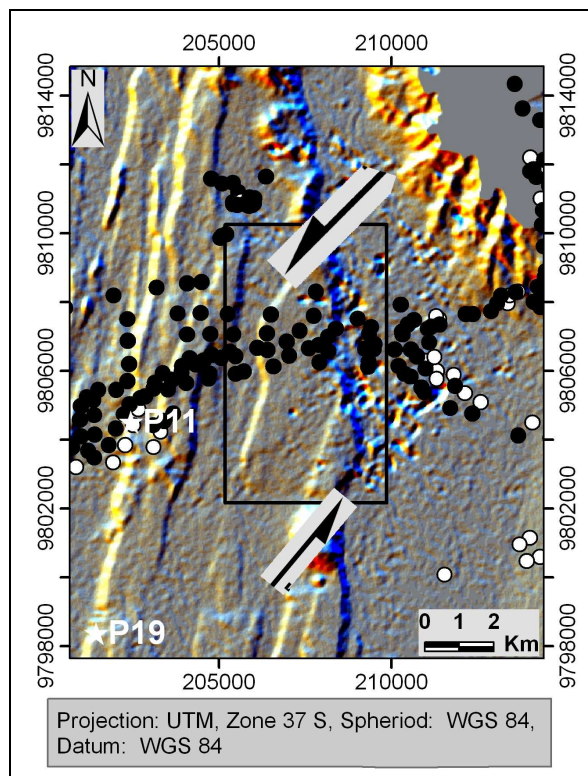


Figure 43 show NE-SW structure revealed by the presence of S shape feature in the ASTER DEM in and by the clustering of 3D Euler depth solution along the NE-SW trend; the sinistral sense of movement is indicated by the arrows. Field observation photos 11 and 19 showing NE-SE faults (see section 4.2.1 under NE-SW set).

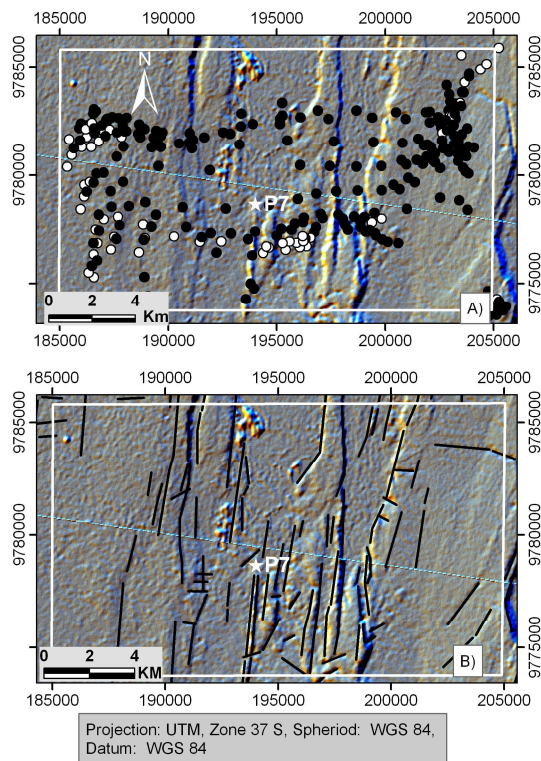


Figure 44 ENE-WSW faults from A) the alignment of 3D Euler depth solution, B) the combined results of ASTER image, ASTER DEM and SRTM DEM. P7 stands for field photo 7 shown in section 4.2.1 under ENE-WSW set.

In the integrated datasets (Figure 41), intersection of the NW-SE and NE-SW structures with the N-S structures coincide with the clustering of the earthquake swarms in the northern part of the Lake Magadi. This implies that the clustering is associated with the intersection of the N-S structures and the reactivated NW-SE and NE-SW structures. Thus the reactivation of the pre-existing structures may have contributed to the clustering of the earthquake swarms in the northern part of the Lake Magadi area. This result supplements the existing understanding proposed by Seht et al.(2001) that the clustering and the shallow hypocenter depths beneath the earthquake cluster are associated with the presence of lower crustal magmatic intrusion since the crustal intrusion may have reactivated the pre-existing structures in the area.

6.1.2. Ground survey geophysical datasets and field data of the rupture area

The surface rupture that was reported from northern part of the Lake Magadi area by Seht et al.(2001) was observed during field observation of this research. The ground magnetic survey and 2D resistivity profiling taken from the site show good matching and have characterized subsurface nature of the rupture. The N-S to NNE-SSW trending surface rupture and the normal faults observed in the field (white lines) and the resistivity profiles (P1 and P2) are overlain on the analytical map of the ground magnetic data (Figure 45). The resistivity cross-sections of P1 and P2 are shown in section 5.2.2.

In the analytical signal magnetic map, the field observed normal faults and surface rupture form a linear pattern between magnetic lows and magnetic highs. On the other hand, the resistivity profile P1

crosses the surface rupture (Figure 45). As discussed in section 5.2.2 and shown in Figure 39, the surface rupture penetrates to a subsurface depth of greater than 66m, which is labeled as rupture zone one. Profile one also intersects with profile two (Figure 45). In the magnetic signal map, the intersection of P1 and P2 is marked with abrupt change of magnetic signal value and forms a linear pattern. In both the resistivity profiles (P1 and P2), the intersection is marked with low resistivity values (Figure 39 and Figure 40) that penetrates to a subsurface depth of greater than 66m. Therefore, by combining the information obtained from the magnetic data and the resistivity imaging profiles, a second rupture which is marked as rupture zone 2 (Figure 39 and Figure 40) is proposed in the site.

The presence of N-S to NNE-SSW trending ruptures which penetrate to a subsurface depth of greater than 66m as verified by the geophysical datasets coupled with the clustering of the earthquake swarms in the area (Figure 41) signify that the present extension direction is E-W.

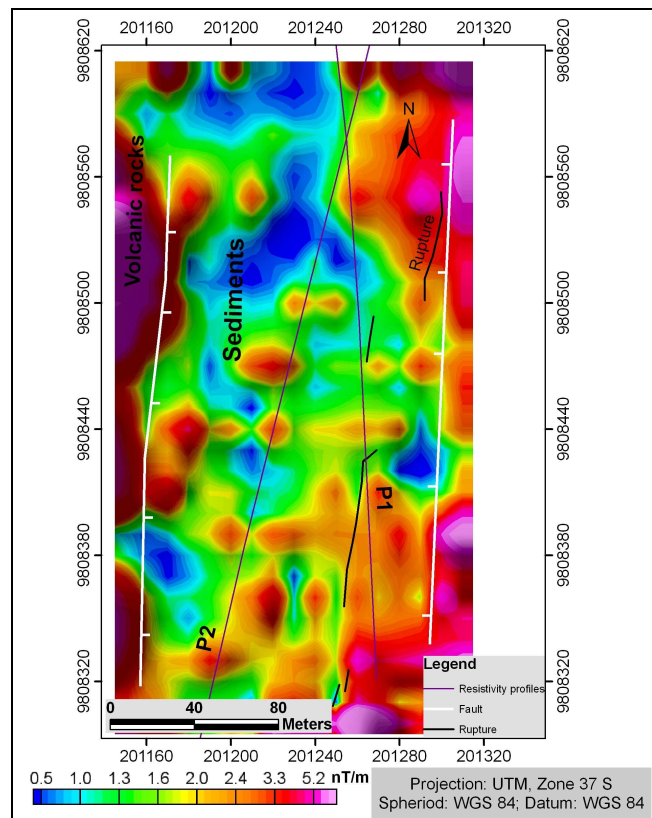


Figure 45 resistivity profiles (P1 and P2), the surface rupture and normal faults observed in the field (white lines) overlaying the analytical ground magnetic map of the rupture site. For resistivity cross-sections of P1 and P2 refer section 5.2.2.

6.1.3. Airborne magnetic data and ASTER image

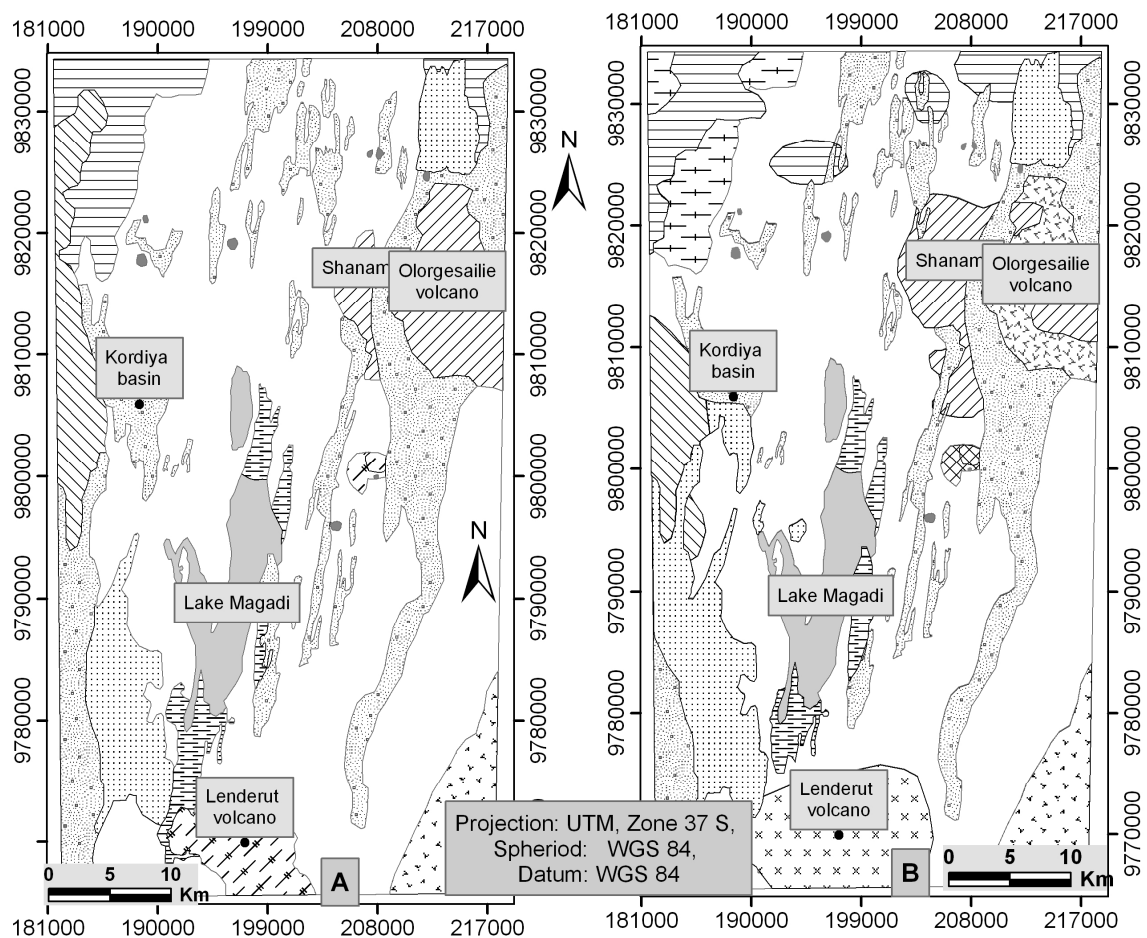
The existing geological map in Figure 46 A was updated to Figure 46 B based on the information extracted from the ASTER images, the airborne magnetic data and the field observations.

Different colour composites of: the ASTER image bands, the principal components and the band ratios were used to analyze the rock types in the area, and the images were useful in discriminating

the sediments as explained in section 3.2.1. Thus, the chert and clay unit in southern part of the Lake Magadi area has been updated based their spectral signature combined with field observation of the unit. Besides, the Tuff and clay unit in the south was updated. The ASTER image, however, was not useful in differentiating the volcanic units except silica index was used to generally asses distribution of the silica rich and silica poor volcanic units, which indicated that the central part of the study are is rich in silica while the flanks of the rift are poor in silica.

To further discriminate the volcanic units, airborne magnetic data was used. The interpretation of the magnetic data is explained in section 5.1.1. The OITepsi basalt and benmoreites, an intermediate rock (Baker et al., 1976) were classified in to two separate units where the high magnetic signal was assigned as basalt and the low magnetic signal as benmoreites. The Pliocene Ologesaile volcanics (mainly basalt and trachyte) covering the shanamu and Ologesaile volcanoes were separated in to Ologesaile basalt (high magnetic) and the remaining units to Ologesaile volcanics (lower magnetic). On the other hand, the Lenderut volcano showed high signal so that it was assigned to basalt.

The area was exposed to basaltic and then to trachytic volcanism (Baker, 1958; Baker et al., 1971). Even though, the basaltic flows were formed earlier than the trachytic flow, the basalts outcrop on flanks of the rift which is due to the normal faulting; it threw down the trachyte in central part of the rift while exposing basalts in eastern and western flanks of the rift as well as in few horsts in the center.



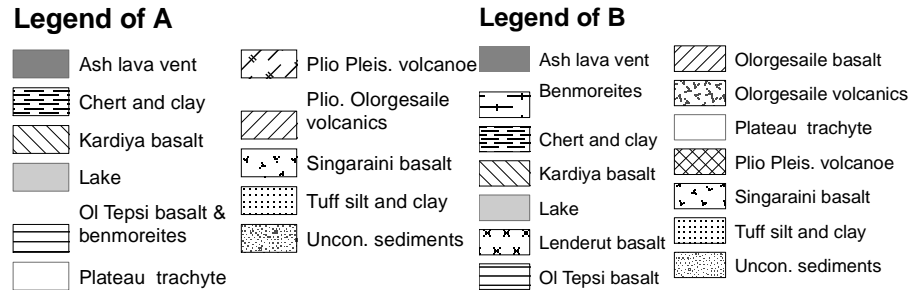


Figure 46 A) existing geological map of the study area B) updated geological map of the study area.

6.2. Discussion of rift development model

Existing model for the central and southern Kenya Rift

Based on the observation of Z and S fault patterns on remote sensing data, Le Turdu et al. (1999) proposed a conceptual rift development model for the central and southern parts of the Kenya Rift (Figure 47). For the central part of the Kenya Rift, they showed that the Z and S patterns were created due to the interference of the N-S faults with pre-existing structures trending NW-SE and NE-SW. Moreover, Le Turdu et al. (1999) observed Z-shaped fault patterns in the Lake Magadi area, and proposed a NW-SE structures. However, S-fault patterns have not been reported from the Lake Magadi area.

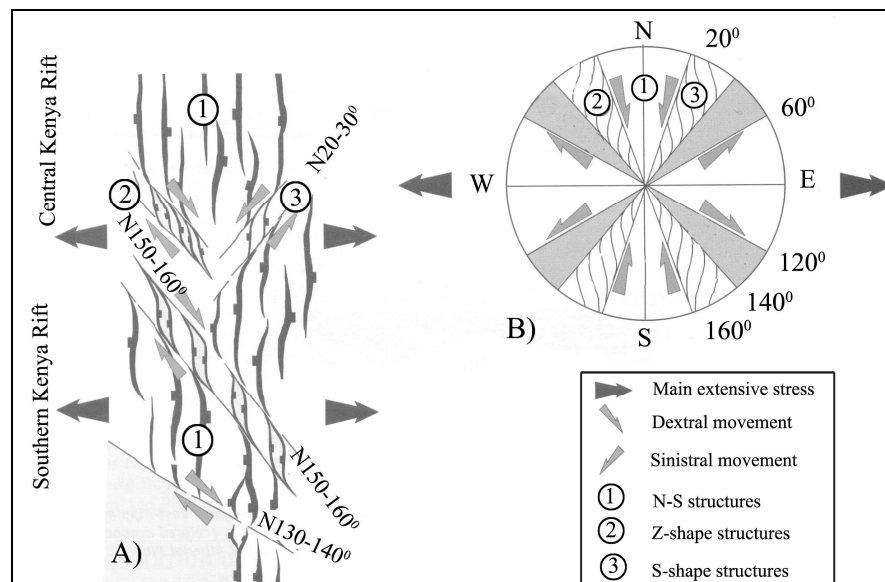


Figure 47 A) Conceptual tectonic development model for the central and southern part of the Kenya Rift, after Le Turdu et al. (1999) showing the normal N-S, the dextral NW-SE (N130-160°) and the sinistral NE-SW (N20-30°) structures created under E-W extension; B) Rose diagram showing orientation of the structures and the corresponding stress fields.

Updating the model of Lake Magadi area

In this research, both Z and S fault patterns (deflection of the prominent N-S normal faults) were observed in the remote sensing datasets that signify the presence of a dextral NW-SE and sinistral NE-SW structures, respectively. Besides, a strike slip fault trending ENE-WSW was observed in the remote sensing datasets. The N-S, NW-SE, ENE-WSW and NE-SW faults were observed in the field and in the airborne magnetic data. All the fault sets occur in different parts of the EARS as discussed in sections 3.3.1 and 4.2.1. The four set of faults (normal N-S, dextral NW-SE, strike slip ENE-WSW and sinistral NE-SW) having different styles and different relative ages were created under an E-W extension which is explained by Anderson's fault model (4.2.2); the E-W extension direction is verified by paleostress analysis (section 4.2.3). In addition, the neotectonic E-W extension direction is supported by the presence of N-S to NNE-SSW trending recent ruptures in the study area.

Therefore, by taking Anderson's fault model into account and by reviewing the existing models for study area, the rift development model of central Kenya Rift proposed by Le Turdu et al. (1999) is extended to the Lake Magadi area with modification. The NE-SW structures were not represented in the model (Figure 47) on the southern part of the Kenya Rift; however, field observation and remotely sensed datasets of the current research have revealed the presence of NE-SW (N30-60) structures in the Lake Magadi area. Hence, the model is modified in order to incorporate the NE-SW structures on the southern part of the Kenya Rift as shown in Figure 48 .

During commencement of the rift, Normal faults (represented with 1 in Figure 48) were created under an E-W extension resulting horst and graben structure in the Lake Magadi area. Later, a geo-tectonic change occurred in the rift; as a result the style of faulting changed from normal fault to strike slip. The strike slip movement created a dextral NW-SE, a strike slip ENE-WSW and a sinistral NE-SW while the extension direction was maintained along E-W (Figure 48). At the present, the extension direction continues to operate along E-W creating a N-S to NNE-SSW trending ruptures.

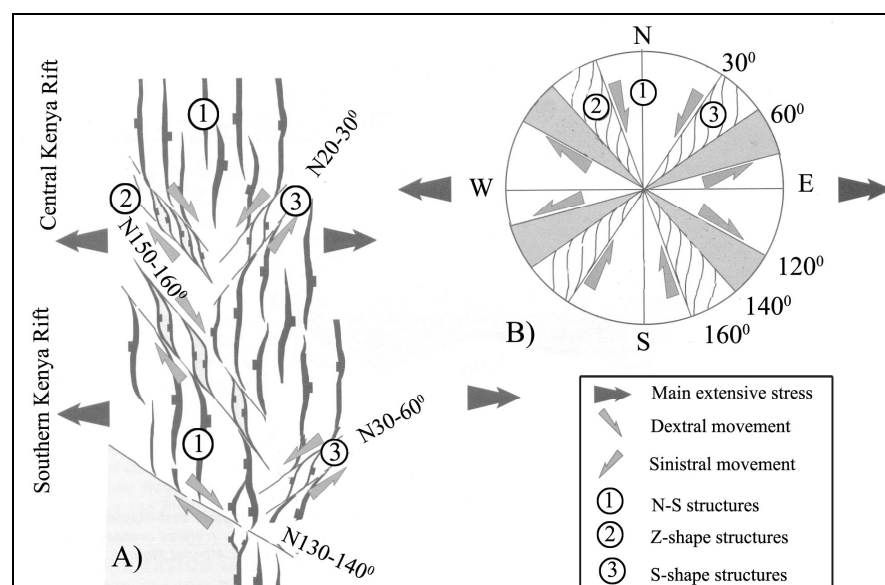


Figure 48 Conceptual tectonic development model of the Kenya Rift, modified after Le Turdu et al. (1999) in order to incorporate the NE-SW (N30-60) structures for the Lake Magadi area. B) Rose diagram showing orientation of the structures and the corresponding stress fields.

7. Conclusions and recommendations

7.1. Conclusions

The present understanding of the Kenya Rift, especially, in the southern Kenya Rift, indicates two plausible neotectonic extension directions E-W to ESE-WNW and NW-SE. The results of the present research, which aimed mainly at contributing to this present understanding of neo-tectonics in the Lake Magadi area, are presented below in relation to each of the specific research objectives.

In this research, conjunctive analysis of field and remotely sensed datasets were carried out in order to contribute to the understanding of the neo-tectonic extension of the Lake Magadi area.

7.1.1. Characterizing the surface and subsurface structures

7.1.1.1. Do the field and remotely sensed datasets support the E-W to ESE-WNW or NW-SE extensional neotectonics in the southern Kenya Rift?

Processing and structural analysis of ASTER datasets and SRTM DEM, field data and airborne magnetic data reveal four fault sets in the study area that trend: 1) N-S (N-S, NNE-SSW, NNW-SSE), 2) NW-SE, 3) ENE-WSW and 4) NE-SW.

- In the first set, the N-S faults are dominant and they deflect to NNE-SSW as well as to NNW-SSE forming Z and S patterns, respectively. The Z and S patterns observed in the remote sensing data are due to interference of the N-S faults with pre-existing NW-SE and NE-SW structures, respectively. Reactivation of the pre-existing structures has resulted in the formation of younger NW-SE (set two) and NE-SW (set four) faults that crosscut the N-S faults in the area.
- The Euler depth solution of the airborne magnetic data also gave similar result where the Euler points showed clustering along N-S, NW-SE, ENE-WSW and NE-SW.
- All fault sets have been verified in the field where normal N-S, dextral NW-SE, strike slip ENE-WSW and sinistral NE-SW fault sets have been observed. Crosscutting relationship observed in the field indicates that the N-S normal faults are oldest and the sinistral NE-SW faults are youngest.
- Even though the NE-SE fault set has been reported from different parts of the EARS, it was not reported from the Lake Magadi area so that it is a new finding of this research.

The existence of four set of faults (normal N-S, dextral NW-SE, strike slip ENE-WSW and sinistral NE-SW) having different styles and different relative ages signify occurrences of geodynamic changes in the neo-tectonics of the rift that created the four fault sets under an E-W extension which is explained by Anderson's fault model.

- At its early stage, the rift experienced normal faulting where σ_1 was acting vertically on the earth's surface and σ_3 acting horizontally along E-W which means an E-W direction of extension.
- Then as a result of geo-tectonic change in the rift, σ_1 changed orientation from acting vertically on top of the surface to act horizontally along N-S while σ_3 remained E-W; thus, the direction of extension remained E-W.
- The geo-tectonic change reactivated the pre-existing structures in the rift creating a dextral NW-SE, strike slip ENE-WSW and sinistral NE-SW faults under an E-W direction of extension.
- Preliminary paleostress reconstruction of the field data also shows that the neo-tectonic extension direction of the study area is E-W.

The finding of sinistral oblique slip NE-SW fault set supports the E-W extension in the area; it also explains the existence of NW-SE fault set. The youngest sinistral oblique slip NE-SW fault was formed by reactivation of pre-existing NE-SW structures under the E-W extension in order to counterbalance the dextral NW-SE faulting. Thus, the finding solves the puzzle that some researchers were associating the dextral NW-SE faulting with the NW-SE extension direction and the E-W to WNW extension advocates of Lake Magadi area have been assuming it as local feature regardless of its occurrence through out the whole Kenya Rift.

Significance of the four fault sets with respect to earthquake and hot-springs in the study area

Earthquake:

- Intersection of the N-S, NW-SE and NE-SW to ENE-WSW structures coincides with the margin of the cluster of the earthquake swarms in the northern part of the Lake Magadi.
- This implies that the clustering is associated with the intersection of the N-S structures and the reactivated NW-SE and NE-SW to ENE-WSW structures.
- Thus the reactivation of the pre-existing structures may have contributed to the clustering of the earthquake swarms in the northern part of the Lake Magadi area.
- This result supplements the existing understanding proposed by Seht et al.(2001) that the clustering and the shallow hypocenter depths beneath the earthquake cluster are associated with the presence of lower crustal magmatic intrusion where the crustal intrusion may have reactivated the pre-existing structures in the area.

Hot-springs:

- The presence of four sets of faults have created conducive environment for the movement of groundwater and its interaction with hot subsurface fluid resulting hot-springs in the area.
- The high fractal dimension value 2 from the fault throw and 3 from the fault length imply that the short faults (<1.6 km) and faults with small throws (<30m) have significant contribution in the area.
- Thus, the presence of short faults and faults with small throws coupled with the big faults having different orientation and subsurface continuation that go as deep as 2.4km serve as suitable conduits for the hot-springs in the Lake Magadi area

7.1.1.2. What is the implication of recent surface rupture on neotectonics of the southern Kenya Rift?

Processing and analysis of ground magnetic and resistivity datasets characterized the subsurface nature of the rupture and suggest the presence of other hidden rupture in the area.

- ❖ The 2D resistivity imaging of the ruptures showed that both ruptures penetrate to a depth of greater than 66m signifying that the ruptures were intense.
- ❖ Besides, field observation of the surface rupture shows that the rupture aligns along N-S to NNE-SSW signifying that the present extension direction is E-W.
- ❖ The clustering of earthquake swarms also support the E-W neotectonic extension in the area.

7.1.2. Lithologic investigation of the study area

Regional and local geology of the Lake Magadi area show that lithologies of the area are mainly basalts and trachytes with Precambrian basements occupying either flanks of the rift. However, existing geological maps are old which were prepared by reconnaissance survey so that they need updating.

- * The ASTER images were useful in discriminating the sediments of the area so that considering the field observation, lithologic boundary of the chert and clay unit as well as the tuff and clay unit were updated.
- * Besides, basalt which has high magnetic signal in the study area was differentiated from other volcanic units using aeromagnetic dataset.
- * The OITepsi basalt and benmoreites unit was classified in to two separate units where the high magnetic signal was assigned as basalt and the low magnetic signal as benmoreites.
- * The Pliocene Ologesaile volcanics (mainly basalt and trachyte) covering the shanamu and Ologesaile volcanoes were separated in to Ologesaile basalt (high magnetic) and the remaining units to Ologesaile volcanics (lower magnetic)
- * The Lenderut volcano showed high magnetic signal so that it was assigned to basalt.

Therefore geological map of the study area was updated based on field observations, ASTER images and aeromagnetic data. The area was exposed to basaltic and then trachytic volcanisms respectively with age so that the occurrence of basaltic outcrops on the surface is attributed to the normal faulting in the rift that brought the basalt to the surface.

7.2. Recommendations

Although the results of the present study are meaningful, very limited time was available for collecting structural data in the field. Therefore further field structural data is recommended in order to substantiate or revise the interpretations based on the reconstruction of the paleostress conditions of the study area. Moreover, field checking of places that were not visited during this research is required in order to verify and modify, if necessary, the updated geological map presented in this study.

Further geophysical investigation (for example, 3D resistivity imaging) of the ruptures may help in quantifying them which could contribute to the understanding of the extension in the area. Besides, searching other ruptures in different sites of the area could be worth to consider.

References

- Abrams, M., 2000. The Advanced Spaceborne Thermal Emission and Reflection Radiometer (ASTER): data products for the high spatial resolution imager on NASA's Terra platform. *International Journal of Remote Sensing*, 21(5): 847 - 859.
- Achauer, U. and Masson, F., 2002. Seismic tomography of continental rifts revisited: from relative to absolute heterogeneities. *Tectonophysics*, 358(1-4): 17-37.
- Anderson, E.M., 1951. *The Dynamics of Faulting*. Oliver & Boyd, London, 83 pp.
- Angelier, J., 1994. Fault slip analysis and paleostress reconstruction. In: P.L. Hancock (Editor), *Continental Deformation*. Pergamon, Oxford, pp. 101 -120.
- Arlegui, L.E. and Soriano, M.A., 1998. Characterizing lineaments from satellite images and field studies in the central Ebro basin (NE Spain). *International Journal of Remote Sensing*, 19(16): 3169 - 3185.
- Atmaoui, N. and Hollnack, D., 2003. Neotectonics and extension direction of the Southern Kenya Rift, Lake Magadi area. *Tectonophysics*, 364(1-2): 71-83.
- Baker, B.H., 1958. *Geology of the Magadi area*, Geological Survey of Kenya, Nairobi.
- Baker, B.H., 1986. Tectonics and volcanism of the southern Kenya rift valley and its influence on rift sedimentation. *Geological Society Special Publication 25(Sedimentation in the African rifts)*: 3-7.
- Baker, B.H. and Mitchell, J.G., 1976. Volcanic stratigraphy and geochronology of the Kedong - Olorgesailie area and the evolution of the South Kenya rift valley. In: *Journal of the Geological Society(London)*, 132(1976), pp. 467-484.
- Baker, B.H., Williams, L.A.J., Miller, J.A. and Fitch, F., J., 1971. Sequence and geochronology of the Kenya rift volcanics. *Tectonophysics*, 11 191-215
- Barritt, S.D., 1993. The African Magnetic Mapping project. *Special Issue ITC Journal(1993-2)*: 121-131.
- Bates, R.L. and Jackson, J.A. (Editors), 1987. *Glossary of geology* American Geological Institute, Alexandria.
- Bates, R.L. and Jackson, J.A., 1995. *Glossary of geology on CD - ROM*. American Geological Institute, Alexandria.
- Behrensmeyer, A.K., Deino, A.L., Hill, A., Kingston, J.D. and Saunders, J.J., 2002. Geology and geochronology of the middle Miocene Kipsaramon site complex, Muruyur Beds, Tugen Hills, Kenya. *Journal of Human Evolution*, 42(1-2): 11-38.
- Boccaletti, M. et al., 1998. Quaternary oblique extensional tectonics in the Ethiopian Rift (Horn of Africa). *Tectonophysics*, 287(1-4): 97-116.
- Bonham-Carter, G.F., 1994. *Geographic Information Systems for Geoscientists: Modelling with GIS*, 13. Pergamon, Ontario.
- Bosworth, W. and Strecker, M.R., 1997. Stress field changes in the Afro-Arabian rift system during the Miocene to recent period. *Tectonophysics*, 278: 47-62.

- Bosworth, W., Strecker, M.R. and Blinskiuk, P.M., 1992. Integration of East African paleostress and present day stress data: Implications for continental stress field dynamics. *J. of Geophysical research*, 97(B8): 11851-11865.
- Braile, L.W., Keller, G.R., Morgan, P. and Khan, M.A., 1995. The East African Rift System. In: K.H. Olsen (Editor), *Continental Rifts: evolution, structure, tectonics*. Developments in geotectonics 25. Elsevier, Amsterdam, pp. 213 - 231.
- Byrne, G.F., Jacob, A.W.B., Mechie, J. and Dindi, E., 1997. Seismic structure of the upper mantle beneath the southern Kenya Rift from wide-angle data. *Tectonophysics*, 278(1-4): 243-260.
- Chernet, T., Hart, W.K., Aronson, J.L. and Walter, R.C., 1998. New age constraints on the timing of volcanism and tectonism in the northern Main Ethiopian Rift-southern Afar transition zone (Ethiopia). *Journal of Volcanology and Geothermal Research*, 80(3-4): 267-280.
- Chorowicz, J., 2005. The East African rift system. *Journal of African Earth Sciences*, 43(1-3): 379-410.
- Chorowicz, J. and Sorlien, C., 1992. Oblique extensional tectonics in the Malawi Rift, Africa. *Geological Society of America Bulletin*, 104(8): 1015-1023.
- Condie, K.C., 1997. *Plate Tectonics and Crustal Evolution*, 4th edition. Butterworth-Heinemann, Oxford.
- Crossley, R. and Knight, R.M., 1981. Volcanism in the Western Part of the Rift Valley in Southern Kenya. *Bull. Volcanol*, 44(2).
- De Castro, D.L., de Oliveira, D.C. and Gomes Castelo Branco, R.M., 2007. On the tectonics of the Neocomian Rio do Peixe Rift Basin, NE Brazil: Lessons from gravity, magnetics, and radiometric data. *Journal of South American Earth Sciences*, 24(2-4): 184-202.
- Delvaux, D. and Sperner, B., 2003. New aspects of tectonic stress inversion with reference to the TENSOR program. *Geological Society, London, Special Publications*, 212(1): 75-100.
- Dewangan, P., Ramprasad, T., Ramana, M.V., Desa, M. and Shailaja, B., 2007. Automatic Interpretation of Magnetic Data Using Euler Deconvolution with Nonlinear Background. *Pure appl. geophys*, 164: 2359 - 2372.
- Dobrin, M.B. and Savit, C.H., 1988. *Introduction to geophysical prospecting*. McGraw-Hill, New York etc., 867 pp.
- Drury, S.A., 2001. *Image Interpretation in Geology*, 3. Nelson thrones UK.
- Ebinger, C.J. et al., 2000. Rift deflection, migration, and propagation: Linkage of the Ethiopian and Eastern rifts, Africa. *Geol Soc Am Bull*, 112(2): 163-176.
- Ebinger, C.J., Yemane, T., Woldegabriel, G., Aronson, J.L. and Walter, R.C., 1993. Late Eocene-Recent volcanism and faulting in the southern main Ethiopian rift. *Journal of the Geological Society*, 150(1): 99-108.
- Fairhead, J.D. and Girdler, R.W., 1972. The seismicity of the east african rift system. *Tectonophysics*, 15(1-2): 115-122.
- Furman, T., 2007. Geochemistry of East African Rift basalts: An overview. *Journal of African Earth Sciences*, 48(2-3): 147-160.
- Furman, T., Bryce, J.G., Karson, J. and Iotti, A., 2004. East African Rift System (EARS) Plume Structure: Insights from Quaternary Mafic Lavas of Turkana, Kenya. *J. Petrology*, 45(5): 1069-1088.
- Ganas, A., Pavlides, S. and Karastathis, V., 2005. DEM-based morphometry of range-front escarpments in Attica, central Greece, and its relation to fault slip rates. *Geomorphology*, 65(3-4): 301-319.

- Gani, N.D.S. and Abdelsalam, M.G., 2006. Remote sensing analysis of the Gorge of the Nile, Ethiopia with emphasis on Dejen-Gohatsion region. *Journal of African Earth Sciences*, 44(2): 135-150.
- George, R., Rogers, N. and Kelley, S., 1998. Earliest magmatism in Ethiopia; evidence for two mantle plumes in one flood basalt province. *Geology*, 26(10): 923-926.
- GETECH, 2007. Advanced processing and Interpretation of gravity and magnetic data. GETECH group plc.
- Gloaguen, R., Marpu, P.R. and Niemeyer, I., 2007. Automatic extraction of faults and fractal analysis from remote sensing data. *Nonlinear Processes in Geophysics*, 14(2): 131-138.
- Gomez, C., Delacourt, C., Allemand, P., Ledru, P. and Wackerle, R., 2005. Using ASTER remote sensing data set for geological mapping, in Namibia. *Physics and Chemistry of the Earth, Parts A/B/C*, 30(1-3): 97-108.
- Grauch, V.J.S., 2002. High-resolution aeromagnetic survey to image shallow faults, Dixie Valley Geothermal Field, Nevada. Open-File Report 02-384, US Geological Survey.
- Hackman, B.D., Charsley, T.J., Key, R.M. and Wilkinson, A.F., 1990. The development of the East African Rift system in north-central Kenya. *Tectonophysics*, 184(2): 189-211.
- Henry, W.J. et al., 1990. A seismic investigation of the Kenya Rift Valley. *Geophys. J. Inter*, 100: 107-130.
- Hollnack, D. and Stangl, R., 1998. The seismicity related to the southern part of the Kenya Rift. *Journal of African Earth Sciences*, 26(3): 477-495.
- Hsu, S.K., Sibue, J.C. and Shyu, C.T., 1996. High-resolution detection of geologic boundaries from potential-field anomalies: An enhanced analytic signal technique. *GEOPHYSICS*, 61(2).
- Jarrige, J.-J. et al., 1990. The multistage tectonic evolution of the Gulf of Suez and northern red sea continental rift from field observations. *Tectonics*, 9.
- Jestin, F., Huchon, P. and Gaulier, J.M., 1994. The Somalia plate and the East African Rift System: present-day kinematics. *Geophysical Journal International*, 116(3): 637-654.
- Jones, B.a.R., R., 1996. Morphology and growth of aragonite crystals in hot - spring travertines at Lake Bogoria, Kenya Rift Valley. *Sedimentology*, 43(2): 323-340.
- Jordan, G. and Schott, B., 2005. Application of wavelet analysis to the study of spatial pattern of morphotectonic lineaments in digital terrain models. A case study. *Remote Sensing of Environment*, 94(1): 31-38.
- Jutz, S.L. and Chorowicz, J., 1993. Geological mapping and detection of oblique extensional structures in the Kenyan Rift Valley with a SPOT/Landsat-TM datamerge. *International Journal of Remote Sensing*, 14(9): 1677 - 1688.
- Kalinowski, A. and Oliver, S., 2004. ASTER Mineral Index Processing Manua.
- Kampunzu, A.B., Bonhomme, M.G. and Kanika, M., 1998. Geochronology of volcanic rocks and evolution of the Cenozoic Western Branch of the East African Rift System. *Journal of African Earth Sciences*, 26(3): 441-461.
- Katz, M.B., 1987. East African rift and northeast lineaments: continental spreading--transform system? *Journal of African Earth Sciences*, 6(1): 103-107.
- Keller, G.R. et al., 1994. The East African rift system in the light of KRISP 90. *Tectonophysics*, 236(1-4): 465-483.

- Kington, J.D. and Goodliffe, A.M., 2008. Plate motions and continental extension at the rifting to spreading transition in Woodlark Basin, Papua New Guinea: Can oceanic plate kinematics be extended into continental rifts? *Tectonophysics*, 458(1-4): 82-95.
- Kis, K.I. and Pusztá, S., 2006. Application of magnetic field derivatives for locating Sarmatian graves. *Journal of Applied Geophysics*, 60(1): 13-26.
- Kurz, T., Gloaguen, R., Ebinger, C., Casey, M. and Abebe, B., 2007. Deformation distribution and type in the Main Ethiopian Rift (MER): A remote sensing study. *Journal of African Earth Sciences*, 48(2-3): 100-114.
- Le Gall, B. et al., 2008. Rift propagation at craton margin.: Distribution of faulting and volcanism in the North Tanzanian Divergence (East Africa) during Neogene times. *Tectonophysics*, 448(1-4): 1-19.
- Le Turdu, C. et al., 1999. Influence of Pre-existing Oblique discontinuities on the Geometry and Evolution of Extensional Fault Patterns: Evidence from the Kenya Rift Using SPOT Imagery. In: C.K. Morley (Editor), *Geoscience of Rift Systems-Evolution of East Africa*. AAPG Studies in Geology The American Association of Petroleum Geologists, Oklahoma, pp. 173-191.
- Levin, N., 1999. Fundamentals of Remote Sensing. In: N. Levin (Editor), 1st Hydrographic Data Management course, IMO. International Maritime Academy, Trieste, Italy.
- Lunina, O.V. and Gladkov, A.S., 2007. Late Cenozoic fault pattern and stress fields in the Barguzin rift (Baikal region). *Russian Geology and Geophysics*, 48(7): 598-609.
- Macdonald, R., 1994. Petrological evidence regarding the evolution of the Kenya Rift Valley. *Tectonophysics*, 236(1-4): 373-390.
- Macdonald, R., Rogers, N.W., Fitton, J.G., Black, S. and Smith, M., 2001. Plume-Lithosphere Interactions in the Generation of the Basalts of the Kenya Rift, East Africa. *J. Petrology*, 42(5): 877-900.
- Mariita, N.O. and Keller, G.R., 2007. An integrated geophysical study of the northern Kenya rift. *Journal of African Earth Sciences*, 48(2-3): 80-94.
- Marrett, R. and Allmendinger, R.W., 1992. Amount of extension on "small" faults: An example from the Viking graben. *Geology*, 20(1): 47-50.
- Mechie, J. et al., 1994. Crustal structure beneath the Kenya Rift from axial profile data. *Tectonophysics*, 236(1-4): 179-200.
- Mechie, J., Keller, G.R., Prodehl, C., Khan, M.A. and Gaciri, S.J., 1997. A model for the structure, composition and evolution of the Kenya rift. *Tectonophysics*, 278(1-4): 95-119.
- Morgan, P. and Baker, B.H. (Editors), 1983. Processes of continental Rifting. *Developments in Geotectonics* 19, Reprinted from *Tectonophysics* volume 94. Elsevier, Amsterdam, 680 pp.
- Morley, C.K. et al., 1992. Tectonic evolution of the northern Kenyan Rift. *Journal of the Geological Society*, 149(3): 333-348.
- Mushayandebvu, M.F., Drielz, P.V., Reid, A.B. and Fairhead, J.D., 2001. Magnetic source parameters of two-dimensional structures using extended Euler deconvolution. *Geophysics*, 66(3): 814-823.
- Nabighian, M., 1984. Toward a three-dimensional automatic interpretation of potential field data via generalized Hilbert transforms: Fundamental relations *Geophysics*, 49: 780-786.
- Needham, T., Yielding, G. and Fox, R., 1996. Fault population description and prediction using examples from the offshore U.K. *Journal of Structural Geology*, 18(2-3): 155-167.

- Ngecu, W.M. and Njue, J.N., 1999. Lithostratigraphy and distribution of Pleistocene sediments of the Munyu wa Gicheru Formation in South Kenya Rift Valley. *Journal of African Earth Sciences*, 29(2): 411-421.
- Nonnotte, P. et al., 2008. New K-Ar age determinations of Kilimanjaro volcano in the North Tanzanian diverging rift, East Africa. *Journal of Volcanology and Geothermal Research*, 173(1-2): 99-112.
- Olsen, K.H. and Morgan, P., 1995. Progress in understanding continental rifts. In: K.H. Olsen (Editor), *Continental Rifts : evolution, structure, tectonics*. Developments in geotectonics 25 Elsevier, Amsterdam pp. 1 - 26.
- Owusu, E.A., Woldai, T., Carranza, E.J.M. and Hale, M., 2006. Analysis and integration of Landsat ETM and SRTM data for geological mapping of the Kibi area in Ghana : abstract. In: Abstracts of oral and poster presentations from the SEG 2006 conference : wealth creation in the minerals industry, May 14-16, 2006, Keystone, Colorado, USA. pp. 330-338.
- Parsons, S., Nadeau, L., Keating, P. and Chung, C.-J., 2006. Optimizing the use of aeromagnetic data for predictive geological interpretation: an example from the Grenville Province, Quebec. *Computers & Geosciences* 32: 565-576.
- Pavlidis, S.B., 1989. Looking for a definition of Neotectonics. *Terra Nova*, 1(3): 233-235.
- Qari, M.H.T., Madani, A.A., Matsah, M.I.M. and Hamimi, Z., 2008. Utilization of aster and landsat data in geologic mapping of basement rocks of arafat area, Saudi arabia. *The Arabian Journal for Science and Engineering* 33(1C): 99-116.
- Reeves, C.V., 1989. Aeromagnetic interpretation and rock magnetism. 27(7).
- Reid, A.B., 1995. Euler deconvolution: Past, present and future, a review, 65th Ann. Internat. Mtg., Soc. Expl. Geophys Expanded Abstracts, pp. 272-273.
- Reid, A.B., Allsop, J.M., Granser, H., Millett, A.J. and Somerton, I.W., 1990. Magnetic interpretation in three dimensions using Euler deconvolution. *Geophysics*, 55: 80-91.
- Roest, W.R., Verhoef, J. and Pilkington, M., 1992. Magnetic interpretation using the 3-D analytic signal. *Geophysics*, 57(1).
- Rogers, J.J.W., 1993. *A History of the Earth*. Cambridge University Press.
- Rogers, N. et al., 2000. Two mantle plumes beneath the East African rift system: Sr, Nd and Pb isotope evidence from Kenya Rift basalts. *Earth and Planetary Science Letters*, 176(3-4): 387-400.
- Rosendahl, B.R., Kilembe, E. and Kaczmarick, K., 1992. Comparison of the Tanganyika, Malawi, Rukwa and Turkana Rift zones from analyses of seismic reflection data. *Tectonophysics*, 213(1-2): 235-256.
- Roux, A.T., 1980. *Geophysical field manual for technicians. The magnetic method, No. 1*. South African geophysical association.
- Rowan, L.C. and Mars, J.C., 2003. Lithologic mapping in the Mountain Pass, California area using Advanced Spaceborne Thermal Emission and Reflection Radiometer (ASTER) data. *Remote Sensing of Environment*, 84(3): 350-366.
- Rowan, L.C., Mars, J.C. and Simpson, C.J., 2005. Lithologic mapping of the Mordor, NT, Australia ultramafic complex by using the Advanced Spaceborne Thermal Emission and Reflection Radiometer (ASTER). *Remote Sensing of Environment*, 99(1-2): 105-126.
- Seht, M.I.-V., Blumenstein, S., Wagner, R., Hollnack, D. and Wohlenberg, J., 2001. Seismicity, seismotectonics and crustal structure of the southern Kenya Rift - new data from the Lake Magadi area. *Geophys. J. Inter*, 146: 439-453.

- Sengor, A.C. and Burke, K., 1978. Relative timing of rifting and volcanism on earth and its tectonic implications. *Geophys Res. Lett.*, 5: 419-421.
- Simiyu, S.M. and Keller, G.R., 1998. Upper crustal structure in the vicinity of Lake Magadi in the Kenya Rift Valley region. *Journal of African Earth Sciences*, 27(3-4): 359-371.
- Simiyu, S.M. and Randy Keller, G., 1998. Upper crustal structure in the vicinity of Lake Magadi in the Kenya Rift Valley region. *Journal of African Earth Sciences*, 27(3-4): 359-371.
- Skobelev, S.F. et al., 2004. Active faults in Africa: a review. *Tectonophysics*, 380(3-4): 131-137.
- Suzen, M.L. and Toprak, V., 1998. Filtering of satellite images in geological lineament analyses: an application to a fault zone in Central Turkey. *International Journal of Remote Sensing*, 19(6): 1101 - 1114.
- Thompson, D.T., 1982. EULDPH A new technique for making computer assisted depth estimates from magnetic data. *Geophysics*, 47: 31-37.
- Thurmond, A.K., Abdelsalam, M.G. and Thurmond, J.B., 2006. Optical-radar-DEM remote sensing data integration for geological mapping in the Afar Depression, Ethiopia. *Journal of African Earth Sciences*, 44(2): 119-134.
- Thurston, J.B. and Smith, R.S., 1997. Automatic conversion of magnetic data to depth, dip, and susceptibility contrast using the SPI (TM) method. *GEOPHYSICS*, 62(3): 807- 813.
- Ukstins, I.A. et al., 2002. Matching conjugate volcanic rifted margins: $^{40}\text{Ar}/^{39}\text{Ar}$ chrono-stratigraphy of pre- and syn-rift bimodal flood volcanism in Ethiopia and Yemen. *Earth and Planetary Science Letters*, 198(3-4): 289-306.
- Van Avendonk, H.J.A., Lavier, L.L., Shillington, D.J. and Manatschal, G., In Press. Extension of continental crust at the margin of the eastern Grand Banks, Newfoundland. *Tectonophysics*, In Press, Corrected Proof.
- Van Roij, A., Carranza, E.J.M., Hale, M. and Owusu, E.A., 2006. Geological remote sensing and gold prospectivity mapping in Kibi area, Ghana. In: AARSE 2006 : Proceeding of the 6th AARSE international conference on earth observation and geoinformation sciences in support of Africa's development, 30 October - 2 November 2006, Cairo, Egypt. Cairo : The National Authority for Remote Sensing and Space Science (NARSS), 2006. ISBN 1-920-01710-0. 8 p.
- Vétel, W., Le Gall, B. and Tiercelin, J.-J., 2003. Neotectonics along the Turkana rift (north Kenya) from river network analysis, remote sensing and reflection seismic data *European Geophysical Society*, 5(Geophysical Research Abstracts).
- Vétel, W., Le Gall, B. and Walsh, J.J., 2005. Geometry and growth of an inner rift fault pattern: the Kino Sogo Fault Belt, Turkana Rift (North Kenya). *Journal of Structural Geology*, 27(12): 2204-2222.
- Walsh, J.J. et al., 2003. Strain localisation and population changes during fault system growth within the Inner Moray Firth, Northern North Sea. *Journal of Structural Geology*, 25(2): 307-315.
- Walsh, J.J. and Watterson, J., 1992. Populations of faults and fault displacements and their effects on estimates of fault-related regional extension. *Journal of Structural Geology*, 14(6): 701-712.
- Wang, S., Zhang, J., Wang, Y., Zhang, J. and Li, B., 2004. Simple operator based edge detection of binary image. In: J.P. Li (Editor), *The Proceedings of the International Computer Congress on Wavelet analysis and its applications and active media technology*.
- Watchorn, F., Nichols, G.J. and Bosence, D.W.J., 1998. Rift related sedimentation and stratigraphy, southern Yemen (Gulf of Aden). In: B.H. Purser and D.W.J. Bosence (Editors), *Sedimentation and Tectonics in Rift Basins: Red Sea-Gulf of Aden*. Springer.

- Wolfenden, E., Ebinger, C., Yirgu, G., Deino, A. and Ayalew, D., 2004. Evolution of the northern Main Ethiopian rift: birth of a triple junction. *Earth and Planetary Science Letters*, 224(1-2): 213-228.
- Won-In, K. and Charusiri, P., 2003. Enhancement of thematic mapper satellite images for geological mapping of the Cho Dien area, Northern Vietnam. *International Journal of Applied Earth Observation and Geoinformation*, 4(3): 183-193.
- Yielding, G., Needham, T. and Jones, H., 1996. Sampling of fault populations using sub-surface data: a review. *Journal of Structural Geology*, 18(2-3): 135-146.
- Yirgu, G., Ebinger, C.J. and Maguire, P.K.H., 2006. The Afar volcanic province within the East African Rift System: introduction. *Geological Society, London, Special Publications*, 259(1): 1-6.

Appendix

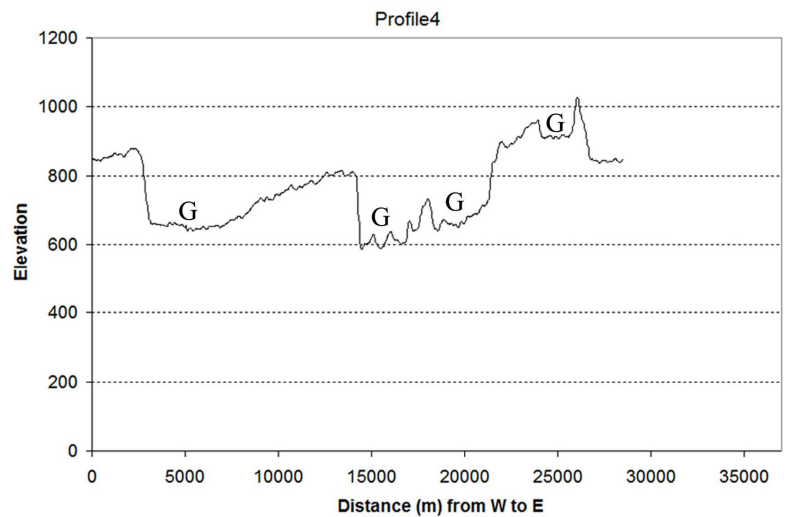
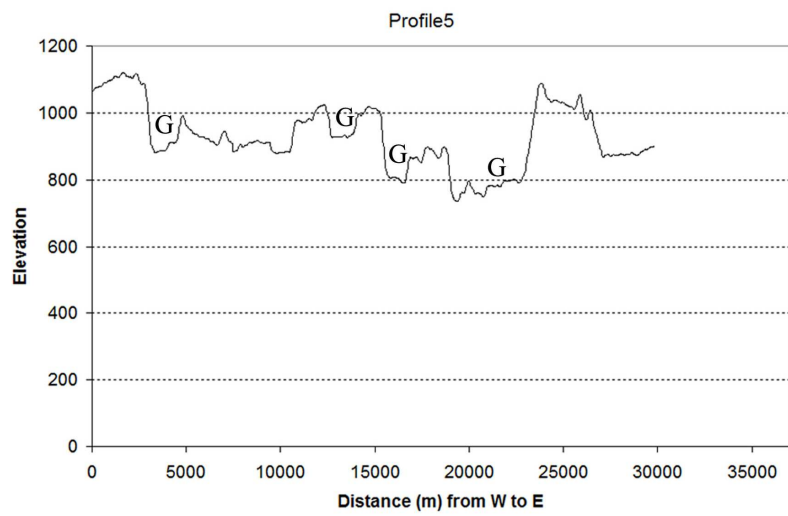
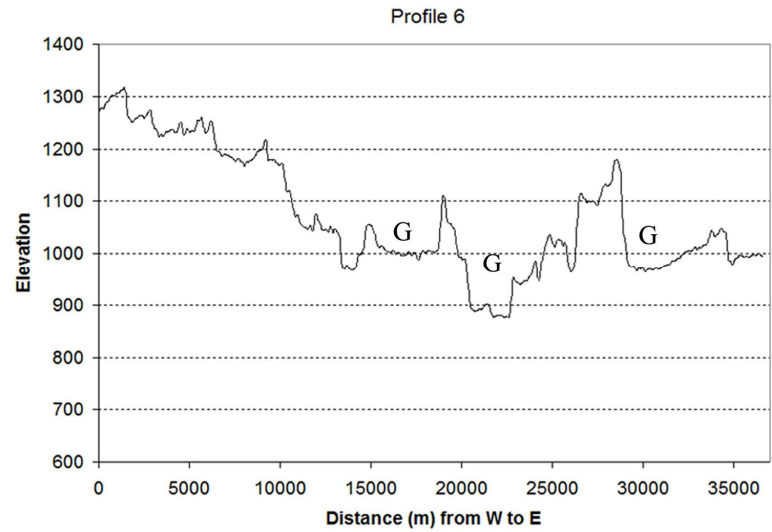


Figure 49 Topographic section (distance versus elevation) along profiles 4-6 derived from the ASTER DEM. The section runs from west on the left to east on the right, G represents graben.

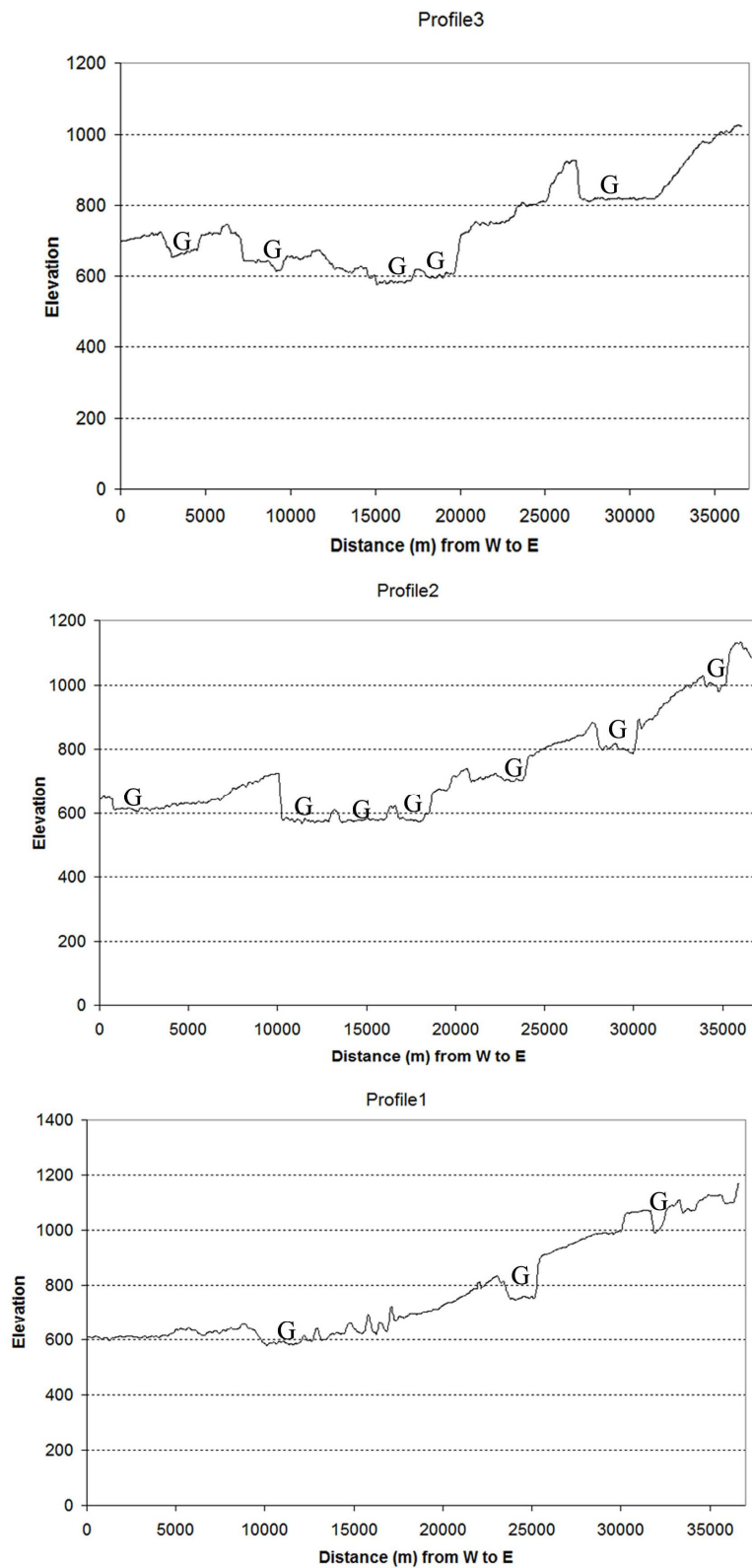


Figure 50 Topographic section (distance versus elevation) along profiles 1-3 derived from the ASTER DEM. The section runs from west on the left to east on the right, G represents graben.

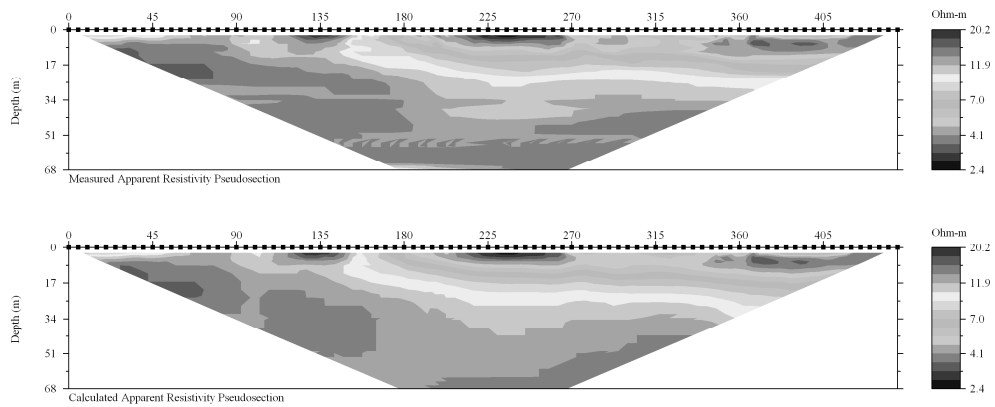


Figure 51 measured resistivity and calculated apparent resistivity pseudo sections along profile one of the rupture area.

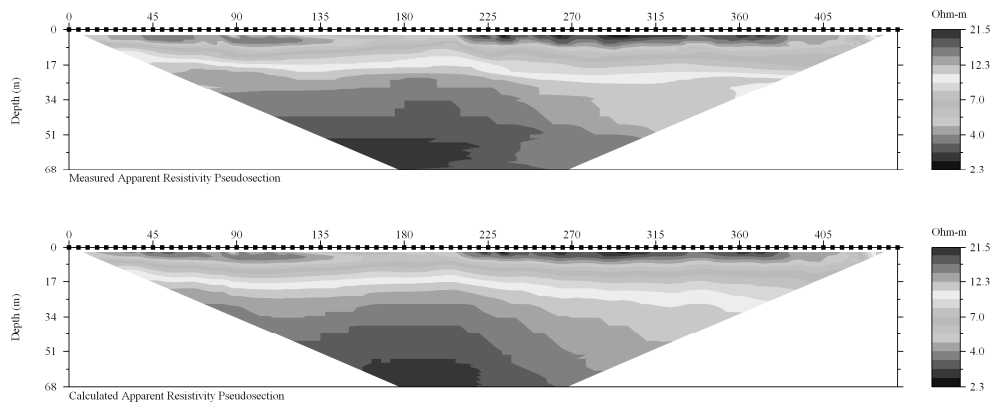


Figure 52 Measured resistivity and calculated apparent resistivity pseudo sections of profile two of the rupture area.